Technical Letter Report
TLR-RES/DE/REB-2025-12

U.S.NRC
United States Nuclear Regulatory Commission
*Protecting People and the Environment*

# REVIEW OF COMPOSITES FOR HIGH-TEMPERATURE NUCLEAR APPLICATIONS

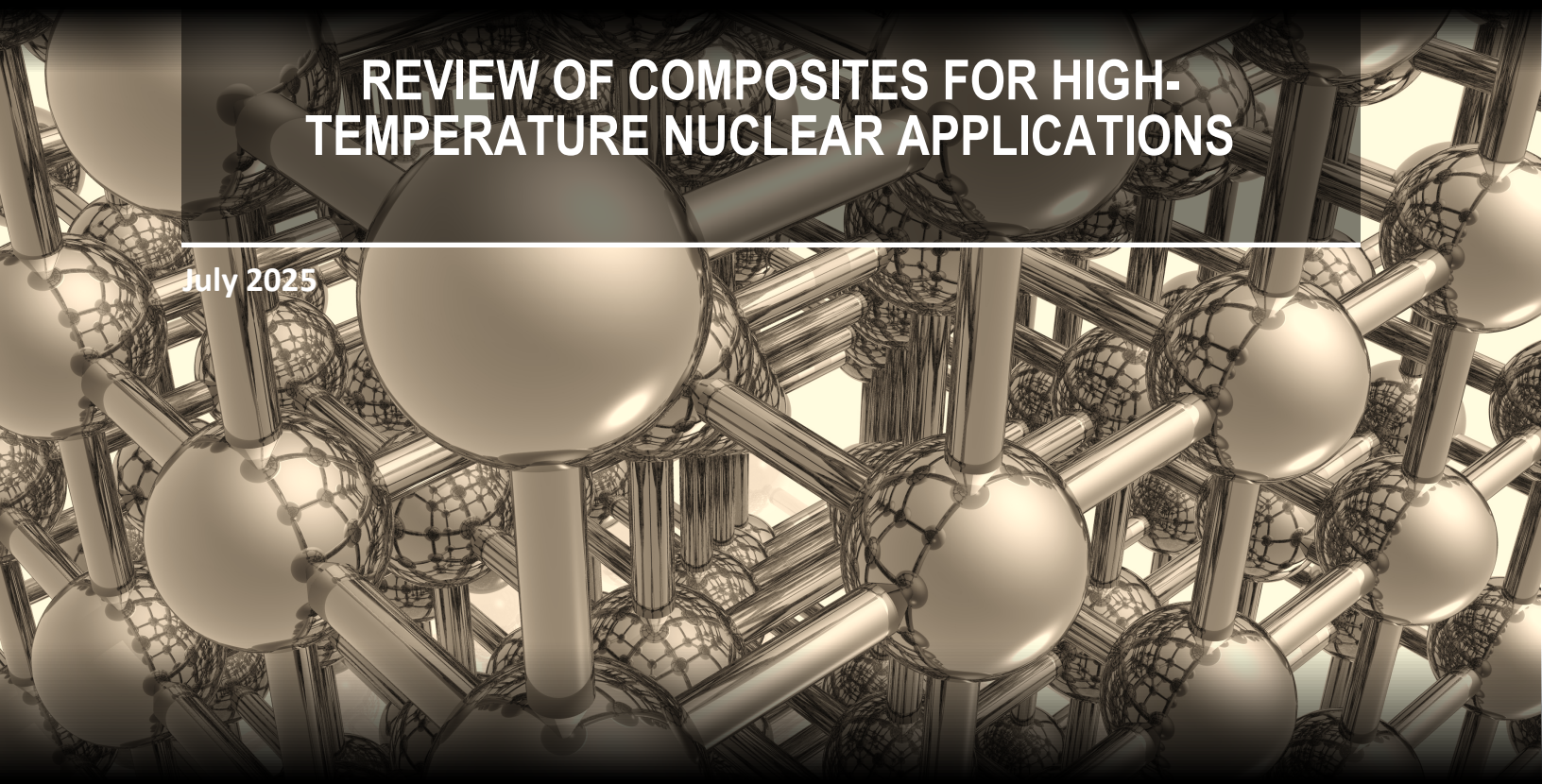

July 2025

***Farjana Sultana, Bipul Barua, Pawan Chaugule, Mark Messner***
Argonne National Laboratory

***Joseph Bass***
U.S. Nuclear Regulatory Commission

**Division of Engineering**
**Office of Nuclear Regulatory Research**
**U.S. Nuclear Regulatory Commission**
**Washington, DC 20555–0001**

**This report does not contain or imply legally binding requirements. Nor does this report establish or modify any regulatory guidance or positions of the U.S. Nuclear Regulatory Commission and is not binding on the Commission.**

*Page intentionally left blank*

Argonne NATIONAL LABORATORY

# Review of Composites for High-Temperature Nuclear Applications

Applied Materials Division

**About Argonne National Laboratory**

Argonne is a U.S. Department of Energy laboratory managed by UChicago Argonne, LLC under contract DE-AC02-06CH11357. The Laboratory's main facility is outside Chicago, at 9700 South Cass Avenue, Argonne, Illinois 60439. For information about Argonne and its pioneering science and technology programs, see www.anl.gov.

# Review of Composites for High-Temperature Nuclear Applications

Prepared by

Farjana Sultana
Bipul Barua
Pawan Chaugule
Mark C. Messner

Argonne National Laboratory

July 2025

*Page intentionally left blank*

## EXECUTIVE SUMMARY

This report provides a comprehensive evaluation of carbon–carbon (C/C) and silicon carbide–silicon carbide (SiC/SiC) ceramic matrix composites (CMCs), focusing on their potential use in elevated-temperature nuclear applications. It surveys key fabrication processes, outlines material property changes under irradiation, analyzes degradation mechanisms such as oxidation and corrosion, and discusses various structural failure modes. By compiling data from published studies, the report offers insights on how these CMCs might perform in advanced reactor environments.

The fabrication section details how C/C and SiC/SiC composites are produced using approaches such as chemical vapor infiltration, polymer impregnation and pyrolysis, nanopowder infiltration and transient eutectic phase processing, and melt infiltration. Each method balances critical factors such as densification time, cost, process temperature, and porosity. Impurity control – the ability to minimize neutron-absorbing or oxidation-promoting elements – emerges as a significant consideration, particularly for nuclear components operating under high flux conditions.

Both C/C and SiC/SiC CMCs fail progressively rather than catastrophically. The progressive failure process involves matrix cracking and interfacial debonding, which lead to fiber pull-out and eventual failure. Compared to monolithic ceramics, this complex failure process increases toughness and decreases strength. As the failure process progresses, the load-bearing capacity decreases. Predictive modeling frameworks, based on approaches ranging from micromechanical to continuum damage models, aid in the sound assessment of component performance and the prediction of the failure process.

In surveying material properties, the report summarizes published data on unirradiated and neutron-irradiated mechanical behaviors. C/C composites commonly exhibit initial improvements in mechanical properties at lower neutron doses, followed by anisotropic distortions and dimensional instability at higher doses. In comparison, near-stoichiometric SiC/SiC composites typically maintain strength under moderate fluences. Thermal conductivity drops significantly with dose for both C/C and SiC/SiC CMCs. Fiber type, matrix composition, fiber-matrix interface design, and preform architecture are important characteristics that affect CMC behavior.

Oxidation and corrosion analyses reveal that C/C composites are susceptible to degradation, especially in high-temperature air or steam ingress scenarios. However, this can be mitigated by protective coatings and highly crystalline carbon. In comparison, SiC/SiC composites form protective silica layers under passive oxidation conditions. Nevertheless, in SiC/SiC, oxidation and molten salt corrosion of fiber interphases can lead to embrittlement, which can be managed through careful tailoring of crystallinity, fiber coatings, and environmental barriers.

Finally, the report addresses nondestructive testing methods – thermal imaging, ultrasonic testing, X-ray computed tomography, and acoustic emissions – that can identify defects, monitor in-service damage, and validate design margins during operation. By integrating improved manufacturing

controls, thorough impurity screening, tailored coatings, and advanced inspection methods, C/C and SiC/SiC composites can be used more safely and efficiently for high-temperature nuclear reactor components.

## TABLE OF CONTENTS

*Page intentionally left blank*

## LIST OF FIGURES

# LIST OF TABLES

*Page intentionally left blank*

# 1 Introduction

Next-generation nuclear systems, including very high-temperature reactors (VHTRs), molten salt reactors (MSRs), and gas-cooled fast reactors (GFRs), require structural materials capable of withstanding extreme service conditions, including high temperatures, intense neutron irradiation, corrosive coolants, and significant thermal and mechanical loads. The nuclear materials research community has turned significant attention toward ceramic matrix composites (CMCs) due to their promising combination of high strength-to-weight ratios and excellent high-temperature stability. Furthermore, some varieties have shown favorable response to irradiation damage and have demonstrated an intrinsic resistance to thermal shock and/or oxidation. These properties make CMCs strong candidates for critical core components of next-generation nuclear reactors.

Among the various CMC classes, carbon–carbon (C/C) and silicon carbide–silicon carbide (SiC/SiC) composites currently stand at the forefront of research and development [1-4]. Both materials exhibit exceptional high-temperature stability and robust mechanical properties, positioning them well for demanding core applications. However, each also presents challenges, such as dimensional changes under irradiation, oxidation susceptibility, and the presence of processing-related impurities that may impact long-term performance. As a result, current research efforts are focused on refining fiber architectures, matrix infiltration techniques, and interphase coatings to optimize material behavior. Within this context, a deeper understanding of how microstructure, manufacturing methods, and service conditions collectively govern the properties of C/C and SiC/SiC is essential to enable their successful deployment in advanced reactor systems.

In parallel with these technical developments, there is a growing need to align emerging performance data on CMCs with established industry codes and standards – specifically, the American Society of Mechanical Engineers (ASME) Boiler and Pressure Vessel Code (BPVC) Section III, Division 5, which outlines design and construction rules for high-temperature nuclear components. Current composite rules and the broader discourse on structural design often need additional data on fabrication procedures, impurity limits, mechanical and thermal properties, and in-service inspection protocols to ensure the reliability and safety of these materials under nuclear operating conditions. Efforts are underway to refine the relevant standards, as exemplified by ASTM C1783 and C1793 guidelines for nuclear-grade carbon and SiC-based composites, respectively. A more comprehensive understanding of the material processing – structure–performance relationships is therefore critical to ensure that new composites can be effectively integrated into advanced reactor designs.

This report gathers and synthesizes the present state of knowledge surrounding C/C and SiC/SiC composites. Following this introductory chapter, the report begins with an overview of fabrication processes, highlighting key manufacturing parameters, common routes to fiber and matrix production, and associated limitations or impurity concerns in Chapter 2. Chapter 3 discusses current structural and failure analysis methods – covering both engineering-level theories and continuum damage approaches – alongside creep, fatigue, and irradiation- and oxidation-induced

defect modeling. Next, Chapter 4 explores the evolution of material properties under irradiation, illustrating how neutron damage impacts mechanical performance, thermal conductivity, and dimensional stability. Chapter 5 examines oxidation and corrosion phenomena, considering how environments ranging from air ingress to molten salts can compromise or, in select cases, even enhance material properties. Chapter 6 addresses nondestructive inspection techniques suitable for pre-service qualification and in-service monitoring, including thermal imaging, ultrasound, X-ray computed tomography, and acoustic emission methods. Finally, the report concludes by summarizing the key takeaways from the literature survey.

# 2 Fabrication Processes and Manufacturing Limitations

This chapter presents a literature review of various fabrication methods for C/C and SiC/SiC CMCs. It also separately reviews the methods for producing the fiber and matrix constituents of the composite. Additionally, the chapter discusses the manufacturing limitations and impurities.

## 2.1 Processes for Fabricating C/C CMCs

The fabrication of high-performance C/C CMCs [5-8] involves a process that integrates carbon fibers (C-fibers) and a carbon matrix (C-matrix). These composites are tailored to meet specific mechanical requirements through a careful selection of fiber types and reinforcement architectures. The fabrication process has three main steps: C-fiber preforms molding, densification, and graphitization [9]. It begins with molding a C-fiber preform, which serves as the structural framework and significantly influences the composite's properties. Following preform molding, the densification step involves filling the porous C-matrix with gaseous or liquid precursors. This process can include multiple cycles of impregnation and pyrolysis to enhance density. The final step is graphitization, where the composite undergoes high-temperature treatment to enhance the microstructure, improve mechanical properties, and improve thermal stability. The careful selection of fiber types, reinforcement architectures, matrix fabrication methods, and heat treatments are critical to achieve a high-quality C/C composite that meets the specific requirements of its intended application.

### *2.1.1 Fibers*

C-fibers are the primary load-bearing components in C/C composites; hence, they greatly impact the mechanical and thermal properties of the final composites [10-13]. The producer's selection of C-fibers is made based on the mechanical requirements of the final composite. Commercially available C-fiber types include high tensile, high modulus, and intermediate modulus fibers [14]. C-fibers' performance and application range depend largely on their precursor polymer chemistry and manufacturing process conditions, which ideally should ensure high desired product yields, ease of conversion, and cost-effective processing.

The C-fibers considered for use in nuclear C/C composite applications are derived from three major precursors: (i) acrylic precursors such as polyacrylonitrile (PAN), (ii) pitch-base precursors derived from petroleum or coal tar, and (iii) cellulosic precursors such as rayon [1]. Among these, PAN-derived C-fibers dominate production by making up more than 90% of the C-fibers manufactured in recent years due to their high desired product yields, mechanical strength, and thermal stability [15]. The manufacturing process for PAN-based C-fibers involves doping to control structure, spinning to enhance mechanical strength and crystallinity, and is followed by carbonization and graphitization to convert them into high-performance fibers [15]. Properties vary with manufacture, but typically PAN-based C-fibers can offer higher strength than pitch-based C-fibers, while the opposite is true for thermal conductivity. Both PAN and pitch derived C-fibers offer higher thermal conductivity than traditional refractory metals [16]. Additionally,

these fibers can be graphitized to enhance the long-range ordering of their graphite microstructure and further improve the thermal conductivity. Finally, the cellulose-based C-fibers exhibit lower thermal conductivity and tensile strength, and are suitable for thermal insulation and ablation applications [1].

C-fibers are woven into preforms to meet application-specific demands by forming the primary reinforcing network of the C/C composite. These fibers are assembled into preform architectures through techniques like weaving, braiding, or needling, ranging from unidirectional (1D) to multidimensional (2D, 2.5D, 3D, etc.) structures [16]. The structural geometry of fiber arrangement critically influences composite properties. Unidirectional (1D) preforms provide high strength and modulus along a single axis but exhibit poor performance in other directions [9]. Two-dimensional (2D) preforms, such as carbon cloth laminated structures and non-woven felts, enhance X-Y plane properties but have limited Z-direction strength due to the lack of fiber continuity [9]. Advanced 3D braiding techniques enable multiaxial reinforcement improving isotropy and delivering superior mechanical performance in multiple directions [17, 18]. For nuclear applications, preform architectures that align with specific loading conditions can optimize mechanical and thermal performance. The wide range of processing and architectural variations in C-fibers necessitates extensive testing and qualification for nuclear and other high-performance applications.

### *2.1.2 Matrix and Composites*

A C-matrix is created by precursor infiltration into the C-fiber preform architecture to form the C/C CMC. The matrix precursor infiltration typically involves the use of one or more volatile hydrocarbons. The general methods used are: (i) gas-phase densification, specifically chemical vapor infiltration (CVI), and (ii) liquid-phase densification. Both techniques enable the effective impregnation of complex preform geometries.

i. CVI: CVI involves growing a dense C-matrix throughout a preform architecture. The infiltration process is performed by introducing volatile hydrocarbon precursors, such as alkenes, unsaturated hydrocarbons, and aromatic hydrocarbons into a chamber containing the fiber preform [6]. Heating the system to 800 - 1200 °C decomposes the precursors, depositing carbon onto the fiber surfaces and expelling product gases that are produced from the precursors [6]. CVI can produce high-purity graphitizable carbon matrices. The degree of graphitization is a measure of the long-range ordering of the graphite matrix and affects many material properties, including the thermal conductivity and thermomechanical strength of the composite (which all increase with increased graphitization) [15, 16]. Temperature and pressure gradients within the furnace during processing can be used to reduce processing times. Adjusting precursor gas composition, temperature, and pressure affects the density, morphology, and anisotropy of the C-matrix. Higher tempera-

tures and pressures yield denser structures with greater anisotropy due to enhanced graphitization [19]. These combined factors allow for variation in the CVI method to tailor final component properties to the application, as well as producing an overall quick process, even with repeated infiltration steps [20].

ii. Liquid-phase densification involves impregnating C-fiber preforms with a liquid carbon precursor, such as pitch or thermosetting resin, under vacuum [21]. The preforms are carbonized and pyrolyzed at temperatures above 800°C to convert the precursor into a C-matrix [21]. During pyrolysis, hydrocarbon gases such as methane and propane are released, forming multiple layers of carbon within the preform [21]. This process is repeated several times to fill the pores and achieve the desired density and physical properties. The number of densification cycles depends on the carbonization efficiency of the matrix material and the specifics of the impregnation method used [21]. Two primary approaches to liquid-phase densification are classified based on the type of matrix material used: thermosetting resin impregnation (using epoxy, phenol, or furan resin) and pitch impregnation (using petroleum or coal tar) [1]. Pitch-based impregnation offers advantages over resins due to its liquid-phase carbonization, which enhances molecular orientation, thermal conductivity, and shrinkage control [21]. However, during pitch-based impregnation, the carbonization at atmospheric pressure often leaves voids due to volume reduction during volatilization [21]. A high-pressure step (>1000 bar) mitigates this shortcoming by increasing carbon yield and reducing the number of impregnation cycles required to achieve a particular loading, albeit at higher costs [18]. This step can also be used, in complement, after the other densification processes (resin impregnation or CVI). The final step in the C/C composite production is the high-temperature graphitization step, which is performed at a temperature ranging from 2200 to 2800 °C to achieve a highly crystalline structure close to the density of graphite [21].

The limitations of the above methods include:

i. CVI typically results in a residual porosity ranging from 10% to 15% by volume, depending on variables such as process time, temperature, and the number of impregnation cycles performed [19]. Additionally, CVI processes often result in uneven densification, particularly in thicker components [13]. To address this issue, multiple cycles are usually required, with intermediate machining steps to remove any carbon layer blocking the surface pores between CVI cycles [19].

ii. Liquid infiltration faces challenges in microstructure control and requires significant time during the carbonization process [21]. The thermal decomposition of hydrocarbons releases gases that can damage the C-matrix if released too quickly [16].

## 2.2 Processes for Fabricating SiC/SiC CMCs

In SiC/SiC CMCs, the interphase (interfacial substance between the fibers and the matrix) is a crucial constituent that is equally as important as the fibers and the matrix themselves. The fibers primarily carry the load, while the matrix and interphase are responsible for transferring the load to the fibers.

### *2.2.1 Fibers*

SiC fibers were first developed using the polymer precursor method by Yajima and Hayashi [22]. These fibers are used widely due to their mechanical properties, affordability, and weavability. Commercially available fibers like Nicalon™ and Tyranno Fiber™ are produced by melt-spinning of polycarbosilane (PCS) or polytitanocarbosilane (PTCS). These spun fibers are stabilized through heating in oxygen and then ceramized in an inert atmosphere at around 1300°C [23]. Generation I SiC fibers have high oxygen and carbon content. They contain poorly crystallized SiC embedded in a glassy Si-$O_x$-$C_y$ matrix. For example, ceramic-grade Nicalon contains 65% SiC with 23% silica and 11% free carbon phases [23]. As a result, Generation I SiC-based fibers have poor radiation tolerance due to the significant amounts of silica and carbon present. Generation II fibers, like Hi-Nicalon™, show minor improvement on radiation stability over that of the previous generation fibers by reducing the oxygen content. However, their microstructure remains unstable under radiation due to the presence of a large amount of excess carbon [24]. Generation III SiC fibers, such as Hi-Nicalon Type S [23, 25], Tyranno SA3 [26], and Sylramic™ [27], exhibit near-stoichiometric composition, enhanced crystallinity, and very low levels of excess carbon and oxygen contents. These improvements make them ideal for nuclear applications due to their dimensional stability under irradiation compared to Generation I and II fibers. Generation III fibers are made of beta-phase SiC grains that range from tens to hundreds of nanometers in size. These fibers demonstrate improved properties like higher elastic modulus, thermal conductivity, smaller elongation, and a coefficient of thermal expansion (CTE) that closely matches that of pure beta-SiC.

SiC CMCs are strongly influenced by fiber architecture, including volume fraction and orientation, which governs the composite's mechanical and thermal properties. Common architectures include 2D woven fabrics, 2.5D layups with cross weaving through the woven fabrics, and 3D orthogonal weaves. In 2D woven structures, 0°/90° stacking of orthogonally woven fabrics results in orthotropic properties, whereas 0°/±30° stacking allows more isotropic in-plane properties at the expense of somewhat reduced on-axis strength [24]. Among non-2D architectures, the 1D architectures maximize strength in one direction, while 3D weaves with adjustable fiber ratios (x:y:z) allow for customization of anisotropic properties. Braided preforms, available in both 2D and 3D, are valued for their conformability, damage resistance, and ability to adapt to complex shapes [16]. 2D braided preforms are composed of intertwined fiber structures capable of 0° and ±θ layups [28]. On the other hand, 3D braided preforms are created by intertwining or interlacing yarns orthogonally, providing through-thickness reinforcement and making them suitable for a

wide range of complex shapes [28]. The different fiber architectures also influence the fiber volume fraction, pore size, and distribution, all of which are critical to the thermomechanical performance of the composite [16].

### *2.2.2 Interphase*

The fiber-matrix interface in SiC/SiC composites is crucial in facilitating effective load transfer, as well as for maintaining adequate debonding strength and sliding resistance between the fibers and the matrix. The interphase significantly enhances the mechanical performance and damage tolerance of the composites by enabling crack deflection and fiber pull-out during fracture, which improves toughness through frictional energy dissipation [28]. Carbon-based interphases, such as monolayer pyrolytic carbon (PyC) and multilayer PyC/SiC, are commonly used as the coating onto the fiber surfaces before the matrix densification, due to their irradiation resistance [28]. These interphases are typically created using chemical vapor deposition (CVD) [24]. The thickness of the PyC interphase significantly affects the composite's performance. If the interphase is too thin, it may lead to brittle failure due to excessive frictional stress. Conversely, if it is too thick, it can reduce the effectiveness of the load transfer between the fiber and the matrix [29-33]. For SiC/SiC CMCs, which consists of Generation III SiC fibers and CVI SiC matrices, an optimal PyC interphase thickness ranges between 50 and 200 nm. While thicker interphases might reduce irradiation tolerance, experimental observations have not identified significant disadvantages [34]. The typical CVD PyC interphase in a nuclear-grade SiC/SiC CMC is mostly anisotropic with the basal planes slightly to moderately aligned parallel with the fiber surface [34]. Additionally, boron nitride (BN) is a potential alternative interphase material, but only when isotropic $^{11}$BN is used to minimize problems like boron burnup and helium production caused by $^{10}$B (n, a)$^{7}$Li transmutation reactions under irradiation, which pose serious harm to the composite strength [35].

### *2.2.3 Matrix and Composite*

The fabrication methods for the matrix and composite are described briefly as follows:

i. CVI: Developing SiC/SiC CMCs for nuclear applications focuses on achieving stoichiometric, high-purity, and highly crystalline SiC fibers and matrices [36]. CVI is the most reliable method for fabricating these high-purity, highly crystalline SiC matrices, which are essential for irradiation resistance [24]. The CVI process involves CVD of SiC onto the surfaces of reinforcing fibers, using precursors such as methyltrichlorosilane (MTS) or ethyltrichlorosilane (ETS) that are carried by hydrogen gas [37]. With deposition temperatures ranging from 1000 to 1200 °C, CVI is considered a low-temperature technique that minimizes damage to fibers and reduces residual thermal stress. This process yields a high-purity, highly crystalline β-SiC matrix with relatively high strength and high thermal conductivity. The deposition rate is a critical factor in this process – higher rates result in greater internal porosity, while lower rates reduce porosity but increase fabrication

times. Achieving a dense matrix is important, as it enhances the mechanical strength and thermal properties of the composite [38].

ii. Nanopowder infiltration and transient eutectic phase (NITE): The NITE process has demonstrated the ability to produce nearly fully dense SiC/SiC CMCs with radiation resistance, making it a promising alternative to the CVI method [39]. Developed at Kyoto University, NITE is a liquid-phase sintering process that uses additives such as $Al_2O_3$, $Y_2O_3$, and $SiO_2$ to achieve densification [40-42]. The process involves impregnating a SiC fiber preform with a slurry of SiC powder and additives, drying it into prepreg sheets, and then hot pressing them at temperatures above 1800 °C [42]. Tyranno-SA fiber, which is known for its thermal stability above 1800 °C, is used in this process. The resulting composite reaches a density of 3.1 g/cm³, close to the ideal density of crystalline SiC (3.21 g/cm³), with open porosity below 1% [42]. The reported properties of the composite include an ultimate tensile strength of approximately 400 MPa and thermal conductivity of 30 W/m·K[43]. Efforts are currently underway to industrialize the NITE process for broader applications [44].

iii. Polymer impregnation and pyrolysis (PIP): PIP is a traditional method for fabricating SiC/SiC CMCs and is valued for its ability to produce large, complex components with controlled microstructures at a relatively low cost [45]. The process involves repeated cycles of impregnating fiber preforms with a liquid silicone-organic polymer precursor, followed by pyrolysis to form the SiC matrix. However, achieving high density is challenging due to volume shrinkage and gas evolution during ceramization [45]. Innovations, such as using polyvinylsilane (PVS) instead of polycarbosilane (PCS) and optimizing curing conditions, have improved density of PIP-based SiC CMCs to approximately 70% [46]. However, issues like radiation instability and microcracking during crystallization limit the suitability of using PIP-based SiC CMCs for nuclear applications [47].

iv. Melt infiltration (MI) or liquid silicon infiltration (LSI): The MI process, enhanced by a fine-tuned reaction sintering (RS) technique, has been developed to fabricate SiC CMCs [48]. This process involves infiltrating a mixed slurry of SiC and carbon particulates into the SiC fiber preform under a hydraulic pressure of approximately 6 MPa [45]. Following this, molten silicon is infiltrated into the preform, and a RS process occurs. The molten silicon reacts with the free carbon to create a silicon carbide bonding matrix at a temperature of 1400 °C in a vacuum [45], with residual silicon also remaining. By optimizing the composition and particle size of raw materials, the residual silicon phase can be minimized. For Hi-Nicalon SiC fiber/fine-tuned RS SiC matrix composites, density, and thermal conductivity values reached 2.8 g/cm³ and 49 W/m·K, respectively [45]. The most anticipated practical hindrances for use of conventional MI SiC in nuclear applications have been high temperature and irradiation instability due to the networked silicon [49].

The limitations of the above methods include:

i. Both CVI and PIP may require long processing times, as several cycles of densification are required compared to other methods. Additionally, CVI requires complex equipment and higher temperatures.

ii. The NITE method can face the challenge of improper infiltration of the matrix between the fiber bundles (because of the high surface area of the nanopowder) resulting in pores between the fiber bundles [50].

iii. The MI or LSI method can lead to the formation of residual silicon phase in the matrix which are detrimental to the strength of the composite and limit the operational temperature.

## 2.3 Impurity Limits

ASTM C1783 and ASTM C1793 provide guideline specifications for C/C [20] and SiC/SiC [51] CMCs. These guidelines outline how to specify the constituents, the structure, the desired engineering properties, methods of testing, manufacturing process requirements, the quality assurance requirements, and traceability for CMCs for nuclear reactor applications. The need for these guidelines arises, in part, from the absence of industry-wide material specification standards relating to fiber architecture, composition, and manufacturing processes.

### *2.3.1 C/C Composites*

Fiber-reinforced C/C composites face several manufacturing constraints, particularly when designed for nuclear applications. The production process requires precise control over fiber architecture, matrix composition, and the alignment of reinforcements to achieve specific performance properties. For nuclear applications, it's crucial to control impurity levels in C/C composites, as high impurity levels can lead to increased neutron absorption, oxidation catalysis, and nuclear activation. Issues such as high ash content and uneven distribution of fibers or matrix materials can create localized weaknesses and reduce overall performance [20]. ASTM C1783 includes a list of acceptable chemical impurity limits for nuclear-grade graphite and carbon, as shown in Table 2.1. The impurities are categorized as neutron-absorbing impurities, oxidation-promoting catalysts, nuclear activation relevant impurities, metallic corrosion relevant impurities, and fissile/fissionable elements [20]. These suggested limits provide guidelines on the allowable amount of chemical impurities, when manufacturing carbonaceous materials for nuclear applications. Additionally, environmental factors also present risks, necessitating protective surface seal coatings to mitigate oxidation and corrosion in high-temperature reactor environments.

Table 2.1: Chemical purity requirements for C/C composites in nuclear applications given in ASTM standard C1783.

| Test | ASTM Test | High Purity (ppm) | Low Purity (ppm) |
|---|---|---|---|
| Ash Content | C561 | 300 maximum | 1000 maximum |
| Chemical Impurity - Ca | D5600 | < 30 | < 100 |
| Chemical Impurity - Co | D5600 | < 0.1 | < 0.3 |
| Chemical Impurity - Fe | D5600 | < 30 | < 100 |
| Chemical Impurity - Cs | D5600 | < 0.1 | < 0.3 |
| Chemical Impurity - V | D5600 | < 50 | < 250 |
| Chemical Impurity - Ti | D5600 | < 50 | < 150 |
| Chemical Impurity - Li | D5600 | < 0.2 | < 0.6 |
| Chemical Impurity - Sc | D5600 | < 0.1 | < 0.3 |
| Chemical Impurity - Ta | D5600 | < 0.1 | < 0.3 |
| Boron Equivalent | C1233 | 2 maximum | 10 maximum |
| Chemical Impurity - N | TBD | TBD | TBD |
| Chemical Impurity - S | C816 | TBD | TBD |

### *2.3.2 SiC/SiC Composites*

The manufacturing of SiC/SiC composite structures for nuclear applications faces notable challenges. Fabrication involves processes such as CVI, MI, pyrolysis, and hot pressing, each requiring strict control over variables like precursor composition, process conditions, and matrix density. Impurity control is critical for nuclear applications to prevent neutron absorption, impurity catalyzed oxidation, and other impurity catalyzed reactions. High purity and crystallinity silicon carbide fibers and matrices are essential to ensure mechanical and chemical stability under radiation and high-temperature environments. ASTM C1793 does not provide a specific list of chemical impurity limits for nuclear-grade SiC/SiC composites; it suggests the chemical impurity limits recommended for graphite (Table 2.1) could be extended to silicon carbide as well [51].

# 3 Structural and Failure Analysis Methods for CMCs

CMCs are advanced engineered materials designed to overcome the inherent brittleness of monolithic ceramics. By incorporating ceramic fibers into a ceramic matrix, these composites offer enhanced mechanical properties such as increased toughness, thermal shock resistance, and damage tolerance. These attributes make CMCs ideal for high-temperature applications. Despite their robustness, CMCs are susceptible to various failure modes due to their intricate microstructure and anisotropic properties. This chapter provides a comprehensive overview of the structural failure modes in CMCs, discusses the methodologies for modeling these failures, and highlights the importance of progressive failure analysis in predicting and mitigating damage in these materials. In addition, the chapter includes detailed discussion on the modeling of SiC/SiC CMCs behavior under various loading conditions, focusing on mechanisms like creep, fatigue, and oxidation-assisted stress rupture. The chapter discusses the challenges and modeling strategies for SiC/SiC CMCs in nuclear applications, where materials face high-dose irradiation and significant thermal gradients.

## 3.1 Structural Failure Modes in CMCs

Understanding the failure mechanisms is critical for reliable design and performance prediction of CMCs under extreme conditions. The following discusses the structural failure modes in CMCs as identified in literature.

### *3.1.1 Matrix Cracking*

Matrix cracking is one of the most common failure modes in CMCs and often represents the initial stage of damage during service, when the ceramic matrix is subjected to tensile stresses that exceed its inherent fracture strength [52-59]. Due to the brittle nature of ceramics, the matrix lacks the ability to undergo significant plastic deformation, resulting in the formation of microcracks that can propagate through the material and compromise its structural integrity. These cracks can also create pathways for oxygen and other reactive species to penetrate deeper into the composite, triggering oxidation and chemical degradation [60, 61].

Several factors influence matrix cracking, including thermal stresses caused by high temperature gradients, mechanical loading from tensile or bending forces, and pre-existing defects such as pores or inclusions that act as stress concentrators. While matrix cracking is not necessarily catastrophic in CMCs due to the load-sharing capability of the reinforcement phase, it can trigger other failure mechanisms, such as fiber-matrix debonding, which ultimately degrade the composite's overall performance. The ultimate load-bearing capacity of a CMC can significantly surpass the load at which matrix cracking first occurs. However, the initial occurrence of matrix cracking is critically important, as it marks the onset of permanent damage, the loss of the matrix's ability to protect the fibers from corrosion and oxidation, and an increase in vulnerability to degradation under cyclic loading.

### *3.1.2 Fiber-Matrix Debonding*

Fiber-matrix debonding refers to the separation of the reinforcing fibers from the surrounding matrix, which occurs when the interfacial shear strength between the fiber and matrix is insufficient to transfer loads effectively [52-59]. This failure mode can be influenced by several factors, including weak interfacial bonding caused by poor adhesion which makes the interface vulnerable to mechanical or thermal stresses. Matrix cracking can also contribute to debonding as cracks propagate to the fiber-matrix interface and disrupt the bond. Additionally, mismatch between matrix and fiber CTE can induce interfacial stresses that lead to debonding.

Controlled debonding, however, can be desirable for energy dissipation by helping to absorb and redistribute stresses within the CMC [62, 63]. While controlled debonding can enhance toughness, extensive debonding reduces the efficiency of load transfer from the matrix to the fibers and diminishes the composite's overall strength and stiffness. Excessive debonding can also facilitate crack propagation and fiber pull-out. Balancing the degree of debonding is therefore critical to optimizing the performance and durability of CMCs.

### *3.1.3 Fiber Fracture*

Fiber fracture occurs when the reinforcing fibers, which are the primary load-bearing elements in CMCs, fail under tensile or compressive loading [52-59]. This failure mode is particularly critical because the fibers provide the composite with its strength and toughness. Several factors contribute to fiber fracture, including stress concentrations at fiber-matrix interfaces or near matrix cracks, which can lead to localized fiber breakage. Repeated cyclic loading or fatigue can progressively weaken the fibers over time and eventually cause them to fracture. Additionally, environmental effects such as high temperatures and oxidative conditions can degrade the fibers by reducing their strength and making them more susceptible to failure.

The consequences of fiber fracture are significant as it diminishes the composite's ability to carry loads and results in a substantial drop in mechanical performance. In severe cases, widespread fiber failure can lead to catastrophic structural collapse, compromising the integrity and functionality of the CMC component.

### *3.1.4 Fiber Pull-Out*

Fiber pull-out occurs when, following matrix cracking and interface debonding, fibers are partially or fully extracted from the matrix rather than fracturing immediately [52-59, 64-66]. This mechanism is influenced by factors such as interfacial strength, where weaker bonding between the fiber and matrix promotes pull-out, and the extent of matrix cracking, which creates pathways for fiber disengagement. The mechanical toughness of the fibers further dictates the effectiveness of this mechanism. Tougher fibers are more capable of undergoing significant pull-out without premature fracture, allowing greater energy dissipation through the frictional work of sliding. In contrast, brittle fibers are prone to breaking rather than pulling out, which limits their contribution

to energy absorption via this mechanism, as they cannot sustain the stresses required for sustained sliding.

Fiber pull-out has both beneficial and detrimental implications for composite performance. On the positive side, it contributes to toughness enhancement by dissipating fracture energy during crack propagation, enabling gradual failure rather than the abrupt, brittle fracture seen in monolithic ceramics. Conversely, excessive pull-out can reduce the composite's stiffness and load-bearing capacity which ultimately compromises structural integrity. Therefore, achieving an optimal balance – promoting sufficient pull-out for energy dissipation while maintaining effective load transfer –maximizes the performance and reliability of CMCs.

#### *3.1.5 Delamination*

Delamination is a failure mode characterized by the separation of layers within a composite and is often observed in CMCs with laminated structures or regions where the matrix and reinforcement are not uniformly distributed [52-59, 67, 68]. This separation typically occurs due to interlaminar stresses, which are out-of-plane forces induced by bending, impact, or other mechanical loads. Defects such as voids or weak interfacial bonds between layers can act as initiation sites for delamination which further compromises the structural integrity of the composite. Additionally, thermal cycling can generate interlaminar stresses that exacerbate this failure mode.

The consequences of delamination are significant, as it reduces the composite's load-bearing capacity and stiffness, impairing its ability to perform under mechanical loads. Furthermore, delamination exposes internal surfaces to environmental degradation, such as oxidation and corrosion, which can accelerate material weakening and compromise long-term durability. Managing delamination is important for ensuring the reliability and performance of CMC components.

### 3.2 Structural Failure Analysis

#### *3.2.1 Overview of Failure Models*

CMCs exhibit complex fracture phenomena because their brittle matrices can crack at low strains, yet the presence of reinforcing fibers often provides bridging mechanisms that stave off abrupt, catastrophic failure. Fundamentally, the design of such composites must balance matrix toughness, fiber strength, and interface properties to achieve the desired balance between stiffness and damage tolerance. Failure modeling approaches for CMCs can be broadly divided into phenomenological, semi-empirical, micromechanical (including fracture mechanics and shear-lag theory), continuum damage, and statistical classes, each of which provides different insights and trade-offs in predictive power [69].

Phenomenological models emerged when laminate strength predictions were first adapted from isotropic metal criteria. The maximum stress or maximum strain approach simply requires that a unidirectional lamina "fails" whenever a principal stress or strain exceeds the experimentally measured strengths in that direction. Slightly more advanced theories, such as Tsai–Hill [70] or Tsai-Wu [71], create polynomial-based surfaces in stress space and allow limited interaction terms between different stress components. Despite their simplicity and practical value in early design phases, these approaches neither account for the progressive mechanics of crack formation and growth, nor capture local phenomena like fiber pull-out or matrix bridging. Consequently, while they remain easy to implement with finite element analysis and require only minimal data (e.g., strengths in the fiber directions), they may prove inadequate to quantify precisely how internal microcracks form, link up, and trigger global failure in a ceramic environment.

Semi-empirical criteria adapt linear elastic fracture mechanics concepts to higher-level laminate behavior by positing that an "intense energy" or "damage" region surrounds the crack tip. Methods proposed by Waddoups et al. [72] and Whitney–Nuismer [73, 74] rely on correlating the nominal stress at a hole or crack to a matrix fracture toughness modified by a characteristic length. Such characteristic distances or toughness terms must be calibrated through notched and unnotched tension tests, resulting in models that work well for certain configurations of polymer matrix composites. However, CMCs bring additional complexities such as fiber-matrix friction, temperature-sensitive oxidation or embrittlement near cracks, and strong but brittle matrices that do not necessarily follow the same scale of damage localization. Although one can still infer characteristic lengths from tests on ceramic-based systems, these models often collapse intricate fiber bridging and debonding details into a single phenomenon that limits extrapolation to novel material systems or complex geometries.

In micromechanical approaches, a key starting point has been the classical shear-lag analysis by Hedgepeth [75], which describes how load in a unidirectional composite redistributes when a fiber breaks. Because the matrix is assumed to transfer load purely through shear, the stress in adjacent, unbroken fibers can increase significantly. Subsequent refinements allowed for matrix yielding or splitting, which are used to represent some polymeric systems but are not fully transferrable to brittle ceramic matrices. CMCs can carry considerable axial load in the matrix before it cracks, after which the role of frictional sliding or debonding at the interface can become dominant. Simple shear-lag approaches rarely address such abrupt changes, nor do they inherently capture multiaxial stress states, so extensions that incorporate interface friction laws or pre-existing matrix microcracks are required for CMC assessments [69]. These improvements can still give valuable local information about how a break in one fiber elevates the stress in neighbors, but further modeling work is usually needed to describe the full path to final fracture.

Fracture mechanics perspectives go further by tackling the evolution of matrix cracks, fiber bridging, and associated energy balances. One pioneering description, introduced by Aveston et al. [76], treats the energy required to propagate a crack in a brittle matrix reinforced with continuous fibers and shows

how multiple transverse cracks can form in the matrix if the fiber has sufficiently higher ultimate strain or if the interface debonds in a controlled manner. Budiansky et al. [77] established a steady-state notion for these bridging cracks: once a crack extends beyond a certain length, the far-field stress required for it to continue growing remains constant, implying a crack propagation mode that is less sensitive to crack size than in monolithic ceramics. Similarly, Marshall et al. [78] studied how frictional fiber bridging mechanisms reduce the crack tip stress intensity, thereby sustaining composites at stress levels higher than those at first matrix cracking. These approaches explicitly incorporate parameters like interface shear strength, fiber radius, and matrix fracture toughness to link microstructural design variables to global failure loads. The approaches require, however, careful characterization of slip or debond initiation and the validity of assumptions like evenly spaced fibers or purely axisymmetric cracks when applied to real parts, where weaving or 2D/3D fiber architectures may trigger more complicated crack patterns.

Another option is to treat damage as an evolving field in a continuum sense, which is the thrust of continuum damage mechanics. The simplest variant uses a scalar damage variable that decreases elastic stiffness with the accumulation of defects [79]; more refined models adopt tensor variables that distinguish directional cracks in the composite's microstructure [80, 81]. For ceramic systems, matrix cracks often localize into one or several dominant macrocracks, challenging the premise of homogenous microcracks on which many continuum models rely. In principle, multi-variable formulations can combine progressive fiber breaks, interface debonding, and matrix cracking [82, 83]. Such attempts can yield broad coverage of material states in a single finite element simulation, though the complexity of capturing abrupt brittle fracture, bridging, and random flaw distributions often necessitates mixing continuum damage approaches with explicit fracture process zone or cohesive models. As a result, while damage mechanics can be a powerful method for global structural analysis, the fidelity of these models hinges on how accurately they represent the unique fracture processes in a brittle matrix with frictionally constrained fibers.

Statistical failure theories are used because both fiber and matrix in CMCs are fundamentally brittle, and thus significant scatter in strength data often arises. By treating flaw populations via Weibull distributions, engineers can predict the probability that a given volume of composite contains a critical defect. Some approaches extend phenomenological formulations to incorporate weakest link arguments in each stress component [84, 85], while others focus on the ultimate fiber bundle strength once the matrix has cracked [86, 87]. In a chain-of-bundles model, the composite is divided into segments in which a small fraction of fibers has failed, load then shifts to adjacent fibers, and, if those fibers are also weak, the break can cascade. Local load-sharing rules often encapsulate the severity of stress concentrations in neighboring fibers, but these must be adapted carefully for CMCs to reflect any frictional pull-out or bridging that might keep load-carrying capacity intact, even as multiple fibers fracture. With sufficient test data and appropriate micromechanical rules, hybrid "mechanistic-statistical" models offer a better approach – they capture how many small fractures can accumulate

before the entire composite fails, and they provide crucial reliability assessments for high-performance applications where the allowable flaw size must remain below critical thresholds.

In summary, modeling failure in CMCs is rarely a one-size-fits-all problem. Phenomenological methods provide a quick, coarse bounding for design criteria. Semi-empirical techniques that borrow from fracture mechanics can account for notch effects when properly calibrated but may hide the finer details of bridging crack growth in a single fitting parameter. Shear-lag models excel at studying the localized consequences of broken fibers or partial matrix splitting, though they can struggle to map the path from small-scale damage to full structural failure. Meanwhile, fracture mechanics frameworks that integrate matrix toughness, interface shear behavior, and fiber bridging are highly instructive, often being the most realistic for capturing how a nominally brittle ceramic can carry more load through crack bridging well beyond the first matrix crack event. Continuum damage mechanics tries to unify these micro-level features within large-scale structural simulations, but it must be tailored to reflect discrete microcrack patterns. Finally, statistical models become essential wherever random flaw distributions and brittle fracture combine to create a wide scatter in observed strengths. In practice, designers frequently couple more than one approach, using simple phenomenological checks or semi-empirical correlations for early screening and then relying on fracture-based and statistical frameworks to refine estimates of safe operating stresses, reliability, and lifespan.

### *3.2.2 Progressive Failure Analysis*

CMCs exhibit progressive rather than catastrophic failure behavior, characterized by a sequence of microscale damage events that gradually degrade the material's load-bearing capacity. Failure typically initiates with brittle cracking of the ceramic matrix at stress concentrators, but the composite architecture is intentionally designed to manage this damage. Cracks are often deflected along the fiber-matrix interfaces, reducing the likelihood of direct fiber breakage and enabling stress redistribution to intact fibers. When these interfaces are engineered with low shear strength, debonding can occur which allows cracks to propagate along the interface without severing the fibers. This mechanism facilitates fiber bridging, where unbroken fibers span the crack faces and reduce the stress intensity at crack tips, thereby increasing the toughness of the composite. With further loading, the fibers may eventually fail or be pulled out, but because matrix cracking precedes full fiber failure, CMCs are able to dissipate far more energy than monolithic ceramics.

Progressive Failure Analysis (PFA) is a computational methodology used to simulate this staged damage evolution in CMCs [88-90]. Leveraging continuum damage mechanics and finite element methods, PFA models the sequence of matrix cracking, interface debonding, fiber bridging, and eventual fiber failure. The foundational principle of PFA is the iterative tracking of damage initiation and growth within each constituent – matrix, interface, and fiber – through simulations that reflect the anisotropic and heterogeneous nature of CMCs. At each load increment, a nonlinear analysis determines the equilibrium state without altering the material properties. The resulting stress field within each lamina is then compared against failure criteria. When failure is detected

in a lamina, its material properties are modified using a damage model, and the equilibrium is recalculated to account for the changes. This iterative process continues until no new failures are detected at a given load step, at which point the load is increased and the process repeated until catastrophic failure occurs.

Figure 3.1 illustrates the steps in a typical PFA approach. Effective PFA requires five core capabilities [88]: (1) a nonlinear solver to establish equilibrium; (2) a robust stress recovery procedure to compute local lamina stresses; (3) failure criteria to identify damage initiation and failure modes; (4) damage or degradation models to update material properties post-failure; and (5) a procedure for reestablishing equilibrium after updating properties. The analysis begins with accurate micro- and macro-mechanical characterizations of the composite. Finite element models typically discretize the structure at the ply level and incorporate anisotropic constitutive laws and failure criteria that distinguish among damage modes such as matrix cracking, fiber breakage, pull-out, interface debonding, and delamination.

Failure criteria in PFA are broadly classified as non-interactive and interactive. Non-interactive criteria, such as the maximum stress and strain theories, assess individual stress or strain components against allowable values without accounting for interaction effects. In contrast, interactive criteria include polynomial theories (e.g., Tsai-Wu [71]), direct-mode determining theories (e.g., Hashin [91]), and strain energy-based criteria (e.g., Christensen [92]), which consider interactions among stress components and often distinguish between failure modes. While polynomial-based criteria like Tsai-Wu offer generality, they may not specify failure modes, limiting their utility for modeling damage evolution. More useful in PFA are direct-mode determining criteria that separately define failure envelopes for fiber tension, fiber compression, matrix tension, and matrix compression.

Once failure is identified, material property degradation models update the local stiffness and strength. These models fall into three categories: instantaneous unloading, gradual unloading, and constant-stress assumptions [93]. Instantaneous unloading sets affected properties to zero immediately upon failure, whereas gradual unloading degrades properties progressively based on damage evolution – often following exponential or linear trends. Constant-stress models (e.g. [94]) assume that a failed lamina continues to carry its pre-failure load until global failure ensues. Various degradation strategies – such as ply-discount theories [95], exponential models [96], and Weibull-distribution-based methods – have been developed, and each are tailored to specific failure modes and composite architectures.

An advantage of PFA is its ability to capture subcritical damage and pseudo-ductile behavior – such as crack bridging – that is unaccounted for in traditional elastic–brittle analyses. PFA not only predicts when and how failure will occur but also provides detailed insight into the sequence and spatial distribution of damage. This information supports the design of damage-tolerant and

fail-safe components. As advanced CMCs incorporate nanofillers, graded interfaces, and hybrid fiber architectures, PFA frameworks are being upgraded to include refined micromechanical models and cohesive zone formulations. These developments enhance the physical fidelity of simulations, accounting for the interplay of chemical, thermal, and mechanical effects across length scales.

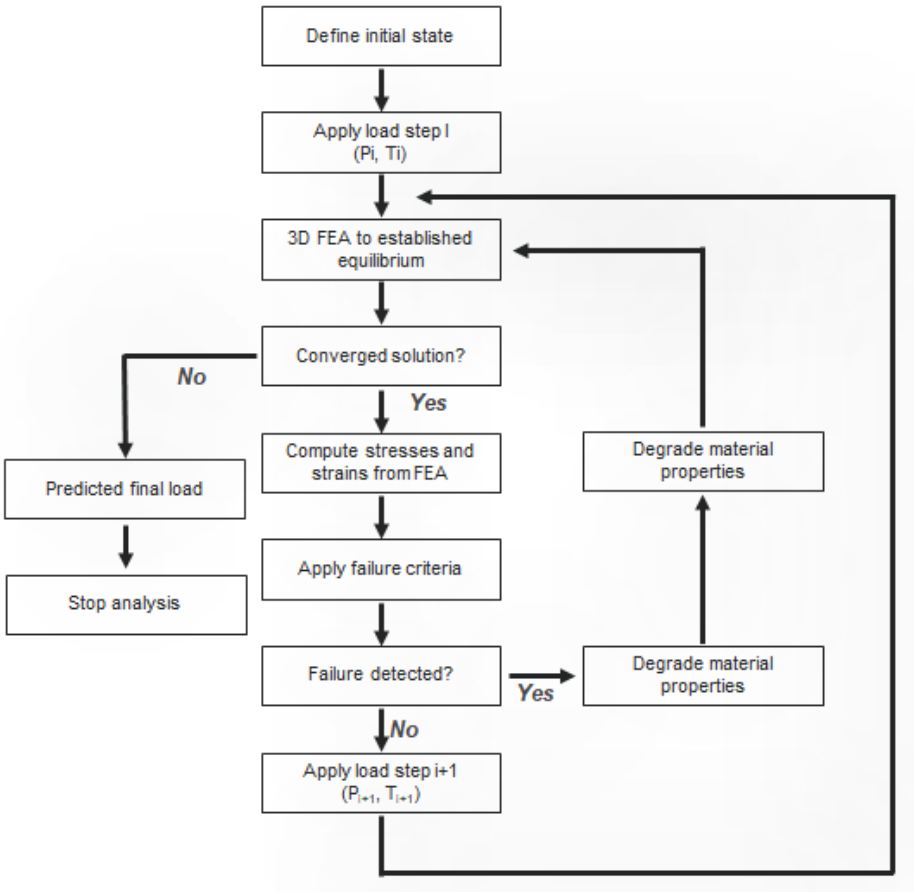


Figure 3.1. Typical steps in a PFA.

### 3.3 Time-Dependent Modeling of SiC/SiC CMCs

At temperatures between 700 °C and 950 °C, SiC/SiC composites are susceptible to oxidation-assisted stress rupture, commonly referred to as "pesting," where severe embrittlement occurs well below the pristine ultimate strength [97]. This degradation is driven by oxidation-induced chemical and thermomechanical interactions that weaken SiC fibers over time. Several mechanisms have been proposed, including fiber fusion into the matrix due to BN coating oxidation [98], tensile stress buildup from silica scale formation on the fiber surface [99], wedging action from oxide growth within matrix cracks [100], and oxidation-facilitated flaw growth within fibers [101].

While many micromechanical models capture aspects of oxidation degradation, most are limited to one-dimensional formulations and lack extension to multiaxial stress states suitable for finite element analysis [102]. Recent efforts by Cluzel [103] and Genet [104] have integrated oxidation damage with mechanical degradation in finite element analysis (FEA) frameworks to enable component-scale life predictions.

At higher temperatures, typically above 950ºC, the long-term behavior of SiC/SiC CMCs is dominated by creep and fatigue mechanisms influenced by both the constituent material properties and their interactions under thermomechanical loading. A primary creep mechanism in these composites involves stress redistribution between the fiber and matrix phases due to their different creep resistances. When the less creep-resistant matrix deforms, load is transferred to the stiffer SiC fibers, potentially leading to cracking in the fibers. This initiates a damage accumulation cycle in which cracked regions transfer load back to the matrix, promoting further creep deformation and eventual rupture once either constituent reaches its failure threshold [105, 106]. Similar stress redistribution and degradation mechanisms have been observed under fatigue load. The progressive weakening of the composite under cyclic loading can result from fiber degradation, matrix microcracking, delamination, and interfacial debonding [107-109].

A unique feature of high-temperature damage evolution in SiC/SiC CMCs is the phenomenon of crack sealing [102, 110]. Under oxidizing environments, oxides such as $SiO_2$ or other glassy phases formed at the fiber-matrix interphases can infiltrate and seal existing matrix cracks. This can lead to partial recovery of the material's elastic stiffness by closing microcracks. However, the filled glassy material is generally weaker and more compliant than the parent composite, leading to a reduction in ultimate strength and potentially masking damage that can still propagate under continued loading [102, 111].

To capture the complex behavior of SiC/SiC composites at high temperatures, a range of micromechanical and continuum-scale modeling approaches has been developed. Early models [112-114] were primarily one-dimensional and aimed to simulate basic creep deformation mechanisms in the fiber and matrix phases. While these provided important insights at the microscale, their applicability was limited under multiaxial stress states relevant to component-scale design. To overcome this limitation, three-dimensional viscoplastic models [115-116] incorporating progressive damage were introduced, often using the method of cells to represent fiber-level interactions. Other approaches have integrated creep-deformation and creep-rupture mechanisms within a unified framework, enabling full-field simulations of structural components subjected to high-temperature environments [117-119]. These models capture the coupled effects of temperature, time, and stress on damage initiation and evolution.

Multiscale modeling techniques have also been widely adopted. Among them, the Generalized Method of Cells (GMC) has supported the development of advanced computational tools capable

of tracking time-dependent damage across spatial and temporal scales. These tools are designed to integrate experimental data with FEA for robust simulation of CMC components under creep loading.

Fatigue modeling of SiC/SiC composites at high temperatures has progressed from basic phenomenological models to more advanced, physics-based multiscale approaches. Early efforts used slow crack growth techniques [120] and energy-based damage evolution laws [121] to describe fatigue damage accumulation during cyclic loading. Building on this foundation, multiscale modeling frameworks [122, 123] have been adapted to capture the influence of material heterogeneity, incorporating random microstructures that reflect the inherent variability in fiber architectures. A hybrid approach [124] that combines macroscopic simulations with micromechanical submodels – such as those based on shear-lag theory for fiber-matrix load transfer – have shown strong alignment with experimental trends.

Recent developments include a progressive creep-fatigue damage analysis framework that integrates multiscale micromechanical models with experimental calibration [125]. This method accounts for combined effects of creep, high-temperature fatigue, oxidation, and interface degradation, and has been validated against experimental data for components such as turbine blades. These tools enable more accurate prediction of damage evolution and component life under complex thermomechanical loading, supporting the design of more reliable and durable SiC/SiC CMC systems in high-performance applications such as high-temperature nuclear reactors.

### 3.4 Irradiation-Induced Damage Modeling of SiC/SiC

SiC/SiC CMCs are currently being explored for potential applications in nuclear reactors, particularly as core components such as control rod sheaths and cladding, which face high-dose irradiation as well as significant thermal gradients. Despite these challenges, there is a lack of macroscopic constitutive models that fully address the combined effects of these conditions. A key phenomenon induced by radiation is volumetric swelling, an inelastic expansion resulting from the accumulation of neutron-induced defects like microvoids and dislocation loops. This swelling occurs independently of external stress, is indicative of the level of irradiation damage, and affects the mechanical and thermal properties of materials in nuclear settings.

Efforts to model the thermomechanical behavior of SiC/SiC fuel cladding under irradiation have been documented in several studies [126-131], especially under conditions that surpass the material's proportional limit stress, such as during shutdown transients or at high burnup levels. Noteworthy developments include phenomenological models that adjust for irradiation impacts by altering the elastic modulus and introducing a pseudo-plastic response driven by matrix cracking thresholds [127-128]. These models represent significant progress toward the predictive modeling of CMCs under complex loading conditions. Although these models have facilitated the design and prediction of the nonlinear mechanical behavior of SiC/SiC cladding, a continuum damage

model rooted in a consistent thermodynamic framework was absent until recently. Alabdullah et al. [131] introduced such a model – a thermodynamically consistent continuum damage mechanics model tailored for SiC/SiC CMCs under severe thermal and radiation conditions. This model integrates elastic, inelastic, thermal, and swelling strains, along with damage from high temperature gradients and radiation. Damage is broken down into three scalar components for computational efficiency and linked with thermal conductivity via a damage-modified Fourier law. The model also accounts for the degradation of proportional limit stress (PLS) due to radiation. Implemented in COMSOL and validated against mechanical and irradiation data, the model shows promising alignment, particularly under high-dose ($\geq$ 40 dpa) scenarios, revealing an early onset of nonlinear behavior, increased damage, and diminished stress capacity under irradiation. However, further refinement of damage evolution laws for thermal gradients and experimental calibration of thermal conductivity degradation functions are necessary for enhanced accuracy.

# 4 Material Properties and Nuclear Reactor Environment Effects

Radiation-induced defects in ceramics, whether isolated or clustered, can significantly affect the material and its properties, leading to swelling, anisotropic deformation, irradiation creep, thermal conductivity loss, and mechanical degradation. Literature data was reviewed to show the effects of irradiation on C/C and SiC/SiC CMCs material properties, where properties were tested as per the standards mentioned in Table 4.1. Material properties are visually compared using bar plots, where the bar height indicates the average value for each property. Scatter bars display the range of reported values from the literature, showing the minimum and maximum observed values. The 'Unirradiated' bar represents a composite of property values from open literature, establishing a baseline. To highlight the impact of nuclear irradiation, an 'Irradiated' bar is added, showing how property values change upon neutron exposure.

## 4.1 C/C Composites Properties (unirradiated and irradiated)

Graphite has long been used in gas-cooled reactors as both a moderator and a structural material, providing a strong foundation for understanding how C/C CMCs behave under irradiation. While individual graphite components in C/C composites exhibit similarities to anisotropic graphite blocks, their overall response to irradiation is influenced by factors such as preform architecture and composite structure [16, 20]. Graphite's microstructure consists of graphene layers with the <*a*> axis parallel and the <*c*> axis perpendicular to these sheets. Under neutron irradiation, carbon atoms are displaced from their lattice positions into interstitial sites, leaving vacancies in the basal planes [132]. At higher temperatures, interstitial carbon atoms are more mobile, forming clusters and eventually generating new planes. Initially, neutron damage strengthens graphite by pinning dislocations in the basal planes which increases elastic modulus, but continued irradiation alters the polycrystalline structure due to defect accumulation which can lead to lattice distortion, grain boundary disruption and potentially cause dimensional changes, microcracking, and eventual embrittlement of the material [132]. Thermal conductivity also decreases with irradiation as irradiation-induced defects scatter phonons and reduce their mean free path. In addition to physical property changes, graphite undergoes dimensional and volume changes when irradiated. Graphite exhibits a distinct turnaround response. Graphite initially shrinks in all directions, with the <*c*> axis strain absorbed by basal plane misalignment and porosity [133]. However, as irradiation continues, the ability to accommodate the <*c*> axis strain saturates reaching a turnaround point, and the newly formed basal planes cause <*c*> axis swelling while the <*a*> axis continues to contract [134]. This turnaround leads to crack formation and severe strength degradation. This behavior is also observed in C-C composites, though their response is further influenced by several factors, including fiber distribution, fiber volume fraction, porosity characteristics, and the structure and crystallinity of both fibers and matrix.

The irradiation behavior of C/C CMCs is more complex and has less data in the literature than for the graphite materials. One of the most critical yet challenging requirements for high-irradiation applications, such as control rod applications, is achieving dimensional stability. A maximum dimensional variation of 2% at operating temperatures is generally considered acceptable for such

applications [1]. The material properties presented in this section for C/C CMCs are based on different fabrication methods, including CVI and liquid-phase densification using thermosetting resin or pitch impregnation as discussed in Section 2.1. Irradiation effects are measured by irradiating test samples and then testing as per the standards listed in Table 4.1. Most properties found in the literature were for CVI, Pitch, or a combination of different fabrication processes. Table 4.2 lists the C-C CMC data used in this report for analyzing neutron irradiation effects. The effects of neutron irradiation are further discussed in Sections 4.1.1 and 4.1.2.

Table 4.1: List of standard test methods for CMCs [135].

| Failure mode | | ASTM | JIS | ISO |
|---|---|---|---|---|
| Tensile | Room temp. | C1275 | R1656 | 15 733 |
| | High temp. | C1359 | - | - |
| | Off-axis | D3518 (PMC) | - | - |
| | Trans-thickness | C1468 | - | - |
| | Creep | C1337 | - | - |
| | Fatigue | C1360 | - | - |
| Compressive | Room temp. | C1358 | R1673 | 20 504 |
| Flexural | D5600 | C1341 | R1663 | - |
| Shear | Interlaminar | C1292 | R1643 | 20 504 |
| | Iosipescu (test specimen name) | D5379m | - | 20 506 |
| Fracture energy | In-plane mode-I | - | R1662 | - |
| | Interlaminar mode-I | D5528 (FRP)<br>D6671m (FRP) | - | - |
| Thermal diffusivity | Flash method | E1461 | | |

Table 4.2: Detailed information of C/C CMCs considered in this work.

| Process | Material Reference | Material characteristics | Fiber content (%) | Density ($g/cm^3$) | Porosity (%) | References |
|---|---|---|---|---|---|---|
| CVI | Schunk CF22 | Ex-PAN cloth/$C_{CVI}$ | - | 1.55 | - | [7] |
| | SEPCARB A 3D | 3D $C_{PAN}/C_{CVI}$ | - | 1.77 | - | [136] |
| | Herakles N11 | 3D ex-PAN (x,y) and needled fibers (z, ex-PAN) /$C_{CVI}$ | - | 1.75 | 15 | [8] |
| | Herakles N31 | 3D ex-pitch (x), ex-PAN (y) and needled fibers (z, ex-PAN) /$C_{CVI}$ | - | 1.75 | 14 | [8] |
| | Dunlop 3D | 3D ex-pitch P25 (x), ex-PAN (y) and needled fibers (z, ex-PAN) /$C_{CVI}$ | | | | [8] |
| | - | 3D ex-pitch P120-P130 (x), ex-PAN (y) and needled fibers (z, ex-PAN) /$C_{CVI}$ | - | 1.89 | - | [137] |
| CVI + Pitch | SEP N112 | 2.5D $C_{PAN}/C_{CVI+Pitch}$ | 30 | 1.99 | - | [1] |
| | Herakles NB31 | 3D ex-pitch (x), ex-PAN (y) and needled fibers (z, ex-PAN) / $C_{CVI+Pitch}$ | - | >1.9 | 8 | [8] |
| | Herakles NB41 | 3D ex-pitch (x), ex-PAN (y) and needled fibers (z, ex-PAN) / $C_{CVI+Pitch}$ | - | 1.9 | 5 | [8] |
| | A21 | 2D woven $C_{PAN}$ / $C_{CVI+Pitch}$ | - | 1.64 | - | [136] |
| | Carbone Lorraine A05 | 2.5D $C_{PAN}/C_{CVI+Pitch}$ | - | 1.86 | - | [1, 138] |
| Resin + Pitch | Toyo Tanso CX-270G | 2D $C_{PAN}/C_{Phenol+Pitch}$ | 50 | 1.63 | - | [139, 140] |
| Pitch | FMI 222 | 3D $C_{Pitch}/C_{Pitch}$ | 50 | 1.96 | - | [1, 133] |
| | Toyo Tanso CX-2002U | 3D $C_{PAN}/C_{Pitch}$ | - | 1.64 | - | [8, 141, 142] |
| | FMI A27-130 | 3D $C_{Pitch}/C_{Pitch}$ | - | 2.03 | - | [141] |
| | Mitsubishi MKC-1PH | 1D $C_{Pitch}/C_{Pitch}$ | - | 1.93 | - | [141] |

### *4.1.1 Mechanical Properties*

The effect of irradiation on the mechanical properties of C/C CMCs has been relatively understudied and there is limited data available in literature. Experimental results are available for test samples that were irradiated at (i) 800 ℃ to 10 dpa (i.e. displacement per atom) and at (ii) 600 ℃ to 1.8 dpa. The effects of irradiation on the mechanical properties are shown in Figure 4.1. The measured properties included Young's modulus (GPa), tensile strength (MPa), compressive strength (MPa), compressive strength (MPa) and 4-point flexural strength (MPa).

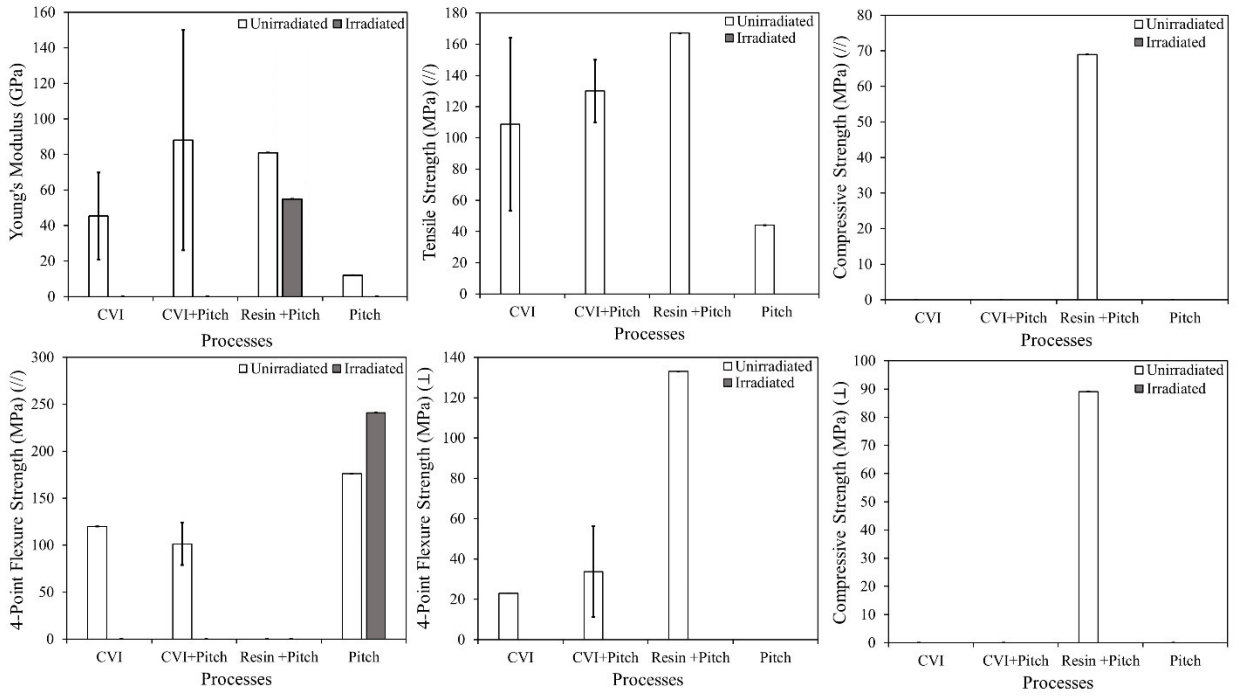


Figure 4.1. Effect of nuclear irradiation on mechanical properties extracted for C/C CMCs from literature.

A study by T. Shibata et al. [139] reported changes in the Young's modulus of 2D C/C (CX-270G) CMCs that were prepared by using resin and pitch impregnation technique following irradiation at 600 °C to a neutron dose of 1.2 dpa. The Young's modulus of CX-270G decreased by about 30% (25 GPa) in the specimen prepared parallel to the fiber lamina and increased by about 30% in the specimen prepared perpendicular to the fiber lamina, which is nearly half the 75% increase observed for conventional nuclear graphite block (grade IG-110). This difference was attributed to the effect of 2D C/C structure compared to IG-110 [139]. Densification occurs through strain relief and closure of internal porosity by the migration of irradiation-induced carbon atoms. The process minimizes microcracks and porosity while effectively pinning dislocations and restricting atomic movement. Consequently, the material becomes stiffer, leading to a notable increase in Young's modulus.

Similarly, the flexure strength of 3D C/C (FMI-222) CMCs fabricated by using the pitch impregnation technique increased by 37% after irradiation at 800 °C to 10 dpa as seen in Figure 4.1. This is due to densification since the neutron irradiation had not yet reached the turnaround point. However, as previously discussed, irradiation beyond the turnaround threshold leads to swelling, which subsequently reduces the mechanical strength. The phenomenon of increasing strength due to neutron irradiation before turnaround is well documented in graphite [142]. However, the turnaround for graphite occurs at lower dpa compared to CMCs. Therefore, the evolution of mechanical properties under irradiation demonstrates the advantages of C/C CMCs over graphite. For example,

graphite under the same radiation conditions (800 ºC to 10 dpa) exhibited swelling and a corresponding 13% decrease in strength [133]. An earlier study by Burchell TD [132] showed that the 3D pitch fiber C/C (FMI-222) CMCs exhibited a continued increase in strength up to ~ 4.7 dpa at 600 °C. In contrast, the 3D PAN fiber C/C (FMI-223) CMCs showed strength gains only up to about 1 dpa, after which strength decreased around 2.5 dpa, likely due to cracking at the fiber-matrix interface.

### *4.1.2 **3.1.2 Thermal and Physical Properties***

Literature data is available for irradiation effects on thermal and physical properties for the following conditions: (i) 820 ℃ and 1.8 dpa, (ii) 1000 ℃ and 1.8 dpa, and (iii) 385 - 775 ℃ and 0.35 - 1.2 dpa. The samples were tested post-irradiation for thermal properties as per the standards mentioned in Table 4.1. The changes in thermal conductivity due to irradiation are shown for C/C CMCs in Figure 4.2. The thermal conductivity was calculated using measurements of thermal diffusivity and specific gravity for each individual specimen and a standard specific heat.

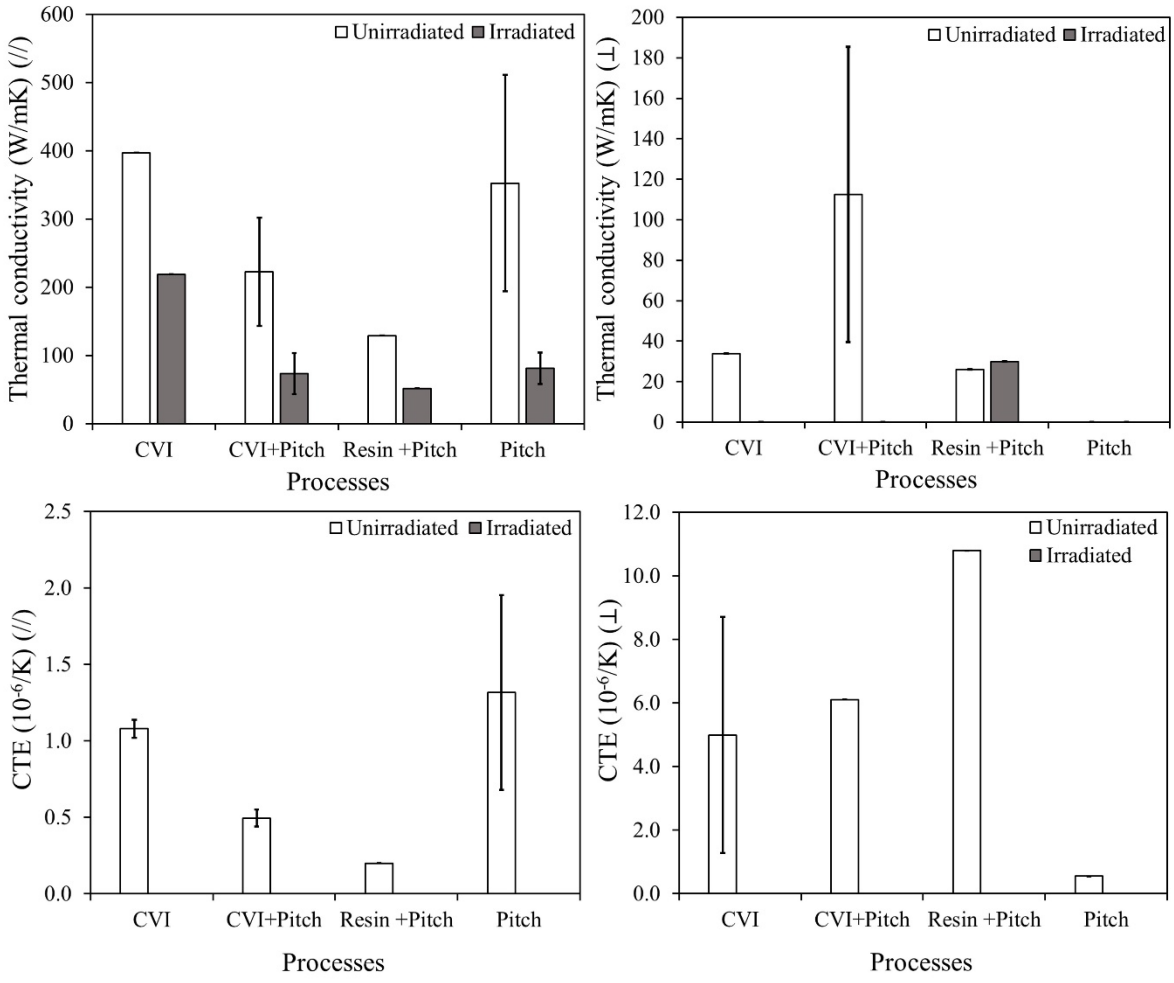


Figure 4.2. Effect of nuclear irradiation on thermal properties extracted for C/C CMCs from literature.

The thermal conductivity of C/C CMCs severely degrades after neutron irradiation at all irradiation temperatures as shown in Figure 4.2. Following irradiation, the thermal conductivity decreases to approximately 40-70% of its original, unirradiated value. The decrease in thermal conductivity of C/C CMCs follows a similar trend as observed in graphite [139, 143]. Neutron damage displaces carbon atoms from their original lattice positions into interstitial sites between graphitic planes [141]. This displacement leads to the formation of dislocation loops or defect clusters, which results in phonon scattering and a subsequent reduction in thermal conductivity. According to T. Shibata et al.[139], in 2D C/C CMCs (CX-270G) fabricated using resin and pitch impregnation techniques and irradiated at 600 ℃ to 1.2 dpa, the decrease in thermal conductivity in directions both parallel to and perpendicular to the composite lamina were similar that of conventional nuclear graphite, IG-110, which experiences approximately a 66% drop. Notably, C/C CMCs with higher initial thermal conductivity before irradiation retained better properties after irradiation. For example, 1D C/C CMCs (Mitsubishi MKC-1PH) prepared via pitch impregnation technique had an initial thermal conductivity of 358 W/m·K at 400 °C and retained a thermal conductivity of 122 W/m·K at 400 °C after irradiation at 420 °C to 0.83 dpa [141]. However, the percentage decrease in thermal conductivity is similar to other C/C CMCs.

Figure 4.3 shows the dimensional change of several C/C composites under irradiation at different temperatures, highlighting the influence of fiber orientation and processing techniques. The 3D pitch-based C/C CMC FMI 222 exhibited significant swelling along the fiber length after irradiation to 2dpa at temperatures above 1000 °C, in association with the friability of the materials, while swelling perpendicular to the fiber axis reached a peak of approximately 1.5% around 1200 °C. In contrast, the 1D pitch-based C/C CMC MKC under the same irradiation condition exhibited shrinkage (i.e. densification) along the fiber axis. Unlike the MKC CMCs, FMI 222 CMCs exhibited swelling rather than shrinkage along the fiber axis, which the author attributed to sample size issues [133]. Therefore, to validate the results, further studies using standardized sample geometries and consistent irradiation conditions are necessary. Next, the 2D PAN-based C/C CMC CX-270G, that was prepared via resin and pitch, swelled after irradiation at low temperature but instead shrank starting at irradiation temperatures around 850 °C and dropped below -6% volume change at ~1200°C; however, there was less change in the perpendicular direction. Overall, CX-270G demonstrated greater dimensional variability than conventional nuclear graphite (IG-110) [1]. Meanwhile, the 2.5D PAN-based C/C N112 showed the lowest dimensional changes in both directions as compared to the others across the temperature range but also has lesser mechanical properties [1]. C/C CMCs are susceptible to irradiation-induced degradation due to anisotropic dimensional changes. The anisotropic dimensional change is driven by irradiation-induced interstitials that create new planes between the existing basal planes leading to swelling in the direction perpendicular to these planes and shrinkage in the direction parallel to these planes. This behavior is also observed in graphitic carbon fibers, influenced by the composite architecture (fibers, preform/fiber design, interfacial coating, matrix). However, it is assumed that the macroscopic behavior in C/C composites is primarily dominated by the fibers [145]. Initially, the carbon fibers shrink

in both diameter (i.e. perpendicular to fiber axis) and length (i.e. parallel to fiber axis) and then swell in diameter while continuing to shrink in length after reaching a turnaround point.

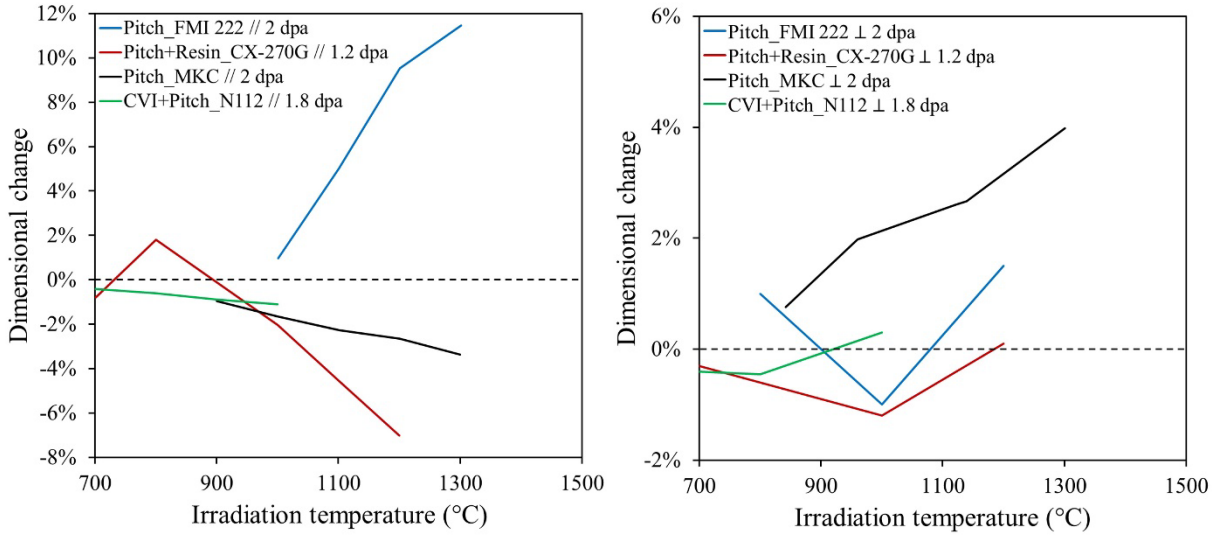


Figure 4.3. Effect of irradiation temperature on the dimensional change of several C/C composites, in one main direction parallel (//, left) and perpendicular (⊥, right) to the fiber axis [138, 145].

Figure 4.4 (left) shows the irradiation-induced dimensional changes in cylindrical specimens of 1D, 2D random fiber composite (RFC), and 3D PAN-based C/C composites irradiated at 600°C to doses up to about 4.5 dpa. The parallel (//) and perpendicular (⊥) directions in the figure are referenced with respect to the cylindrical axis of the specimen. The observed behavior aligns with established theories of graphite's dimensional changes under irradiation, with variations attributed to each composite's unique fiber architecture. For instance, PAN-based graphite fibers consist of radial basal planes aligned parallel to the fiber axis, causing the individual fibers to shrink in length and swell in diameter when irradiated. This trend is particularly evident in the 1D composite as all the fibers are aligned in the cylindrical axis of the specimen. At doses below 1 dpa, the dimensional change in the 1D composite is relatively small. However, as the dose increases, the shrinkage along the fiber axis becomes more pronounced, while the perpendicular direction remains largely unaffected until around 2 - 3 dpa when swelling begins to occur perpendicular to the fiber axis. In contrast, the 2D RFC composite, which has fibers oriented perpendicular to the cylindrical axis of the specimen, exhibited minimal change perpendicular to the fiber axis up to 4.5 dpa, with about 2% shrinkage parallel to the fiber axis. The 3D PAN C/C composites displayed more isotropic dimensional changes compared to both the 1D and 2D RFC composites, shrinking uniformly in the in-plane directions (i.e. aligned with fiber tows in the wrap and weft directions) up to 2 dpa before reaching a diametrical turnaround. As shown in Figure 4.4 (right), pitch-based fiber composites are generally more dimensionally stable than the PAN fiber C/C composites, primarily due to the more graphitic nature of pitch-based fibers in comparison to PAN-based fibers [146]. However, this advantage can be offset by factors such as processing quality, fiber architecture, and

application-specific loading conditions, where PAN-based fibers may offer more uniform properties or better mechanical performance.

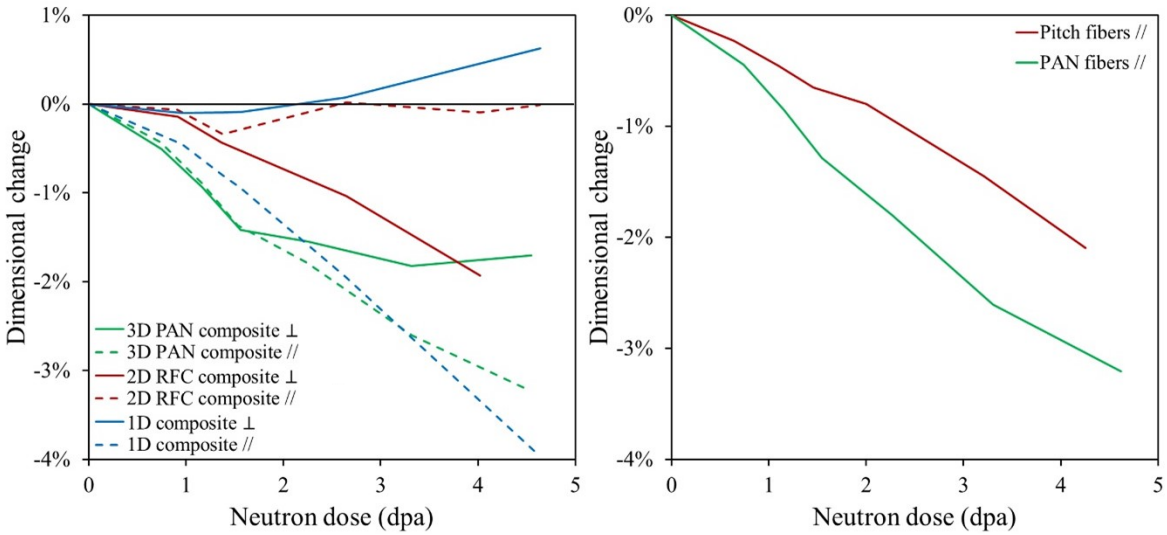


Figure 4.4. Effect of irradiation dose on the dimensional change of several PAN-fiber C-C composites irradiated at 600 °C (left) [144]. Irradiation dimensional change in two 3D, C–C Composites; Pitch and PAN fibers (right)[146].

## 4.2 SiC/SiC Composite Properties (unirradiated and irradiated)

The material properties presented in this section for SiC/SiC CMCs are made from different fabrication processes including CVI, NITE, PIP, and MI or LSI as discussed earlier. The properties of the CMC differ with respect to:

- Fiber grade, architecture, and volume fraction
- Interphase
- Precursor, additives, and binder
- Processing temperature

The material properties of SiC/SiC composites fabricated from different processes are compared in Sections 4.2.1 and 4.2.2, and the effects of radiation are also shown.

Most of the properties found in the literature were for CMCs manufactured using the CVI and NITE processes. The composite materials fabricated using CVI and NITE processes that are studied here for analyzing the effects of neutron irradiation are listed in Table 4.3. Based on the property values and the effects of neutron radiation, discussions are also provided in Sections 4.2.1 and 4.2.2.

Table 4.3: Detailed information of SiC/SiC CMCs considered in this report [24, 35, 42, 50, 147].

| Process | Material designator | Fiber | Architecture | Interphase | Density ($g/cm^3$) | Porosity | Fiber volume fraction |
|---|---|---|---|---|---|---|---|
| CVI | SA3/PyC150-A | Tyranno SA3 | Plain-weave (PW), 17 × 17 thread per inch (tpi) 0°/90° | PyC, 150 nm | 2.58 | 0.18 | 0.38 |
| | SA3/PyC50-A | Tyranno SA3 | PW, 17 × 17 tpi 0°/90° | PyC, 50 nm | 2.62 | 0.17 | 0.38 |
| | SA3T/PyC150-A | Tyranno SA3T | PW, 17 × 17 tpi 0°/90° | PyC, 150 nm | 2.50 | 0.20 | 0.37 |
| | HNLS/PyC150-A | Hi-Nicalon Type S | PW, 25 × 25 tpi 0°/90° | PyC, 150 nm | 2.40 | 0.23 | 0.46 |
| | HNLS/PyC50-A | Hi-Nicalon Type S | PW, 25 × 25 tpi 0°/90° | PyC, 50 nm | 2.31 | 0.26 | 0.46 |
| | HNLS/ML-A | Hi-Nicalon Type S | 5-Harness satin-weave (5H-SW), 16 × 16 tpi, 0°/90° | Multilayer | 2.47 | 0.24 | 0.37 |
| | HNLS/PyC150-B | Hi-Nicalon Type S | 5H-SW, 16 × 16 tpi, 0°/90° | PyC, 150 nm | 2.71 | 0.14 | 0.40 |
| NITE | SA3/PyC200 | Tyranno™ SA3 | Unidirectional | PyC, 200 nm | - | 0.05 | - |
| | SA3/PyC300 | Tyranno™ SA3 | Unidirectional | PyC, 300 nm | - | 0.05 | - |
| | SA3/PyC500 | Tyranno™ SA3 | Unidirectional | PyC, 500 nm | 2.94 | 0.20 | 0.31 |
| | SA3/PyC500 | Tyranno™ SA3 | Unidirectional | PyC, 500 nm | 2.81 | 0.23 | 0.52 |
| | SA3/PyC500 | Tyranno™ SA3 | Unidirectional | PyC, 500 nm | 2.96 | 0.26 | 0.55 |

### *4.2.1 Mechanical Properties*

To demonstrate the effects of irradiation on the mechanical properties, literature data was reviewed for the following irradiation conditions: (i) 830 ℃, 5.9 dpa, (ii) 1000 ℃, 5.3 dpa, (iii) 1270 ℃, 5.8 & 5.9 dpa. The effects of irradiation on the mechanical properties are shown in Figures 4.5 – 4.7, and then the properties are discussed for the CVI and NITE processes separately. The properties were grouped based on the type of test conducted as listed in Table 4.4.

Table 4.4: Mechanical property parameters reported in this report for tensile, flexure, and compressive tests.

| Test type | Property | Unit |
|---|---|---|
| Tensile test | Young's modulus | GPa |
| | Tensile proportional limit stress | MPa |
| | Tensile strain-to-failure | % |
| | Poisson's ratio | |
| | Tensile strength | MPa |
| Flexure test | 4-point flexure strength | MPa |
| | 4-point flexure modulus | GPa |
| | 3-point flexure strength | MPa |
| | 3-point flexure modulus | GPa |
| | Weibull modulus | |
| | Weibull characteristic strength | MPa |
| Compressive test | compressive strength | MPa |
| | compressive strain-to-failure | % |
| | fracture toughness | MPa$\sqrt{m}$ |
| | interlaminar shear strength | MPa |
| | trans-thickness tensile strength | MPa |

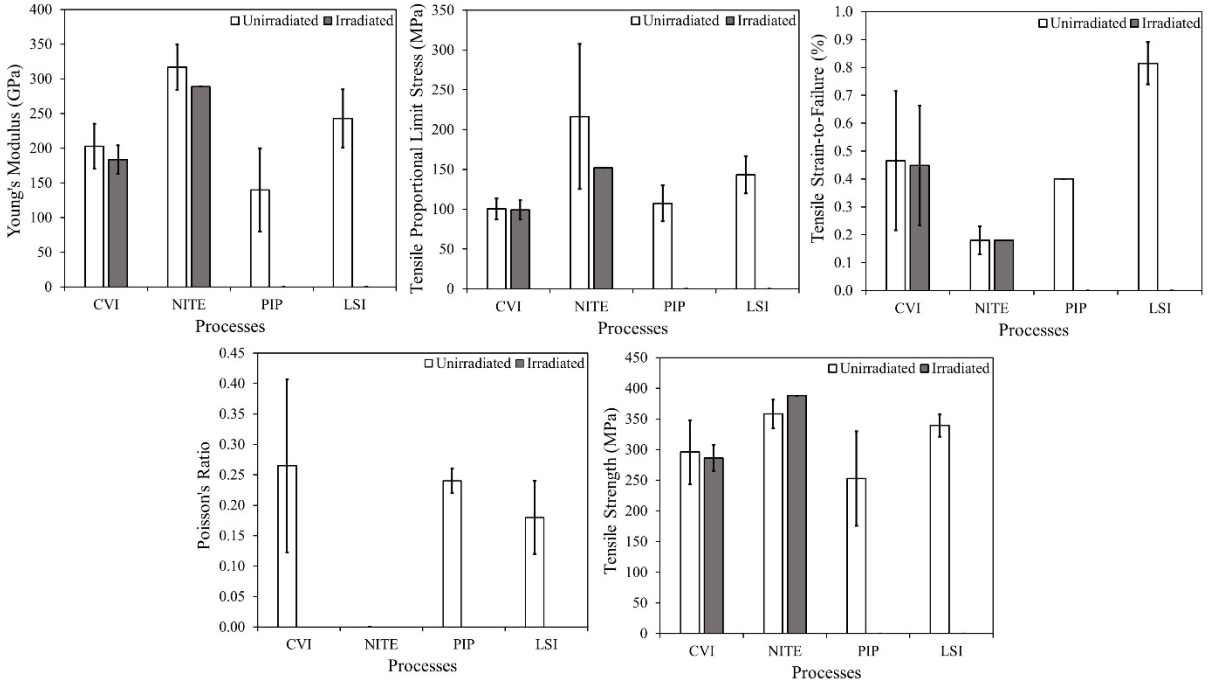


Figure 4.5. Effect of neutron irradiation on mechanical (tensile) properties extracted for SiC/SiC CMCs from literature.

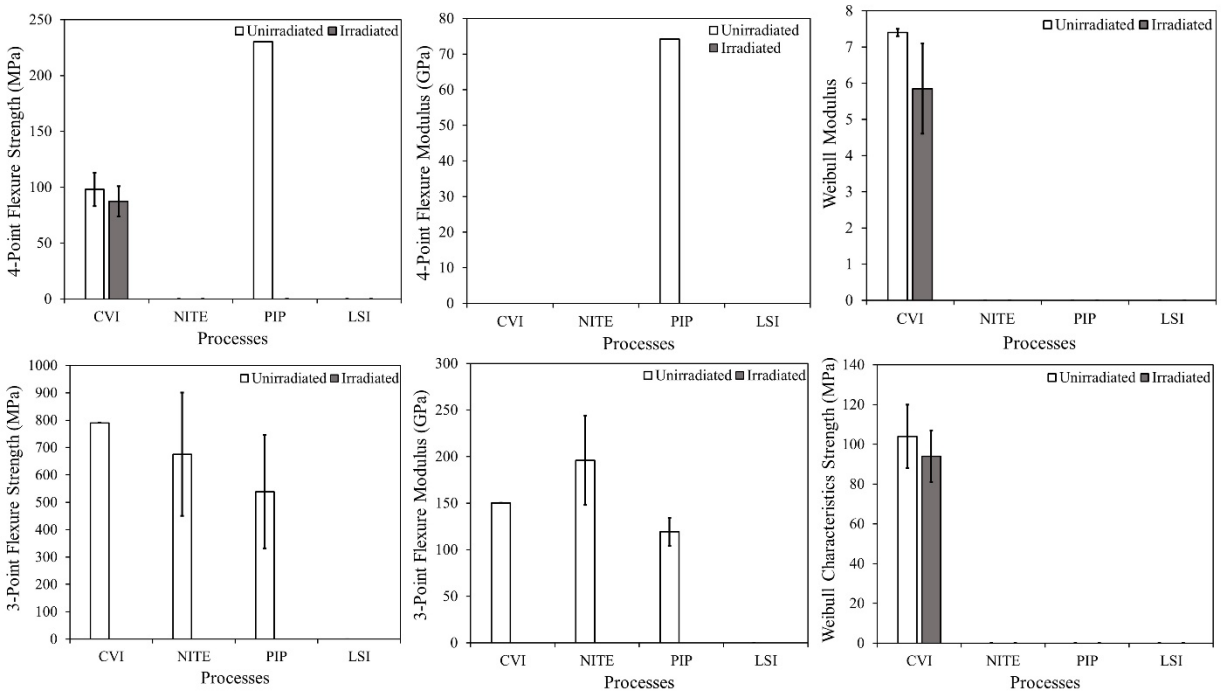


Figure 4.6. Effect of neutron irradiation on mechanical (flexure) properties extracted for SiC/SiC CMCs from literature.

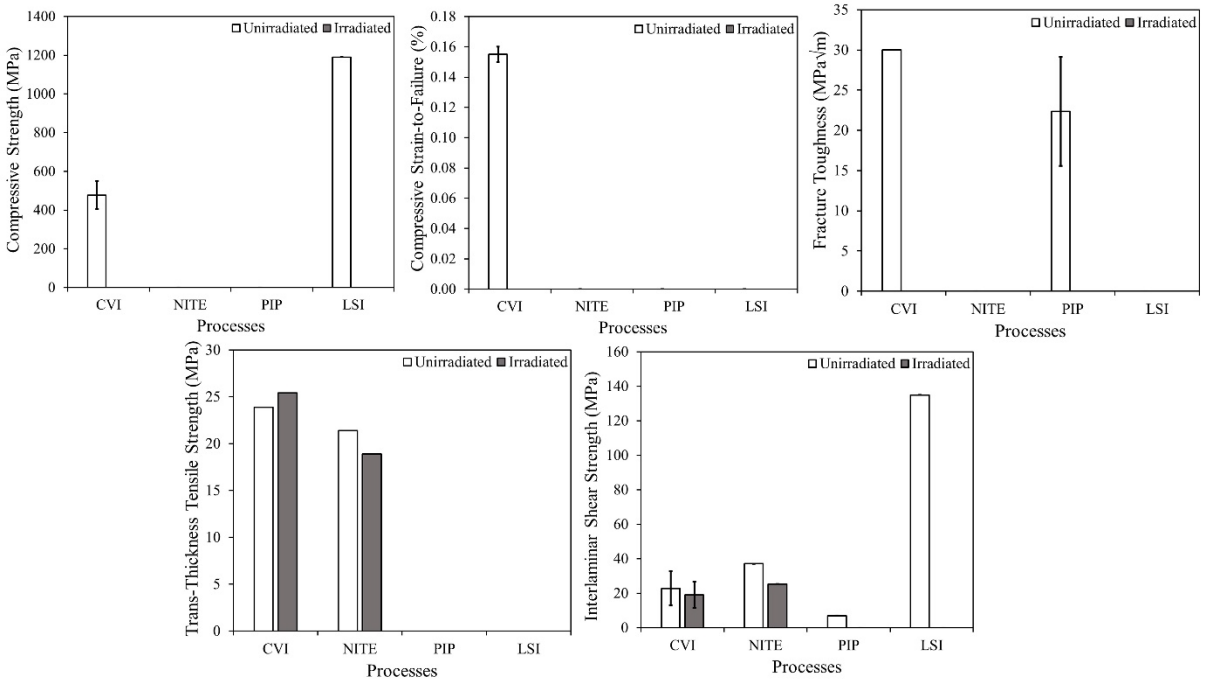


Figure 4.7. Effect of neutron irradiation on mechanical (compressive) properties extracted for SiC/SiC CMCs from literature.

From the above plots and their sources, it is observed that the:

***i. CVI process***

- The Young's modulus decreases by approximately 9% after neutron irradiation at 830 °C to a dose of 5.9 dpa. The change in Young's modulus is negatively correlated with lattice swelling, and the swelling follows a linear trend similar to monolithic beta-phase SiC, which is the primary constituent of the matrices and fibers in SiC/SiC CMCs. The trend is represented by Equation 4.1 [24]:

$$\frac{\Delta E}{E_0} = -\frac{swelling}{3} * c \tag{4.1}$$

  where $E_0$ is the initial Young's modulus, ΔE is the change in Young's modulus after irradiation, and c is a constant with a value of approximately 10. The accumulation of point defects in the composite is responsible for this trend [24].

- The changes in average PLS, ultimate tensile strength (UTS), and tensile strain-to-failure with irradiation are small. The differences between pre-irradiation and post-irradiation values for PLS and UTS in the various 2D CVI SiC/SiC CMCs, as shown in Table 4.5 under two different irradiation conditions, barely exceed one standard deviation. This suggests that neutron irradiation likely has a small effect on the tensile strength of CVI SiC/SiC composites under the tested conditions (i.e. 830 ºC to 5.9 dpa). The UTS of the composite is ideally governed by the statistical strength properties of the fibers alone [24]. The insensitivity of UTS to irradiation suggests that irradiation does not have a significant impact on the in-situ strength of either Tyranno SA3 or Hi-Nicalon Type S fibers. Additionally, no significant or detrimental effects of irradiation on the tensile load–displacement curves have been noted or reported [151].

- The average flexure strength is not strongly affected by irradiation as shown in Figure 4.6. However, early studies showed that composites made with non-stoichiometric SiC fibers experienced a nearly 50% reduction in flexural strength at about 5 dpa and then did not change significantly on further irradiation up to 100 dpa [152]. In contrast, for composites with advanced stoichiometric fibers like Hi-Nicalon Type S and Tyranno-SA, the strength increased at initial neutron irradiation of around 1 dpa, and no further degradation in strength occurs at doses up to 25 dpa [153]. Lastly, for high-purity CVD SiC and SiC/SiC CMCs made from CVI [149], the Weibull modulus and characteristic strength show no significant effect from irradiation.

- The Interlaminar Shear Strength (ILSS) is retained after irradiation as seen in Figure 4.7, even though the interface properties degrade. This indicates that the translaminar shear failure is mainly governed by the crack propagation through the matrix or between pores and fiber tows, not by the fiber-matrix interface [24]. On the other hand, the interfacial debond shear strength (IDSS) and interfacial friction stress (IFS) initially decrease with neutron irradiation and then saturate with further irradiation as shown in Figures 4.7 and 4.8. At higher temperatures (~1100 ℃) the reduction is larger. The reduction in IDSS and IFS may be because of interlaminar porosity where the strength is inversely related to the number of interlaminar pores for 1D fiber architecture.

Table 4.5: Effects of neutron irradiation on tensile PLS and UTS of various 2D CVI SiC/SiC composites [24].

| | SA3/PyC 150-A | SA3/PyC 50-A | SA3T/PyC 150-A | HNLS/PyC 150-A | HNLS/PyC50-A | HNLS/ML-A | HNLS/PyC 150-B |
|---|---|---|---|---|---|---|---|
| PLS (MPa) | | | | | | | |
| Unirradiated | 119 ± 20 | 105 ± 9 | 100 ± 17 | 79 ± 21 | 85 ± 8 | 107 ± 15 | 110 ± 15 |
| 830 °C, 5.9 dpa | 106 ± 15 | 101 | 109 ± 17 | 77 ± 18 | 85 ± 8 | 103 ± 18 | 113 ± 15 |
| 1270 °C, 5.8 dpa | 96 ± 18 | 122 ± 21 | | 79 ± 15 | 70 ± 18 | 100 ± 18 | 104 ± 12 |
| UTS (MPa) | | | | | | | |
| Unirradiated | 278 ± 22 | 287 ± 16 | 318 ± 33 | 343 ± 4 | 306 ± 15 | 230 ± 22 | 378 ± 51 |
| 830 °C, 5.9 dpa | 304 ± 38 | 269 | 273 ± 38 | 309 ± 14 | 306 ± 15 | 249 ± 28 | 295 ± 36 |
| 1270 C, 5.8 dpa | 274 ± 28 | 279 ± 7 | | 290 ± 17 | 300 ± 13 | 234 ± 21 | 339 ± 40 |

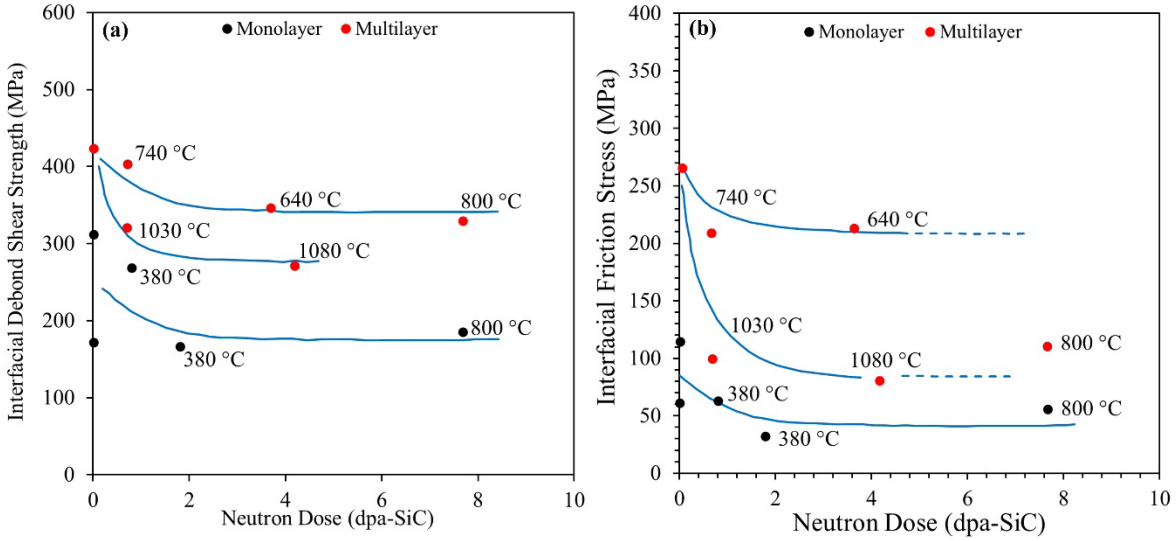


Figure 4.8. Neutron irradiation effects on (a) the IDSS and (b) the IFS. Note that the numbers embedded in the figures show the irradiation temperatures. Data points were taken from [24].

### *ii. NITE process*

- As seen in Figure 4.5, the Young's modulus showed a statistically insignificant decrease of 8% after neutron irradiation at a temperature 830 ℃ to 5.9 dpa [147]. The composites,

although made using the NITE process, used the same type of fiber (Tyranno-SA3) as used in CVI process.

- The PLS of NITE-SiC/SiC CMCs decreased following irradiation at 830 °C to 5.9 dpa as shown in Figure 4.5. However, note that PLS data for unirradiated condition for NITE in Figure 4.5 represent multiple experiments with considerable variation, revealing a standard deviation of ± 91 MPa, while the irradiation condition includes only one data point. The lack of data for irradiated conditions makes it difficult to draw definitive conclusions about the effect of irradiation on PLS of NITE. Furthermore, T. Koyanagi et al. [154] reported an increase in tensile PLS of NITE upon irradiation, as listed in Table 4.6. This increase in PLS of NITE upon irradiation can be due to a reduction in tensile misfit stress ($\sigma_T$ as shown in Table 4.6), which is also the tensile residual stress in the matrix along the fiber axial direction. The equation for PLS can be expressed as:

$$\sigma_{PLS} = \sigma - \sigma_T \quad where\, \sigma = f(\tau, E_f, E_m) \tag{4.2}$$

where $\tau$: frictional stress at the fiber/matrix interface, $E_f$: Young's modulus of fiber, $E_m$: Young's modulus of matrix.

The possible reasons for the reduction in tensile misfit stress can be irradiation creep, secondary stress effects caused by greater swelling of the matrix compared to fiber, and the degradation of CTE. Increase in the frictional stress at the fiber/matrix interface ($\tau$) could also contribute to increasing the PLS. The possible reasons for an increase in friction stress can be an increased friction coefficient caused by grain growth in the fibers and matrix, or an increase in local stress due to larger swelling of the oxide phases around the fibers compared to swelling of the fibers and matrix. Previous evaluation of the irradiation-induced swelling of a monolithic SiC indicated larger swelling of Y-Al oxide as a secondary phase in monolithic NITE-SiC [154]. The larger swelling of the oxide phases is also indicated by neutron irradiation experiment [155]. However, additional experimental data are required to clarify the mechanism underlying the observed increase in the interfacial frictional stress caused by irradiation.

The increase in UTS found in Figure 4.5 and Table 4.6 can be explained by a decrease in the strength of interfacial bonding that promotes the deflection of the matrix crack. There is a matrix tensile residual stress (misfit stress) in the fiber axial direction due to the larger matrix CTE as compared to the fiber. The misfit stress decreased after irradiation which suggests a decrease in the compressive stress in the fiber and also a decrease in the interfacial bond strength [147].

- No data was found on the effect of irradiation on the flexure strength, characteristic strength, and Weibull Modulus of NITE-SiC/SiC CMCs. However, T. Koyanagi et al. [147] measured these properties for monolithic NITE-SiC which is commonly used as the matrix

phase of the NITE-SiC/SiC CMCs, using 3-point or 4-point bending tests and reported decrease in these values after irradiation as seen in Figure 4.9. The Weibull mean 3-point flexure strength increased 9% from 823 MPa before irradiation to 896 MPa after irradiating at 800°C to 0.77 dpa. The Weibull mean 4-point flexure strength decreased 34% from 598 MPa before irradiation to 393 MPa after irradiating at 830°C to 5.9 dpa. These results show degradation of flexural strength after high temperature and dose irradiation. The detrimental effects arose possibly from the misfit stress which induced microcracking due to the differential swelling between secondary phases (such as oxides) and SiC. The strength can also degrade if the grain boundary strength degrades due to the presence of oxide films at the SiC grain boundaries.

- As seen in Figure 4.7, the trans-thickness tensile stress didn't show degradation which can be because the matrix surrounding the fibers bore the load and fractured. While the ILSS degraded by 30% as the shear strength at fiber/matrix interface (PyC) degraded in strength with irradiation.

Table 4.6: Effects of neutron irradiation on PLS, UTS and misfit stress of NITE-SiC/SiC composites. It is noted that a positive sign denotes axial tensile residual stress in the matrix [147].

| | PLS | UTS | Misfit stress |
|---|---|---|---|
| Unirradiated | 104 ± 25 | 399 ± 20 | 120 ± 21 |
| JMTR, 600 °C, 0.52 dpa | 127 ± 23 | 377 ± 19 | 35 ± 14 |
| Unirradiated | 142 ± 26 | 344 ± 25 | 146 ± 24 |
| HFIR, 830 °C, 5.9 dpa | 152 ± 32 | 388 ± 32 | 94 ± 24 |
| HFIR, 1270 C, 5.8 dpa | 181 ± 46 | 404 ± 21 | 83 ± 13 |

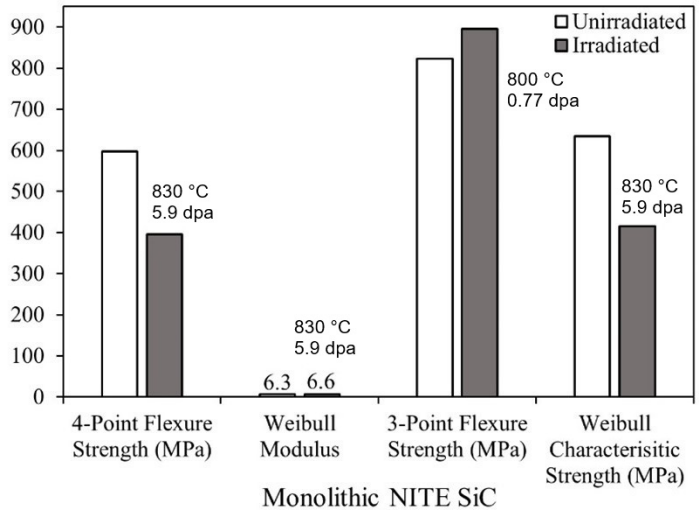


Figure 4.9. Monolithic NITE-SiC Weibull mean 3-point flexure strength before irradiation and after JMTR irradiation at 800 °C to 0.77 dpa. Monolithic NITE-SiC Weibull modulus, Weibull characteristic strength, and Weibull mean 4-point flexure strength before irradiation and after HFIR irradiation at 830 °C to 5.9 dpa. Data points from previous work were taken from Ref [147].

### *4.2.2 Thermal and Physical Properties*

The test samples were irradiated at various conditions out of which the most extreme ones were: (i) 830 ℃, 5.9 dpa, (ii) 1270 ℃, 5.8 & 5.9 dpa, (iii) 400 - 700 ℃ & 2 to 10 dpa. Post-irradiation the samples were tested as per the standards mentioned in Table 4.1, for thermal properties. The changes due to irradiation are shown for only two of the thermal properties in Figure 4.10. Effect of neutron irradiation on thermal properties extracted for SiC/SiC CMCs from literature which are the thermal expansion coefficient and thermal conductivity. The thermal conductivity was calculated using the measured thermal diffusivity, the measured specific gravity for the individual specimen, and standard specific heat.

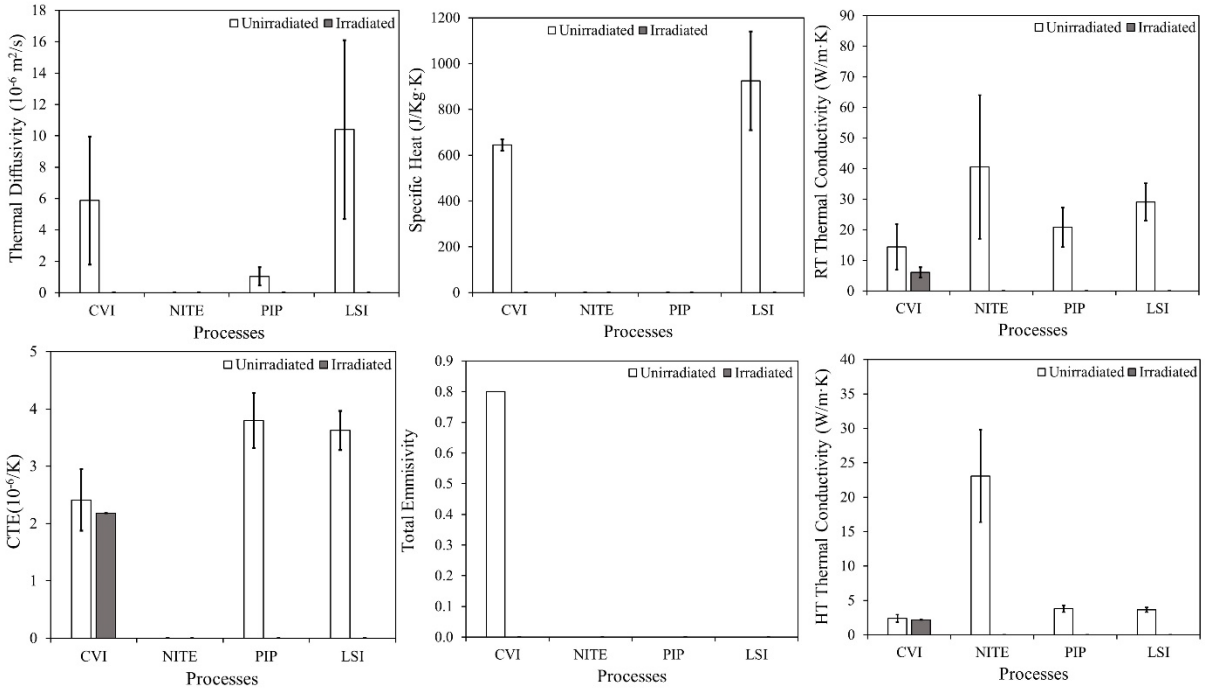


Figure 4.10. Effect of neutron irradiation on SiC/SiC CMC thermal properties extracted from the literature, including thermal diffusivity, CTE, specific heat, total emissivity, and room temperature (RT) and high temperature (HT) thermal conductivity.

From the above plots and the literature, it was observed that for the:

***i. CVI process***

- As shown in Figure 4.10, the CTE result indicated little to minor effect of irradiation on near-stoichiometric CVI SiC/SiC CMC materials. Y. Katoh et al. [24] demonstrated in their research that there was a slight and consistent decrease in the CTE of the SA3/PyC150-A 2D plain-weave composite after irradiation at 830 °C to 5.9 dpa, likely due to lattice swelling. However, no significant changes in CTE were noted for the same composite following irradiation at 1270 °C to 5.8 dpa. They also reported a minor, unexplained increase in CTE for the HNLS/ML-A 2D 5-harness satin-weave composite after irradiation at 1270 °C to 5.8 dpa, which was considered insignificant [24].

- The thermal conductivity significantly decreases as seen in Figure 4.10. The trends with fluence and irradiation temperature are similar to those of swelling. Thermal conductivity saturation occurs early, typically before a few dpa, and remains stable up to high fluence levels (>70 dpa at 800°C) as seen in Figure 4.11. The effect of irradiation can be modeled by the relation:

$$K_{irr}^{-1} = K_0^{-1} + K_{rd}^{-1} \quad (4.4)$$

where $K_{irr}^{-1}$ and $K_0^{-1}$ denote irradiated and unirradiated thermal resistivity, respectively, and $K_{rd}^{-1}$ is the radiation-defect thermal resistivity that represents collective contributions from various radiation-produced defects to the volume thermal resistivity. The thermal conductivity of ceramic materials such as SiC/SiC is based on phonon transport. The reason for a decrease in conductivity at low temperatures is due to the scattering of phonons arising from point defects and defect clusters generated by neutron irradiation. This affects the phonon transport and reduces thermal conductivity. Phonons are essentially vibrations in a crystal lattice that transport heat. For high-purity CVD SiC, the number density and therefore the thermal resistivity of defects (from irradiation) is directly proportional to the macroscopic swelling in the material [156]. Essentially these same defects that are responsible for increased thermal resistivity by scattering phonons are the ones that contribute to the observed macroscopic swelling as shown in Figure 4.11[157]. At high temperatures, the defects are more mobile and recombined. This decreases their concentration and hence, a lesser reduction in conductivity is observed as seen in Figure 4.10.

### *ii. NITE process*

- No data was found on the effect of irradiation on the thermal properties of NITE-SiC/SiC CMCs. However, a previous study showed that thermal conductivity of NITE-SiC degrades with dpa (similar to CVI CMC) and degradation saturates at or before 2 dpa as shown in Figure 4.12. The NITE variant with the largest grains and lowest porosity shows the highest conductivity prior to and after irradiation. Scattering of phonons and defects created from irradiation are concluded to be the main sources of resistance to thermal transport processes, which decrease the thermal conductivity. The decreasing trend is similar to CVI CMCs but with higher parameters indicating higher contribution of defects to resistivity as seen in Figure 4.12.

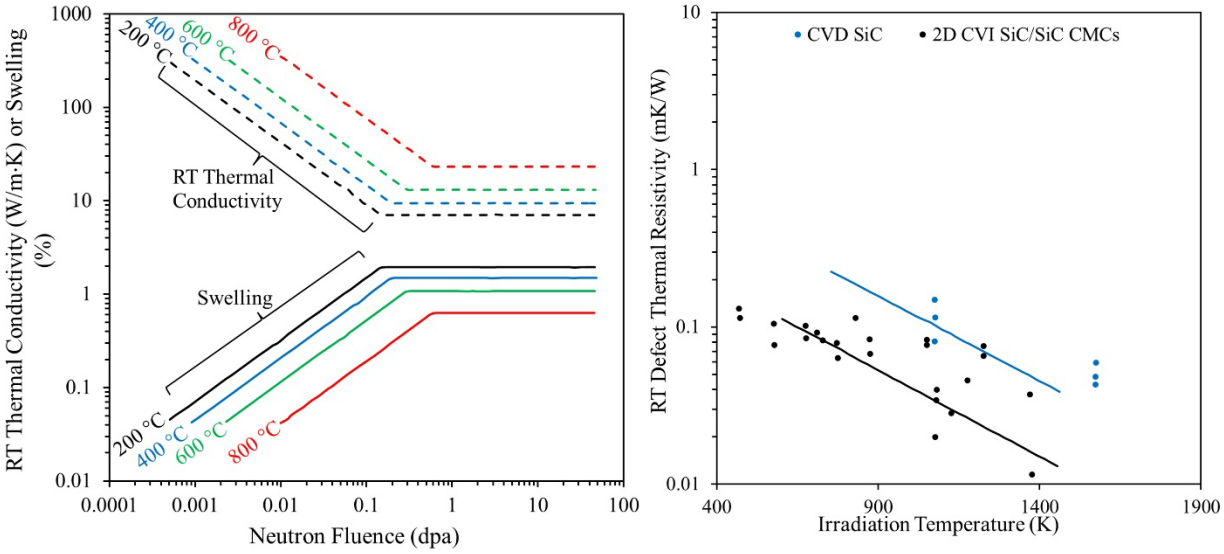


Figure 4.11. Fluence-dependent evolutions of swelling and thermal conductivity of CVD SiC. Data (left) [157]. Radiation-defect thermal resistivity at room temperature for neutron- irradiated 2D SiC/SiC composites plotted against irradiation temperature (right) [24].

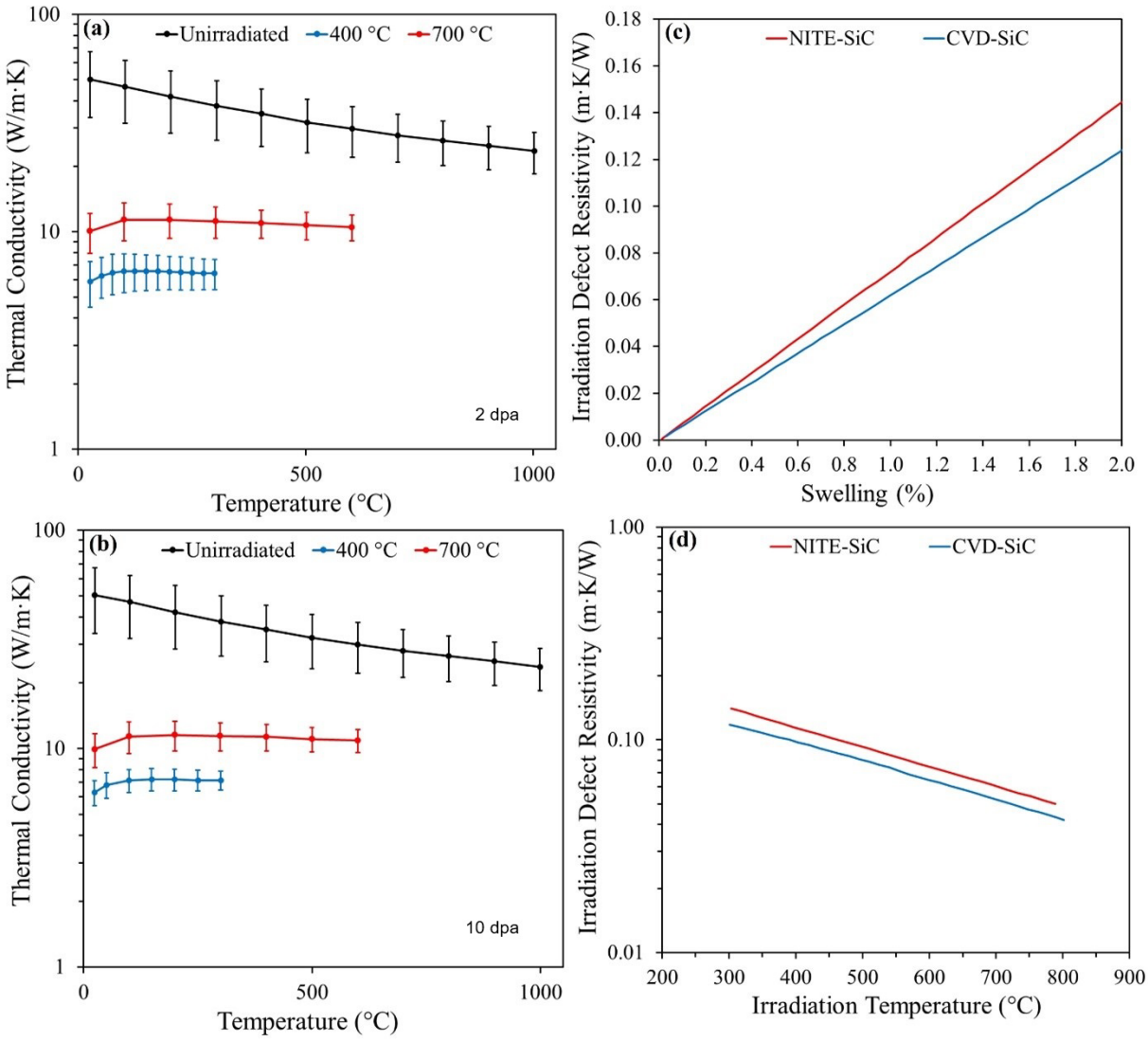


Figure 4.12. Thermal conductivity of the NITE-SiC variants before and after irradiation at: (a) 2 and (b) 10 dpa. Irradiation defect (thermal) resistivity for CVD and NITE-SiC as a function of (c) swelling and (d) irradiation temperature [156].

## 4.3 Summary of CMC Material Properties

This report provides a summary compilation of properties for C/C and SiC/SiC CMCs before and after neutron irradiation. Below is a summary of the key points identified in the report for these CMCs.

- C/C CMCs: The report finds the mechanical properties of C/C CMCs initially improve upon irradiation but can degrade at higher doses. However, thermal conductivity significantly degrades with irradiation. C/C CMCs can exhibit anisotropic property changes due to their structure, including dimensional changes which can shrink or swell with specimen orientation, dose, and irradiation temperature. The composite structure may lead to additional degradation mechanisms than for graphite alone.

- SiC/SiC CMCs: The comparison between unirradiated and neutron-irradiated CVI SiC/SiC CMCs shows neutron irradiation has a minimal impact on most mechanical properties. Young's modulus decreases slightly by about 9%, while Poisson's ratio, PLS, and UTS remain largely unaffected. In contrast, thermal properties exhibit more noticeable changes. The CTE shows minor shifts, with a slight decrease at room temperature and a slight increase at higher temperatures after irradiation. Thermal conductivity, however, drops significantly, from 8.5 - 50.3 W/m·K to 1.2 - 11.7 W/m·K at room temperature. Additionally, translaminar shear strength and trans-thickness tensile strength show no significant irradiation effects.

  For NITE-SiC/SiC CMCs, neutron irradiation results in a minor decrease of about 8% in Young's modulus, while Poisson's ratio remains unchanged. Interestingly, both PLS and UTS increase, suggesting improved load-bearing capacity. However, flexure strength degrades, indicating reduced resistance to bending forces. Translaminar shear strength is largely unaffected, but trans-thickness tensile strength drops by 30%, reflecting a notable decline in through-thickness integrity. Additionally, thermal conductivity in NITE-SiC/SiC CMCs is significantly reduced at both room and high temperatures. Overall, neutron irradiation has mixed effects, enhancing some mechanical properties while degrading others, particularly thermal conductivity and through-thickness strength.

# 5 Oxidation and Corrosion of CMCs

This chapter presents an understanding of the current state of knowledge of C/C and SiC/SiC CMCs regarding their life-limiting mechanisms in oxidative and corrosive environments.

## 5.1 Oxidation

### *5.1.1 C/C Composites*

C/C CMCs were initially designed for rocket nozzles and re-entry shielding and, as such, there is technical experience concerning their general oxidation at high temperatures in atmospheric conditions [20]. The high-temperature (i.e. > 450 ℃) applications of C/C composites are limited due to their poor oxidation resistance at those temperature ranges. These composites are known to oxidize according to the following reactions that form gaseous products,

$$C\ (s) + O_2(g) \rightarrow CO_2(g) \tag{5.1}$$

$$2C\ (s) + O_2(g) \rightarrow 2CO(g) \tag{5.2}$$

The Arrhenius plots in Figure 5.1, taken from [8], show the oxidation mechanisms (or burn-off rate) are temperature dependent:

- At T < ~800 ℃ the burn-off rate is controlled by the intrinsic oxidation chemical reaction rate (chemical kinetics).
- At T > ~800 ℃ the burn-off rate is limited by diffusion (mass transport).

The oxidation attack starts on the atoms at the edge of the carbon material, which means crystal defects in the carbon structure [135]. Therefore, the carbon matrix is more prone to oxidation than the reinforcing C-fibers [8]. Oxidation / burn-off rates at low temperatures can be reduced by increased crystallinity and purification of the carbon matrix by higher final high-temperature treatment as shown in Figure 5.1.

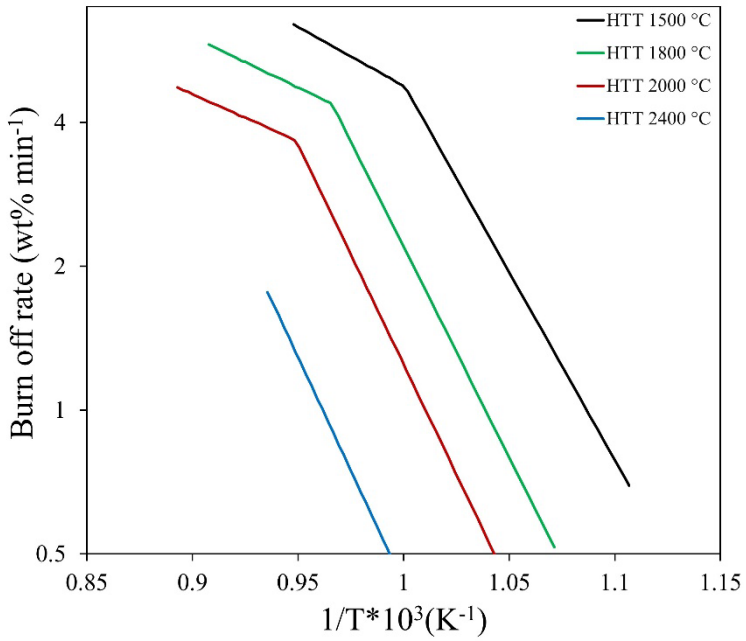


Figure 5.1. Arrhenius model plots of the oxidation of C/C composites from literature [8].

Several studies have shown that the burn-off of C/C Composites is similar to that of graphite at different temperatures in air or steam [1]. To facilitate understanding of the oxidation of C/C composites, the ASME BPVC 2023 code explains briefly the mechanisms of oxidation of graphite and what can be expected post oxidation. During oxidation of graphite from the above plots and the literature, it was observed that:

- Gasification of hot graphite can occur when exposed to oxygen, steam or carbon dioxide.
- The gasification from oxidation of graphite can occur through two mechanisms:
  - Acute oxidation: which can happen when exposed to air or water in the event of a potential air or steam ingress accident scenario. This mechanism is fast and can lead to surface corrosion, weight, loss and density reduction followed by dimensional changes.
  - Chronic oxidation: which usually happens from exposure to small concentrations of coolant impurities and is a slow process. It affects the surface region.
- Depending on conditions (temperature, oxidant concentration, duration) and graphite properties, the thickness of the oxidized layer on the surface may vary. The oxidized layer is a degraded zone where graphite has been chemically attacked and partially or fully removed, often forming a visibly rougher, porous, or eroded surface. At higher temperatures, oxidation occurs more quickly and uniformly across the surface, often consuming the exposed material entirely, resulting in a thinner oxidized layer. In contrast, at lower temperatures,

the reaction is slower and more localized, allowing the oxidized region to penetrate deeper over time.

- The weight loss can cause gradients in the material or component leading to a gradient in the strength in the oxidized layer near the surface [158]. Figure 5.2 shows the dependence of strength of a particular isotropic graphite grade on weight loss after uniform oxidation.

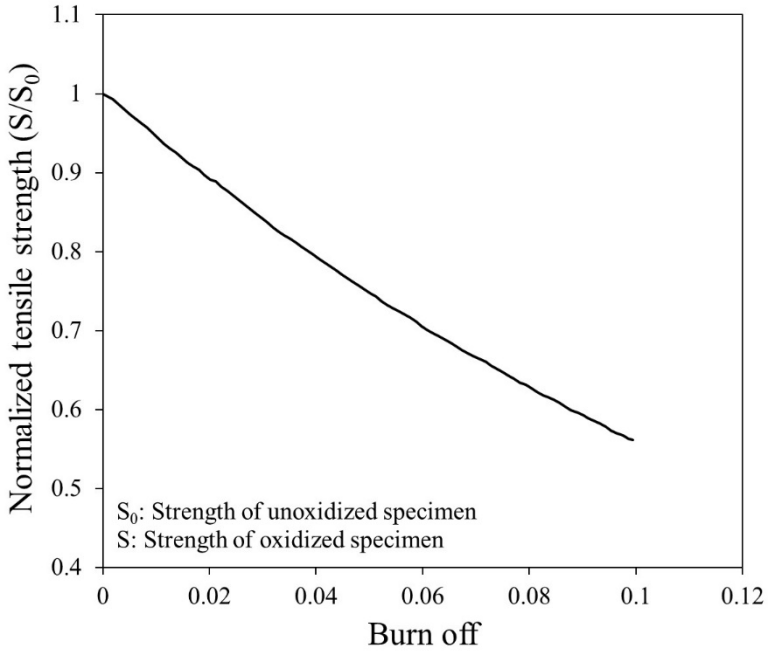


Figure 5.2. Loss in normalized tensile strength of isotropic graphite IG-110 due to a burn-off (i.e. weight loss) occurring from oxidation [158].

The mechanical and thermal properties of C/C CMCs are significantly affected by long-term oxidation, particularly in high-temperature reactor environments. The oxidation behavior of C/C CMCs in air has been studied to evaluate the impact of a potential air ingress incident during depressurization in VHTRs, for ensuring reactor safety and material performance [140]. It was reported that 2D woven C/C composite (CX-270G) experienced severe mechanical degradation after oxidation at 550 °C in air, where only 35% of its original bending strength (⊥ to fiber axis) and 40% of its tensile strength (|| to fiber axis) were retained following a 10% weight loss. These strength retention percentages are lower than those reported for conventional nuclear graphite block (grade IG-110) [140]. This reduction in strength is attributed to the oxidation of the matrix and the crack propagation at the fibers–matrix interface [159]. In addition to mechanical degradation, oxidation also impacts the thermal properties of C/C composites. A clear relationship has been established between burn-off and thermal conductivity as well as CTE for the CX-270G composite, as illustrated in Figure 5.3 [160]. Thermal conductivity decreases significantly with increasing burn-off, particularly along the fiber direction. This is due to increased phonon scattering caused by the formation of pores and cracks, which becomes more pronounced with higher levels

of oxidation. In contrast, conductivity in the direction perpendicular to the fibers is less affected, as phonon transport is already limited by interlayer voids, and Umklapp scattering remains relatively minor even at elevated temperatures [160]. Similarly, the CTE of CX-270G in both directions decreases with increasing burn-off, a result of enlarged interlayer voids, transverse crack growth, and the formation of new defects that accommodate thermal strain [160]. While these results provide valuable insights, further research is needed to fully understand the oxidation behavior of C/C composites, especially considering that variations in fiber architecture, matrix composition, and processing parameters can lead to widely differing oxidation responses and mass loss rates.

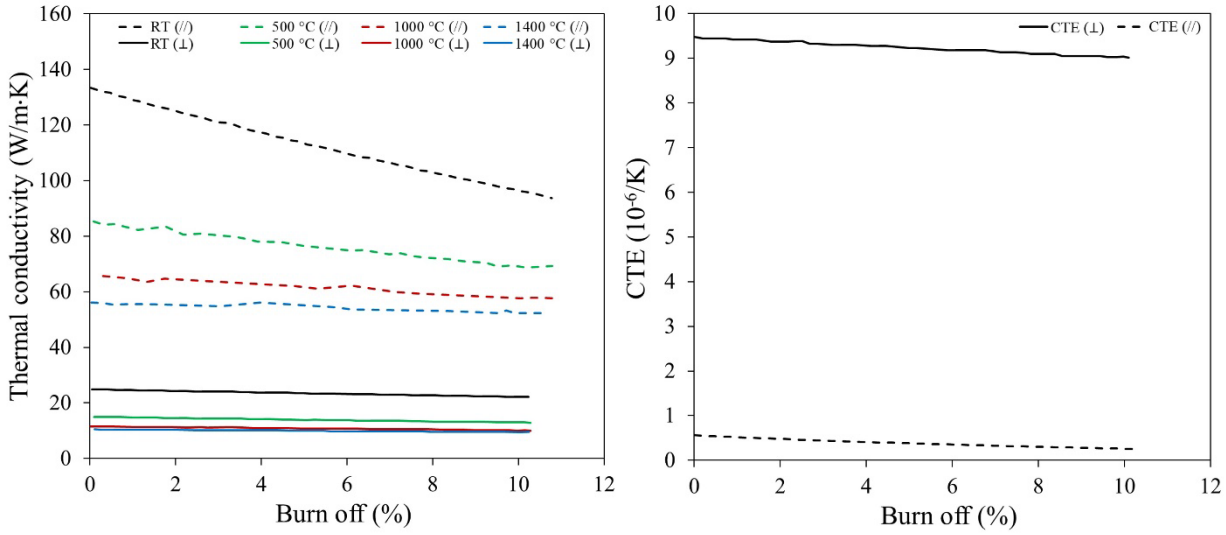


Figure 5.3. Thermal conductivity (left) and CTE (right) of CX-270G as a function of burn-off in both perpendicular and parallel to fiber axis directions after oxidizing at 500 - 550 °C [160].

To protect the C/C CMC from oxidation during operation, three systems can be put into place [8, 161]. These include:

- An inner bulk protection: enhances oxidation resistance by increasing crystallinity, using salt impregnations, or forming protective SiC layers through various silicon treatments.
- An outer multilayer CVD coating: prevents oxidation by creating a barrier using pure β-SiC or multilayer of SiC/$B_4C$/SiC.
- A glass sealing using mullite or alumina: prevents oxidation by creating a barrier using a surface coating.

### *5.1.2 SiC/SiC Composites*

To understand the mechanisms of oxidation in SiC/SiC CMCs it's necessary to first understand the oxidation of monolithic SiC which is similar in oxidation resistance to the matrix of the CMCs formed by the NITE and CVD processes.

The high-temperature oxidation of monolithic SiC occurs in either an 'active' or 'passive' mode, depending on the oxygen concentration [162].

- Active oxidation occurs at oxygen pressure less than one bar according to the following Equation 5.3,

$$SiC\ (s) + O_2(g) \rightarrow SiO(g) + CO(g) \tag{5.3}$$

In this process, volatile SiO forms leading to loss of mass.

- Passive oxidation occurs at higher oxygen pressures (≈1 bar) and follows the reaction,

$$2\ SiC\ (s) + 3\ O_2(g) \rightarrow 2\ SiO_2(s) + 2\ CO(g) \tag{5.4}$$

Here, a solid silica ($SiO_2$) layer forms, which protects the material by limiting further oxidation.

The monolithic SiC shows good oxidation resistance in comparison to Zircaloy-4 (used as light-water reactor fuel cladding material) [163]. Studies by Takaaki et al. have shown that the SiC ceramic undergoes minimal thickness loss under steam oxidation, unlike Zircaloy-4. This is because of the formation of silica (which shows a parabolic trend) and the low propensity for volatilization of silica. This silica layer formation follows a parabolic rate law—meaning the rate of oxidation decreases over time as the oxide layer thickness increases. The dense, stable silica layer acts as a diffusion barrier, limiting the transport of oxygen to the SiC surface and slowing further oxidation. Additionally, the diffusion of oxygen in the silica layer is very low compared to other oxides and this diminishes the underlying SiC oxidation.

Similar to monolithic SiC, the oxidation mechanism in SiC/SiC CMCs primarily involves silica formation, which slows down oxidation due to low diffusion coefficient of oxygen into the silica layer and limits material degradation over time. However, the oxidation behavior and resulting mechanical degradation depend on temperature, aging time, and interphase layer thickness between fibers and matrix [164]. As demonstrated in [164], at 800 °C the rate of silica formation is very low and the oxidation of the carbon interphase on the fiber is mostly observed as open channels that form between fibers and matrix. This leads to a significant drop in strength (Figure 5.4a) which was observed on testing the CMCs after aging them. At lower temperatures, the $SiO_2$ layer does not close porosity fast enough to protect the PyC layer [165]. Whereas at 1400 °C, passive oxidation of the SiC fibers resulted in the formation of silica which closed the open channels between the fibers and induced some damage resistance. The damage resistance is reflected from the relatively low drop in strength (the blue dashed line in Figure 5.4b) for material with thinner carbon interphase.

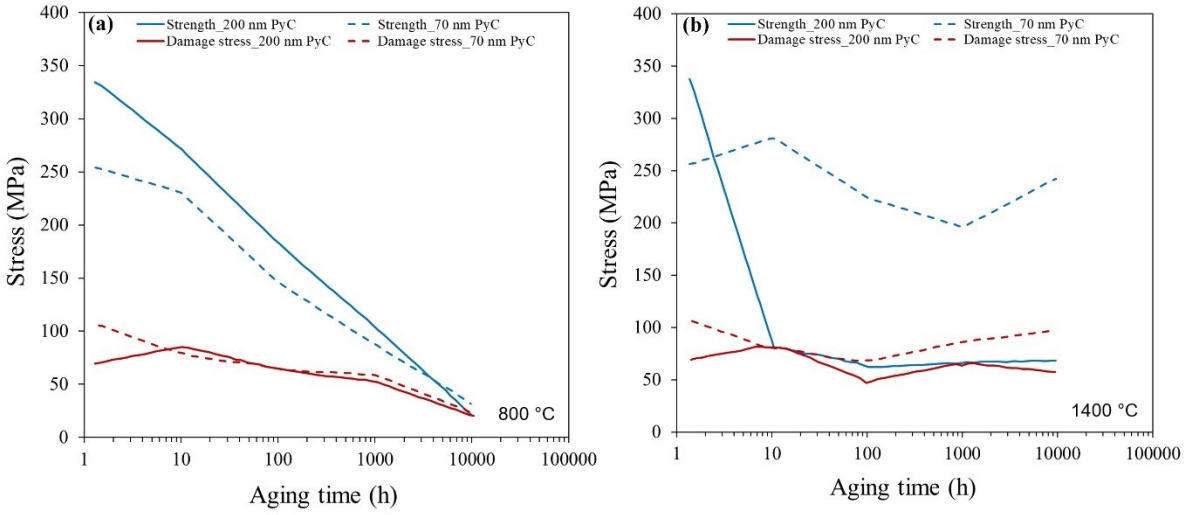


Figure 5.4. Change in fracture strength (blue lines) and damage stress (red lines) as a function of aging time for SiC/SiC composites with two different PyC interphase thicknesses (200 nm and 70 nm) at (a) 800 °C and (b) 1400 °C [164]. The solid lines represent the 200 nm PyC samples, while the dashed lines correspond to 70 nm PyC.

A similar degradation in strength and modulus was observed by another study [166] wherein a multilayer SiC/SiC CMC (made using PIP process) was subjected to oxidation and then displayed strength variations based on oxidation temperature. As shown in Figure 5.5, flexural strength was degraded by 46 % (max.) and the flexural modulus degraded by 60 % (max.) when oxidized at 700 °C for 400 h. When oxidized at 900 °C and 1100 °C (also for 400 h) the strength was observed to be retained. It was concluded that at low temperatures the PyC interphase is greatly consumed, leaving pores and hence a weakened interphase. At high temperatures (≥ 900 °C) the silica layer (from oxidation of SiC) seals the pores and prevents further oxidation.

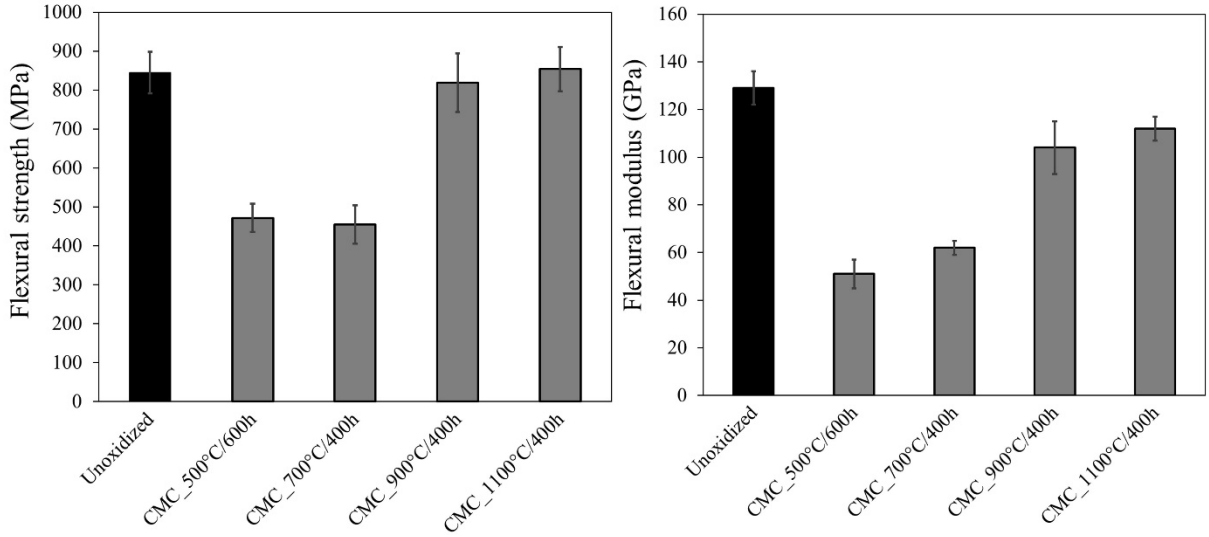


Figure 5.5. Flexure properties of the SiC/SiC CMC before and after oxidation at several temperatures [166].

The matrix in SiC/SiC CMCs is oxidation resistant and its oxidation is not a concern at temperatures < 1250 °C if the partial pressure of $O_2$ is close to 1 Pa [24]. At these temperatures and partial pressures, passive oxidation is expected to occur. However, the fiber and interphase are the weak points as they can degrade at high temperatures. SiC fibers that contain residual free carbon or exhibit poor crystallinity are particularly susceptible to oxidation. The PyC interphase is readily oxidation-prone when exposed and its degradation can lead to crack tip propagation near the interface [167, 168]. Oxidation of this carbon-rich interlayer at the fiber/matrix boundary results in the formation of a silica ($SiO_2$) layer that strengthens the bond between the fiber and matrix. While this may seem beneficial, it suppresses critical toughening mechanisms such as crack deflection and fiber pull-out, leading to embrittlement of the composite. Additionally, the oxidation of SiC at defect sites or crack tips leads to silica formation, which causes local volumetric expansion and induces additional stress at the crack tip. These effects collectively promote subcritical crack growth that limits the fiber's life. Gauthier et al. [167] showed that at moderate temperatures (500 - 800 °C) in air that the life of SiC fibers can be substantially reduced due to the slow crack propagation of surface defects initiated by carbon consumption at grain boundaries and the stress generated from SiC oxidation. As reported in [24] and shown in Figure 5.6(a), the fiber lifetime can be approximated to follow the power law whose coefficient depends on the partial pressure of oxygen.

$$t\sigma^n = A_0 \exp\left(\frac{-Q}{RT}\right), where\ A_0 = A' p_{O_2}^m \tag{5.5}$$

where $t$: rupture time, $\sigma$: applied stress, $n$: constant, $Q$: activation energy, $R$: 8.314 J (K·mol)$^{-1}$, $T$: temperature, $A'$: constant, $p_{O_2}$: partial pressure of oxygen, $m$: reaction order.

Based on the power law, a Larson Miller Parameter (LMP) can be obtained and used to extrapolate time to failure at a specific oxidizing partial pressure [24]. As shown in Figure 5.6(b), the extrapolation is done for 2 Pa which is the pressure expected in a high-temperature gas-cooled reactor (HTGR). The extrapolation to 2 Pa should only be used below 1250°C where passive oxidation is dominant.

$$LMP = T(\log_{10}(t) + 22) \tag{4.6}$$

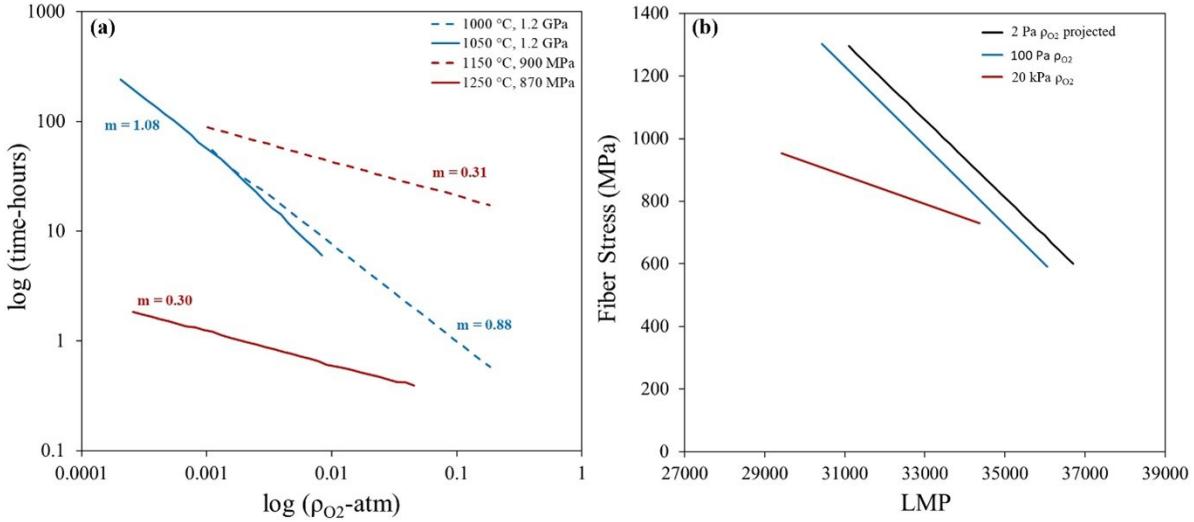


Figure 5.6. (a) Stress rupture dependence on oxygen partial pressure of Hi-Nicalon Type S/CVI SiC with a pre-cracked CVI SiC matrix showing two regimes of m = ~1 at low temperature and high stress levels and ~ 0.3 at high temperatures and low stress levels, (b) Larson Miller plot of Hi-Nicalon Type S/CVI SiC with a pre-cracked CVI SiC matrix showing effect of partial pressure of oxygen and a projection to 2 Pa [24].

According to [24], to meet the requirements for a service condition of 950 ℃ for 60 years in an HTGR, it is recommended to:

- Use a 36% fiber volume, $0^o/90^o$ Hi-Nicalon Type S/CVI SiC CMC
- Restrict maximum temperature event(s) of not more than, $T_{max} = 1250$ ℃ and maximum stress level $\sigma = 90\ MPa$ under low oxidizing partial pressure (2 Pa)
- These requirements are derived for a LMP value of 37,319

Additionally, oxidation resistance of SiC/SiC CMCs can be improved by:

- Use of well-crystallized, pure, and stoichiometric SiC fibers to avoid their oxidation.
- Multilayer matrix and interphase of PyC or a multilayer PyC/SiC of 50 – 200 nm thickness [24].
- SiC/SiC CMC made from the NITE process tends to better perform under oxidation compared to those from CVI, due to their higher density [169].

## 5.2 Corrosion

To understand the possible chemical reactions that might occur between composites and the reactor coolant and fuel systems, their chemical compatibility needs to be considered. Some examples of coolants used in nuclear reactors include:

1. Light-water reactor (LWR): $H_2O$ under high pressure [16]
2. HTGR and GFR: He gas coolant (at high temperature ~ 800 °C and high pressure ~ 5 MPa [170])
3. Fluoride salt cooled reactor (FHR): $LiF - BeF_2$ (FLiBe) as potential primary loop coolants and $LiF - NaF - KF$ (FLiNaK) as a secondary loop coolant (at high temperature ~ 400 – 600 °C but low pressure) [171]
4. Conceptual fusion reactors: $Pb - Li$ and $He/Li_2TiO_3$ coolant [172] that include self-cooled lead lithium blanket design and helium-cooled ceramic breeding blanket.

***Coolants that can affect the composites:***

1. $H_2O$ at high temperatures ($> \sim 900°C$) can oxidize C/C composites – oxidation rate and weight loss depend on the kinetics [173]. In an inert atmosphere the reaction is:

$$C_s + H_2O \leftrightarrow CO + H_2 \tag{5.6}$$

The kinetics are described using the following equations:

$$j = \frac{dm}{dt}.\frac{1}{S_{eff}} \text{ where } j = kP^n \text{ and } k = Aexp\left(-\frac{E_a}{RT}\right) \tag{5.7}$$

where $S_{eff}$ is the projected area of the active reaction surface, $j$ is the oxidation rate, $\frac{dm}{dt}$ is the instantaneous mass loss, $n$ is the pressure exponent for oxidation, $A$ is the pre-exponential factor, $E_a$ is the activation energy, $T$ is the temperature, and $k$ is the temperature dependent reaction rate constant. The reaction rate constant at different temperatures was estimated by fixing the gas temperature at an appropriate rate and maintaining a constant water vapor partial pressure and reaction surface area for the oxidizing gas [173]. Qin et al. [173] reported that for the C/C composites, oxidation occurred simultaneously at the fiber bundle and matrix, however, the oxidation rate of the fiber bundle was greater than the oxidation rate of the matrix and the composite surface became rough due to formation of small pits and cracks in the oxidation test.

When the SiC/SiC composites are exposed to high-temperature water vapor ($H_2O$) and oxygen ($O_2$) environment, the composite can undergo corrosion in two competing steps [174]:

i. At high oxygen pressures and for temperatures below 1300 °C, the SiC matrix can undergo passive oxidation to generate $SiO_2$ resulting in mass gain of composites (Figure 5.7a) according to the reaction below,

$$SiC(s) + \frac{3}{2}O_2(g) \rightarrow SiO_2(s) + CO(g) \tag{5.8}$$

ii. Reaction of water vapor with $SiO_2$ can lead to volatilization of the $SiO_2$ in the form of gaseous $Si(OH)_4(g)$ which results in mass loss. This is a form of corrosion by water vapor and the $SiO_2$ volatilization leaves annular pores around the fiber, with the fibers also severely corroded. The dense $SiO_2$ becomes loose and porous due to generation of new gas exchange channels and reaction surfaces.

$$SiO_2(s) + 2H_2O(g) \rightarrow Si(OH)_4(g) \tag{5.9}$$

As shown in Figure 5.7(b), the flexural strength of the composites decreases considerably with an increase of corrosion time. The retention rates of flexural strength are 59.7% and 15.1% respectively after 20 h and 60 h corrosion. Similar degradation behavior of flexural modulus of SiC/SiC composites can be found. This implies that the SiC fibers are damaged and directly exposed to outer corrosive environments owing to the rupture of the $SiO_2$ layer, resulting in the rapid degradation of composites.

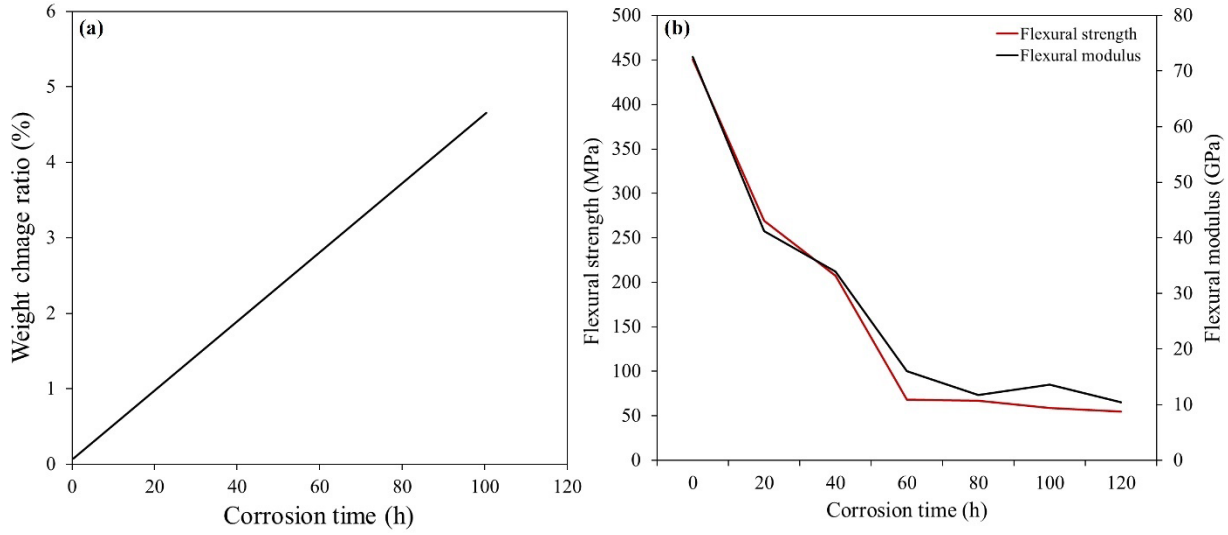


Figure 5.7. (a) The plot of mass gain as a function of time, (b) flexural strength and modulus changes with time in the mixed water vapor and oxygen corrosion environment at 1300 ℃ [174].

2. He gas (at approx. 800 $°C$ and 5 MPa [170]) is used as a coolant in HTGRs and GFRs. He gas is inert and eliminates the concern for chemical compatibility [93], but the coolant needs to be free of impurities like $O_2$ and $H_2O$ to avoid reactions with SiC/SiC and C/C [165,175]. Under a high pressure difference (~ 50 torr) [176], using He can have hermiticity issues with SiC-SiC composites and therefore surface treatments or coatings such as RP-CrN, TM-TiN, and TM-CrN are required to ensure hermeticity, particularly for applications involving irradiation or vacuum environments.

3. Recent studies have shown that molten fluoride salt (FLiNaK) exposure can, under certain conditions, enhance rather than degrade the performance of C/C composites [177, 178]. The inherent presence of pores, defects and their interfaces in PAN-based C-fiber / pitch C-matrix composites facilitates the penetration of the molten salts into the bulk of these composites. This infiltration significantly influences the composite's microstructure and mechanical behavior. Feng et al. utilized in-situ synchrotron-based X-ray diffraction (XRD) to investigate the microstructural evolution of PAN-based C-fiber / pitch C-matrix composites impregnated with FLiNaK for 20 hours, under both thermal cycling and tensile loading conditions for both thermal cycling and tensile loading [177, 178]. Their results demonstrated that FLiNaK infiltration modifies the graphite microstructure by reducing thermal expansion along the out-of-plane (OOP) direction, increasing crystallite size, and relieving internal stress [177]. Specifically, the average crystallographic thermal expansion coefficient of interlayer spacing was reduced to $(1.54 \pm 0.02) \times 10^{-5}\ K^{-1}$ in salt-impregnated composites compared to $(1.94 \pm 0.02) \times 10^{-5} K^{-1}$ in untreated samples, indicating a constraining effect of the salt on interlayer spacing [177]. Upon cooling, the crystallite size of the C/C composite impregnated with FLiNaK salt increased to approximately 32.81 nm, compared to 28.81 nm in the untreated composite, indicating the synthetic action of the salt squeeze effect on crooked carbon layers into flat layers leading to an increase in crystallite size and the release of internal residual stress. Further analysis using grazing-incidence synchrotron XRD showed the azimuthal intensity distribution of the (002) graphite diffraction ring exhibited broader and less distinct peaks in salt-treated composites, compared to the sharp peaks in untreated ones, indicating a loss of preferred in-plane orientation and more random crystallographic alignment, even after cooling. The results suggest that FLiNaK salt impregnating into C/C composite could result in the change of graphite crystallite distribution in C/C composite and weaken the texture.

   Upon tensile loading, the salt-impregnated C/C composites exhibited enhanced crystalline stability and microstructural relaxation, which translated into significantly increased fracture resistance, withstanding up to 250 N of tensile force compared to 150 N in untreated samples as shown in Figure 5.8 [178]. This improvement is attributed to the synthetic effect of the salt squeeze and applied load force. Despite this initial improvement, the graphite texture becomes increasingly disordered under higher stress, driven by the reorientation of crystal domains caused by an imbalance between salt squeeze and tensile load – ultimately leading to material failure [178]. In contrast, untreated composites exhibited failure driven by simultaneous shrinkage along both in-plane and OOP directions, while their texture remained relatively unchanged throughout loading [178]. Elemental analysis confirmed the presence of fluorine (F), potassium (K), and sodium (Na) within the carbon fibers, suggesting that molten salt penetrates deep into the fiber structure, leading to localized reinforcement and changes in fracture modes. As a result, the elastic modulus of pitch-based fibers increased from 18.3 GPa to 21.5 GPa, and the matrix modulus rose from 8.2 GPa to 10.15 GPa, with similar enhancements observed in hardness particularly in the matrix phase [178]. The improvement

in mechanical properties is attributed by study's authors to the transformation of the carbon microstructure toward a more ordered and highly crystalline graphite configuration induced by salt treatment [178].

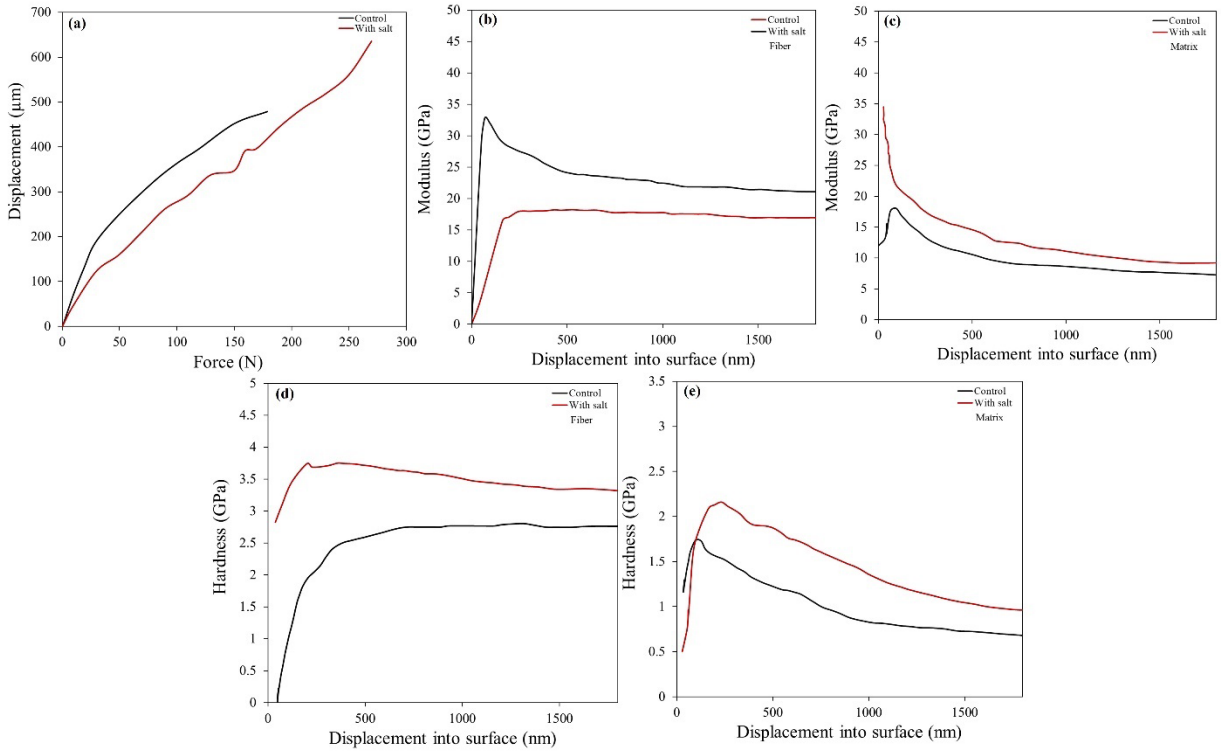


Figure 5.8. (a) The relationship between axial displacement of C/C composite and the applied tensile force, (b, c) modulus, and (d, e) hardness-indentation depth relationship for the C/C composites without and with FLiNaK salt treatment, respectively [178].

SiC/SiC CMCs have good compatibility with liquid fluoride salts. These unique properties of SiC/SiC composites make them strong candidates for structural components such as heat-exchanger, control rod, and other structure components in a MSR [179-182]. However, SiC undergoes corrosion in liquid fluoride salt at high temperature [183]. Key contributors to this corrosion include salt impurities, non-stoichiometric compositions in SiC, and the presence of foreign ions such as $Ni^{2+}$, $Cr^{2+}$ and $Cr^{3+}$, which could be introduced from alloy container corrosion (e.g., Hastelloy N) or salt production [184, 185].

Multiple studies have evaluated the presence of oxygen impurities on corrosion behavior of SiC/SiC composites in fluoride salts. A study investigating the high-temperature corrosion behavior and microstructural evolution of SiC/SiC composites fabricated by using two-dimensional woven fabrics of KD-II SiC fibers reinforced chemical vapor infiltrated SiC designed matrix in FLiNaK eutectic molten salt at 800 °C revealed that Si-rich SiC layers and O-containing boundaries between deposited layers are the most vulnerable regions in SiC/SiC composites, exhibiting significantly lower corrosion resistance compared to near-stoichiometric SiC [186]. Molten salt infiltrates through surface defects such as pores and

cracks, preferentially attacking oxide phases and high-oxygen regions. The Si-O bond in an O-containing SiC phase would be attacked by $F^-$ to form Si-F bonds, indicating that the presence of oxygen impurities in SiC accelerates the corrosion of SiC in fluoride salt [187]. Wang et al. [186] reported that the corrosion followed a linear, reaction-controlled mass loss trend up to 300 h at 800 °C (Figure 5.9); however, exposure at 500 h led to deviations due to the combined effects of chemical attack and exfoliation of SiC layers. The salt may preferentially erode the boundaries between deposition layers leading to more severe exfoliation. The corrosion initiates at weak interfacial regions and progressively penetrates deeper into the matrix, resulting in significant structural degradation.

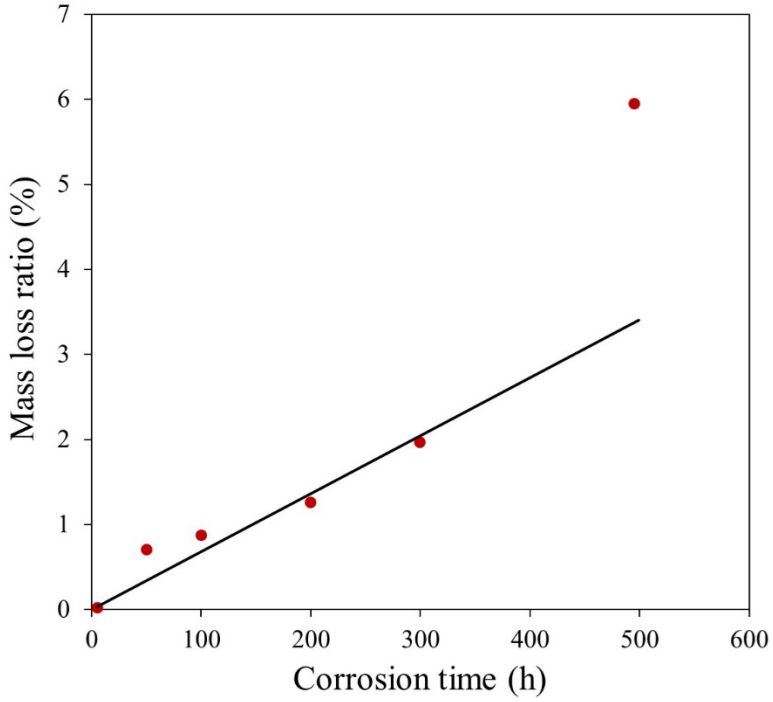


Figure 5.9. Mass loss ratio of samples corroded in 46.5LiF-11.5NaF-42.0KF (mol. %) eutectic salt at 800 °C for various time [186].

Further studies on the corrosion of same SiC/SiC composites at various temperatures (800 - 1000 °C) for 500 h also showed that interlayer boundaries of SiC matrix remain more vulnerable to corrosion in FLiNaK eutectic molten salt compared to near-stoichiometric SiC, primarily due to higher intrinsic oxygen content from repetitive densification cycles during fabrication [188]. As temperature increases, corrosion severity also intensifies. XRD analysis indicated that selective silicon corrosion at elevated temperatures leads to carbon enrichment, and the remaining carbon-enriched SiC can be further oxidized by impurities such as $NO_3^-$ [188]. This results in matrix exfoliation, and significant reductions in mechanical strength. As shown in Figure 5.10, flexural strength retention after 500 h exposure was only 51.6% at 800 °C, 65.26% at 900 °C, and as low as 25.13% at 1000 °C.

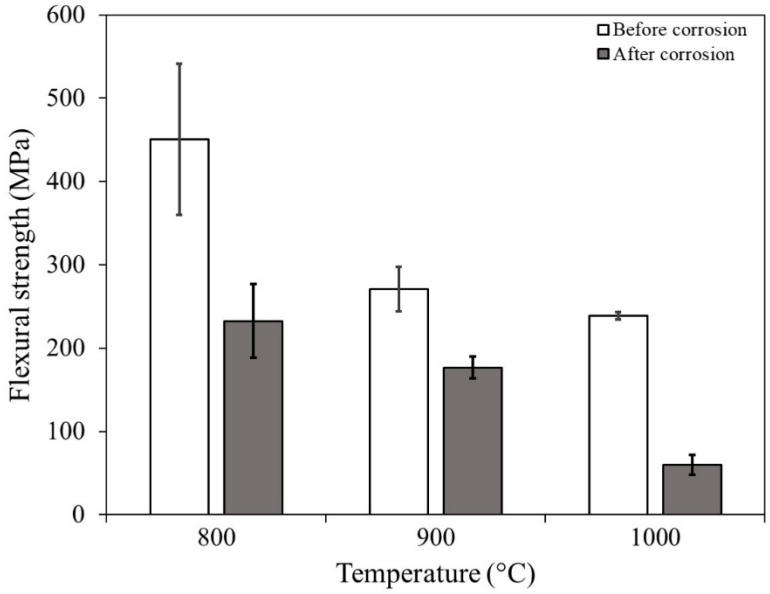


Figure 5.10. High-temperature flexural strength of SiC/SiC composites before and after corrosion in liquid FLiNaK salt at varying temperatures [188].

Long-term corrosion behavior was also assessed for SiC/SiC composites reinforced with Tyranno SA3 and Hi-Nicalon Type S fibers, with corrosion experiments in FLiBe molten salt at 650 °C and 750 °C for 1000 h [189]. Both fiber types exhibited surface corrosion as carbon-rich spotting, with severity increasing at higher temperatures. Despite these surface-level effects, both composites showed weight loss of near or below 3 % of the initial mass at all temperatures and no structural degradation. Thermodynamic analysis confirmed that pure FLiBe salt is highly compatible with SiC, but the presence of water and metallic impurities, specifically oxygen, iron, and nickel, promote carbon deposition. Nishimura et al. found a layer of nickel silicide on the surface of SiC specimens after molten salt exposure at 550 °C in a nickel crucible, attributing corrosion to nickel dissolution and diffusion from the crucible material [190]. SiC corrosion in FLiBe, studied by ab initio molecular dynamics, showed that the standard potentials of solid dissolution in FLiNaK are slightly more negative than in FLiBe, indicating that SiC is more susceptible to corrosion in FLiNaK [191]. It was also reported that the standard potential for Si species is smaller than that of C species, suggesting that the Si species would be much easier to dissolve into the salt than the C species [191]. However, the overall corrosion process remains similar across various fluoride salt systems and is heavily influenced by trace impurities [192]. According to Lee et al. [191, 193], the corrosion mechanism of SiC by FLiNaK or FLiBe involves fluorine ions forming coordinate bonds with Si atoms in SiC, replacing Si–C bonds and creating soluble $[SiF_6]^{2-}$ complexes, and leaving chain- and ring-like carbon structures, as shown in Eq. 11 [189] below:

$$SiC\ (s) + F^-\ (soln) \rightarrow SiF_6^{2-}\ (soln) + C(s) \tag{5.10}$$

At high temperature the $[SiF_6]^{2-}$ could decompose into $SiF_4$ gas and escape out from liquid salt accelerating further dissolution of SiC. The residual C could then be oxidized by impurities such as $NO_3^-$ and could be graphitized, contributing to the degradation of structural integrity. The increase in corrosion temperature accelerates this process, promoting mass loss and weakening of the PyC interphase, which further reduces load-bearing capacity.

In addition to corrosion, tritium is a pervasive issue in FHRs. Tritium is constantly generated from neutron activation of $Li^6$ and $Be^9$ in the FLiBe coolant [194, 195]. The corrosion of structural materials in FHR likely correlates with tritium levels in the coolant; particularly tritium in the form of tritium fluoride (TF), a highly corrosive species that readily reacts with metal surfaces to form soluble metal fluorides and free fluorine ions, so it is necessary to investigate tritium interactions with SiC [196, 197]. SiC/SiC composites, which are being considered for use in FHRs, generally show low tritium permeability and low tritium solubility at high temperatures [198, 199]. Causey et al. showed that the diffusivity of T in SiC was significantly lower and the activation energy was much higher than the diffusivity of T in metals [199]. However, when exposed to irradiation, SiC develops defects such as Si vacancies that can trap tritium atoms and increase their retention [193]. The chemical bonding of tritium to the surface of SiC, as well as the subsequent absorption and then vacancy diffusion of tritium in irradiated SiC structures, is highly dependent on hydrogen partial pressure, temperature, and irradiation conditions [193]. In SiC/SiC composites made by CVI, the C interphase between fibers also plays a role by trapping tritium, although this trapping becomes less effective above 600°C [200, 201]. Additionally, the porous structure of CVI composites affects how tritium moves through them, making their behavior different from that of dense, monolithic SiC [193]. Because of these factors, it is important to study tritium transport and trapping in both SiC and SiC/SiC CMC especially under real reactor conditions in order to better understand how to control tritium release and protect structural materials.

# 6 Pre-service and In-service Inspection Methods

Due to the complex microstructures and multiple processing steps involved in their fabrication, CMC components often contain flaws of various sizes and types ranging from microscopic defects such as interface cracks and matrix porosity to larger defects like delamination and voids. Given the high cost of CMC fabrication, inspecting components using nondestructive testing (NDT) both before service and at regular intervals during operation can help prevent catastrophic failure by monitoring performance and reliability. Several NDT methods – such as thermal imaging, ultrasonic testing (UT), X-ray computed tomography (CT), and acoustic emission (AE) – have demonstrated effectiveness in characterizing CMCs. This chapter provides an overview of these technologies.

## 6.1 Thermal Imaging

Thermal imaging leverages transient heat transfer processes to evaluate material properties, detect defects, and assess damage in components [202]. The method involves applying a thermal impulse to the specimen and measuring its thermal response using an infrared (IR) camera. Depending on the configuration, thermal imaging can operate in two modes: through-transmission and single-sided. In the through-transmission mode, the flash lamps and IR camera are positioned on opposite sides of the specimen to enable mapping of through-thickness thermal diffusivity. In the single-sided mode, both the flash lamps and IR camera are placed on the same side of the specimen.

Several studies [203, 204] have demonstrated the effectiveness of through-transmission thermal imaging in mapping the thermal diffusivity of CMCs. In this approach, the back surface of the sample was heated by an instantaneous thermal impulse, and the rate of heat conduction through the thickness was directly related to the material's thermal diffusivity. Another study [205] highlighted the application of thermal imaging in detecting thermal shock damage in SiC/SiC coupons. These coupons were subjected to water quenching with temperature differences as high as 1000°C. Thermal diffusivity images revealed significant damage at the coupon edges after quenching, as evidenced by reduced thermal diffusivity in these regions.

Thermal imaging has also been employed to measure the depth of delamination in CMCs using a single-sided configuration [206]. After the specimen is flash-heated, the decay rate of surface temperature depends on the heat flux within the material. When the heat flux encounters a delamination—typically filled with air, which has higher thermal resistance – the heat transfer rate is reduced and results in a localized hot spot on the surface. The depth of the delamination can be determined by fitting a theoretical heat transfer model to the measured temperature data. For instance, a SiC/SiC MI panel was tested to evaluate the sensitivity and accuracy of depth detection [206]. The back surface of the panel was machined to contain flat-bottom holes at varying depths and diameters. The study found that depth detection was accurate for holes with a diameter-to-depth ratio larger than three, demonstrating the precision of thermal imaging in quantifying defect dimensions.

### 6.2 Ultrasonic Testing (UT)

UT is a widely used NDT method due to its cost-effectiveness, ease of use, and ability to detect internal flaws in materials. It operates by introducing high-frequency sound waves – typically between 0.1 and 25 MHz – into a material [207]. These waves reflect or scatter upon encountering interfaces or defects, allowing for the detection and characterization of flaws. Several scanning modes are available. The A-scan provides a one-dimensional signal used primarily for thickness measurement. The B-scan arranges A-scans to produce a two-dimensional cross-section, while the C-scan offers a planar view of the defect distribution. C-scans can be obtained using either pulse-echo or through-transmission ultrasonic (TTU) modes. TTU, which uses separate transmitting and receiving transducers on opposite sides of the specimen, is especially effective for materials like CMCs that strongly attenuate ultrasonic waves.

Kim et al. [208] demonstrated how UT can map internal defects in SiC/SiC CMC. Using TTU C-scans with 15 MHz focused transducers, they identified dense regions as those with higher transmitted amplitudes and flaw-rich regions – such as those with cracks or porosity – with lower amplitudes. These amplitude differences, represented in color-mapped images, were later confirmed via scanning electron microscopy which revealed greater porosity in low-amplitude zones.

### 6.3 X-ray Computed Tomography (CT)

X-ray CT provides detailed cross-sectional views of a material's internal structure, making it highly effective for evaluating the integrity of CMCs. Unlike traditional radiography, which captures a 2D projection, X-ray CT reconstructs thin slices – typically 0.025 to 3 mm thick – parallel to the X-ray beam and offers more precise visualization of internal features with pixel resolutions as fine as 0.025 mm [207].

The CT imaging process involves placing the specimen on a computer-controlled rotating table between an X-ray source and a two-dimensional detector. As the specimen rotates, a series of projection images is captured, representing the relative X-ray attenuation at different angles. These images are then processed using advanced reconstruction algorithms to generate cross-sectional slices of the specimen. The gray tones in the reconstructed images correspond to variations in density, allowing for precise mapping of material properties in three dimensions [202].

One experimental study [209] demonstrated the utility of X-ray CT in detecting density variations in a MI SiC/SiC cylinder intended for use as a gas turbine combustor liner. During fabrication, the cylinder experienced a processing upset that resulted in insufficient infiltration leading to localized porosity. CT imaging revealed clear differences in density in the affected regions, which were later confirmed through destructive analysis. This study highlighted the ability of CT to detect spatial variations in density and identify flaws that could compromise the performance of CMC components.

Another study [210] involving X-ray CT characterized delaminations in oxide/oxide CMC combustor liners. CT imaging was used to determine the depth of the delamination. CT data from a detailed 0.5-mm-thick slice at the defect region showed lower density at a depth of approximately 0.5–1 mm from the outer surface. The depth was also predicted by thermal imaging which closely matched the CT results, demonstrating the complementary nature of these NDT methods in characterizing defects.

### 6.4 Acoustic Emissions (AE)

AE can monitor the evolution of damage in real time. When materials are stressed, the formation of microcracks, delaminations, or other structural changes generates transient elastic waves. These waves, or emissions, can be detected by piezoelectric sensors that convert them into electrical signals for analysis [207]. For CMCs, AE activity often increases before macroscopic fracture occurs, offering a way to detect the onset of damage or predict imminent failure.

Several studies [211, 212] used AE to monitor damage accumulation in CMCs during tensile tests. Shiwa et al. [211] demonstrated that distinct AE signatures could be associated with specific fracture mechanisms, including matrix cracking, interfacial debonding, and fiber pull-out in SiC/SiC composites. AE has also shown predictive capabilities for fatigue failure in ceramics [213].

# 7 Conclusions

In summary, this report reviews the literature related to C/C and SiC/SiC CMCs for potential use in high-temperature nuclear environments. By examining fabrication processes, irradiation performance, oxidation resistance, and structural failure mechanisms, several key takeaways emerge:

1. Fabrication processes and impurities:

    - Both C/C and SiC/SiC CMCs rely on carefully controlled manufacturing processes – such as CVI, liquid densification, and NITE – to achieve the desired mechanical and thermal properties.

    - Stringent limits on impurities (particularly boron, iron, and various metallic and nonmetallic elements) are critical to ensuring stable performance under irradiation and reducing detrimental activation and oxidation.

2. Structural modeling and failure analysis

    - Both C/C and SiC/SiC CMCs fail progressively rather than catastrophically, where initial matrix cracking is followed by interphase debonding, fiber bridging, and eventually fiber pull-out or fracture.

    - A range of modeling approaches – from micromechanical to continuum damage and PFA – helps predict the path to failure. Current research focuses on coupling these models with oxidation, corrosion, and irradiation effects for more comprehensive life-prediction.

3. Material properties in unirradiated and irradiated states

    - C/C CMCs generally display improved mechanical strength and stiffness following low-dose neutron irradiation that is attributed to irradiation-induced defect pinning and reduced porosity. At higher doses, the composites may experience significant dimensional instability, especially if they surpass the turnaround point where shrinkage transitions to swelling.

    - Near-stoichiometric SiC/SiC CMCs maintain good mechanical properties after neutron irradiation across a wider range of doses and temperatures. While the Young's modulus can decrease slightly, the PLS and UTS often remain largely unaffected by moderate to high doses.

    - Thermal conductivity decreases for both C/C and SiC/SiC composites following neutron irradiation, which is linked to defect-induced phonon scattering.

4. Oxidation and corrosion resistance

   - C/C CMCs are vulnerable to oxidation at temperatures above ~450 °C. Repeated oxidation–reduction cycles and resulting weight loss degrade mechanical and thermal performance, especially at fiber-matrix interfaces. Protective coatings and high-crystallinity carbon can mitigate, but not eliminate, oxidation damage.

   - SiC/SiC composites exhibit greater oxidation resistance as compared to C/C CMCs because of the formation of protective silica layers. However, prolonged exposure at moderate temperatures can lead to the embrittlement of PyC interphases and slow crack growth in fibers.

   - Corrosion in molten fluoride salts remains a concern for SiC/SiC CMCs if salt impurities and high oxygen content are present. Preventive measures to reduce localized attack at matrix interphases and fiber surfaces include careful compositional control, high-crystallinity fibers, and improved manufacturing to reduce oxygen-rich phases.

5. Inspection techniques

   - Nondestructive testing is important for ensuring structural integrity throughout a composite's service life. Methods such as thermal imaging, UT, X-ray CT, and AE techniques have demonstrated success in detecting cracks, delamination, and porosity.

## Acknowledgements

This work was sponsored by the U.S. Department of Energy, under Contract No. DE-AC02-06CH11357 with Argonne National Laboratory, managed and operated by UChicago Argonne LLC. Funding was provided by the U.S. Nuclear Regulatory Commission (NRC), Office of Nuclear Regulatory Research (RES) under agreement 31310023S0072. The authors would like to thank Joe Bass and other NRC staff members for their helpful feedback and suggestions.

## Bibliography

1. David, P., Carbon/carbon materials for Generation IV nuclear reactors, in Structural materials for generation IV nuclear reactors. 2017, Elsevier. p. 471-493.

2. Park, J. Y. "SiCf/SiC composites as core materials for Generation IV nuclear reactors." Structural materials for generation IV nuclear reactors. Woodhead Publishing, 2017. 441-470.

3. Li, Longbiao. High temperature mechanical behavior of ceramic-matrix composites. John Wiley & Sons, 2021.

4. Rashid, Adib Bin, et al. "Breaking Boundaries with Ceramic Matrix Composites: A Comprehensive Overview of Materials, Manufacturing Techniques, Transformative Applications, Recent Advancements, and Future Prospects." Advances in Materials Science and Engineering 2024.1 (2024): 2112358.

5. Buckley, J.D. and D.D. Edie, Carbon-carbon materials and composites. 1993: William Andrew.

6. Thomas, C.R., Essentials of carbon-carbon composites. 1993: The Royal Society of Chemistry, Cambridge.

7. Weiß, R., Carbon/carbons and their industrial applications. Ceramic matrix composites: fiber reinforced ceramics and their applications, 2008: p. 85-146.

8. Bansal, N.P. and J. Lamon, Ceramic matrix composites: materials, modeling and technology. 2014: John Wiley & Sons.

9. Yin, X., et al., Recent progress in 1D nanostructures reinforced carbon/carbon composites. Advanced Functional Materials, 2022. 32(35): p. 2204965.

10. Han, M., C. Zhou, and H. Zhang, A mesoscale beam-spring combined mechanical model of needle-punched carbon/carbon composite. Composites Science and Technology, 2018. 168: p. 371-380.

11. Liu, F., Z. Guan, and T. Bian, Damage model for predicting shear strength of carbon/carbon composite fastener based on post-failure behavior. Composite Structures, 2019. 221: p. 110864.

12. Wang, T., et al., Dependence of mechanical properties on microstructure of high-textured pyrocarbon prepared via isothermal and thermal gradient chemical vapor infiltration. Composites Part B: Engineering, 2020. 192: p. 107982.

13. Wang, T., et al., The effect of microstructural evolution on micromechanical behavior of pyrolytic carbon after heat treatment. Diamond and Related Materials, 2020. 103: p. 107729.

14. Hatta, H., R. Weiss, and P. David, Carbon/carbons and their industrial applications. Ceramic Matrix Composites: Materials, Modeling and Technology, 2014: p. 85-146.

15. Ahn, H., et al., Microstructure and mechanical properties of polyacrylonitrile precursor fiber with dry and wet drawing process. Polymers, 2021. 13(10): p. 1613.

16. Sauder, C., Ceramic matrix composites: nuclear applications. Ceramic matrix composites: materials, modeling and technology, 2014: p. 609-646.

17. Bilisik, K., Multiaxis three-dimensional weaving for composites: a review. Textile Research Journal, 2012. 82(7): p. 725-743.

18. Bilisik, K., Three-dimensional braiding for composites: A review. Textile research journal, 2013. 83(13): p. 1414-1436.

19. Coltelli, M.-B. and A. Lazzeri, Chapter X Recent advances in CVI of composites and their applications.

20. Geringer, J.W. and T. Burchell, Status Report on ASME Code Development for Nonmetallic Core Components in 2020. 2020, Oak Ridge National Laboratory (ORNL), Oak Ridge, TN (United States).

21. Park, S.-J. and S.-J. Park, Carbon/carbon composites. Carbon Fibers, 2018: p. 279-294.

22. Yajima, S., et al., Development of a silicon carbide fibre with high tensile strength. Nature, 1976. 261(5562): p. 683-685.

23. Ichikawa, H., Development of high performance SiC fibers derived from polycarbosilane using electron beam irradiation curing-a review. Journal of the Ceramic Society of Japan, 2006. 114(1330): p. 455-460.

24. Katoh, Y., et al., Continuous SiC fiber, CVI SiC matrix composites for nuclear applications: Properties and irradiation effects. Journal of Nuclear Materials, 2014. 448(1-3): p. 448-476.

25. Takeda, M., et al., Effect of hydrogen atmosphere on pyrolysis of cured polycarbosilane fibers. Journal of the American Ceramic Society, 2000. 83(5): p. 1063-1069.

26. Ishikawa, T., et al., High-strength alkali-resistant sintered SiC fibre stable to 2,200 C. Nature, 1998. 391(6669): p. 773-775.

27. Lipowitz, J., et al. Structure and properties of Sylramic™ silicon carbide fiber—A polycrystalline, stoichiometric β-SiC composition. in Proceedings of the 21st annual conference on composites, advanced ceramics, materials, and structures—a: ceramic engineering and science proceedings. 1997. Wiley Online Library.

28. Snead, M.A., et al., SiC/SiC Cladding Materials Properties Handbook. 2017, Oak Ridge National Laboratory (ORNL), Oak Ridge, TN (United States).

29. Yang, W., et al., Hi-NicalonTM fiber-reinforced CVI-SiC matrix composites: I effects of PyC and PyC-SiC multilayers on the fracture behaviors and flexural properties. Materials transactions, 2002. 43(10): p. 2568-2573.

30. Yang, W., et al., Effect of carbon and silicon carbide/carbon interlayers on the mechanical behavior of Tyranno-SA-fiber-reinforced silicon carbide-matrix composites. Journal of the American Ceramic Society, 2003. 86(5): p. 851-856.

31. Katoh, Y., et al., Mechanical properties of chemically vapor-infiltrated silicon carbide structural composites with thin carbon interphases for fusion and advanced fission applications. Materials transactions, 2005. 46(3): p. 527-535.

32. Katoh, Y., T. Nozawa, and L.L. Snead, Mechanical Properties of Thin Pyrolitic Carbon Interphase SiC–Matrix Composites Reinforced with Near-Stoichiometric SiC Fibers. Journal of the American Ceramic Society, 2005. 88(11): p. 3088-3095.

33. Lowden, R.A., Characterization and control of the fiber-matrix interface in ceramic matrix composites. 1989.

34. Nozawa, T., Y. Katoh, and L.L. Snead, The effects of neutron irradiation on shear properties of monolayered PyC and multilayered PyC/SiC interfaces of SiC/SiC composites. Journal of nuclear materials, 2007. 367: p. 685-691.

35. Bansal, N.P., Handbook of ceramic composites. Vol. 200. 2006: Springer Science & Business Media.

36. Katoh, Y., et al., Progress in SiC-based ceramic composites for fusion applications. Fusion science and technology, 2003. 44(1): p. 155-162.

37. Xu, Y., et al., Microstructure and Mechanical Properties of Three-Dimensional Textile Hi-Nicalon SiC/SiC Composites by Chemical Vapor Infiltration. Journal of the American Ceramic Society, 2002. 85(5): p. 1217-1221.

38. Deck, C., et al., Fabrication of SiC–SiC composites for fuel cladding in advanced reactor designs. Progress in Nuclear Energy, 2012. 57: p. 38-45.

39. Katoh, Y., S. Dong, and A. Kohyama, Thermo-mechanical properties and microstructure of silicon carbide composites fabricated by nano-infiltrated transient eutectoid process. Fusion Engineering and Design, 2002. 61: p. 723-731.

40. Kohyama, A. and H. Kishimoto, SiC/SiC composite materials for nuclear applications. International Electronic Journal of Nuclear Safety and Simulation, 2013. 4.

41. Dong, S., Y. Katoh, and A. Kohyama, Preparation of SiC/SiC composites by hot pressing, using Tyranno-SA fiber as reinforcement. Journal of the American Ceramic Society, 2003. 86(1): p. 26-32.

42. Shimoda, K., A. Kohyama, and T. Hinoki, High mechanical performance SiC/SiC composites by NITE process with tailoring of appropriate fabrication temperature to fiber volume fraction. Composites Science and Technology, 2009. 69(10): p. 1623-1628.

43. Katoh, Y., Status and prospects of SiC-based ceramic composites for fusion and advanced fission applications. Purazuma, Kaku Yugo Gakkai-Shi, 2004. 80.

44. Kohyama, A., J.-S. Park, and H.-C. Jung, Advanced SiC fibers and SiC/SiC composites toward industrialization. Journal of Nuclear Materials, 2011. 417(1-3): p. 340-343.

45. Noda, T., Advanced SiC-SiC composites for nuclear application. Handbook of Advanced Ceramics and Composites: Defense, Security, Aerospace and Energy Applications, 2020: p. 641-666.

46. Kotani, M., et al. Fabrication of high performance SiC/SiC composite by polymer impregnation and pyrolysis method. in 23rd Annual Conference on Composites, Advanced Ceramics, Materials, and Structures: B: Ceramic Engineering and Science Proceedings. 1999. Wiley Online Library.

47. Kotani, M., et al., Fabrication and oxidation-resistance property of allylhydridopolycarbosilane-derived SiC/SiC composites. Journal of the Ceramic Society of Japan, 2003. 111(1293): p. 300-307.

48. Lee, S., et al., High temperature characterization of reaction sintered SiC based materials. Journal of nuclear materials, 2004. 329: p. 534-538.

49. Lee, S., et al. Microstructure and bending properties of SiC/SiC composites fabricated by reaction sintering process. in 24th Annual Conference on Composites, Advanced Ceramics, Materials, and Structures: A: Ceramic Engineering and Science Proceedings. 2000. Wiley Online Library.

50. Shimoda, K., et al., Influence of pyrolytic carbon interface thickness on microstructure and mechanical properties of SiC/SiC composites by NITE process. Composites Science and Technology, 2008. 68(1): p. 98-105.

51. Geringer, J.W., et al. ASME Code Rules and ASTM Standards Integration for Ceramic Composite Core Materials and Components1. in Journal of Physics: Conference Series. 2021. IOP Publishing.

52. Krenkel, Walter, ed. Ceramic matrix composites: fiber reinforced ceramics and their applications. John Wiley & Sons, 2008.

53. Marshall, David B., and Anthony G. Evans. "Failure mechanisms in ceramic-fiber/ceramic-matrix composites." Journal of the American Ceramic Society 68.5 (1985): 225-231.

54. Bansal, Narottam P., and Jacques Lamon. Ceramic matrix composites: materials, modeling and technology. John Wiley & Sons, 2014.

55. Li, Longbiao. Damage, fracture, and fatigue of ceramic-matrix composites. New York: Springer, 2018.

56. Davidge, R. W. "the mechanical properties and fracture behaviour of ceramic-matrix composites (CMC) reinforced with continuous fibres." Composite materials series 6 (1989): 547-569.

57. Chawla, Krishan K., and Krishan K. Chawla. "Ceramic matrix composites." Composite Materials: Science and Engineering (2012): 249-292.

58. Evans, A. G., F. W. Zok, and T. J. Mackin. "The structural performance of ceramic matrix composites." High Temperature Mechanical Behaviour of Ceramic Composites. Butterworth-Heinemann, 1995. 3-84.

59. Farahmand, Bahram. "Ceramic Matrix Composites (CMCs)(Methods of Manufacturing CMC Parts)." Fundamentals of Composites and Their Methods of Fabrications: PMCs, MMCs, and CMCs. Cham: Springer Nature Switzerland, 2025. 129-159.

60. Jacobson, Nathan S., Elizabeth J. Opila, and Kang N. Lee. "Oxidation and corrosion of ceramics and ceramic matrix composites." Current Opinion in Solid State and Materials Science 5.4 (2001): 301-309.

61. Nutt, S. R. "Environmental effects on high temperature mechanical behavior of ceramic matrix composites." High Temperature Mechanical Behaviour of Ceramic Composites. Butterworth-Heinemann, 1995. 365-406.

62. Pavia, F., and W. A. Curtin. "Optimizing strength and toughness of nanofiber-reinforced CMCs." Journal of the Mechanics and Physics of Solids 60.9 (2012): 1688-1702.

63. Budiansky, Bernard, John W. Hutchinson, and Anthony G. Evans. "Matrix fracture in fiber-reinforced ceramics." Journal of the Mechanics and Physics of Solids 34.2 (1986): 167-189.

64. Thouless, Michael D., and Anthony G. Evans. "Effects of pull-out on the mechanical properties of ceramic-matrix composites." Acta Metallurgica 36.3 (1988): 517-522.

65. Curtin, W. A. "Fiber pull-out and strain localization in ceramic matrix composites." Journal of the Mechanics and Physics of Solids 41.1 (1993): 35-53.

66. Hild, François, Alain Burr, and Frederick A. Leckie. "Fiber breakage and fiber pull-out of fiber-reinforced ceramic-matrix composites." European Journal of Mechanics-A/Solids 13.6 (1994): 731-749.

67. Kumar, Rajesh S., and Gregory S. Welsh. "Delamination failure in ceramic matrix composites: Numerical predictions and experiments." Acta Materialia 60.6-7 (2012): 2886-2900.

68. Sbaizero, Orfeo, Panos G. Charalambides, and Anthony G. Evans. "Delamination Cracking in a Laminated Ceramic-Matrix Composite." Journal of the American Ceramic Society 73.7 (1990): 1936-1940.

69. Tripp, D. E., J. H. Hemann, and J. P. Gyekenyesi. "A review of failure models for ceramic matrix composite laminates under monotonic loads." (1990): 492-501.

70. Azzi, V. D., and Stephen W. Tsai. "Anisotropic strength of composites: Investigation aimed at developing a theory applicable to laminated as well as unidirectional composites, employing simple material properties derived from unidirectional specimens alone." Experimental mechanics 5 (1965): 283-288.

71. Tsai, Stephen W., and Edward M. Wu. "A general theory of strength for anisotropic materials." Journal of composite materials 5.1 (1971): 58-80.

72. Waddoups, Mo E., Jo R. Eisenmann, and B. Eo Kaminski. "Macroscopic fracture mechanics of advanced composite materials." Journal of composite materials 5.4 (1971): 446-454.

73. Whitney, James M., and Ralph J. Nuismer. "Stress fracture criteria for laminated composites containing stress concentrations." Journal of composite materials 8.3 (1974): 253-265.

74. Nuismer, R. J., and J. Me Whitney. "Uniaxial failure of composite laminates containing stress concentrations." Fracture mechanics of composites. ASTM International, 1975.

75. Hedgepeth, John M., and Peter Van Dyke. "Local stress concentrations in imperfect filamentary composite materials." Journal of composite materials 1.3 (1967): 294-309.

76. Aveston, J., Cooper, G. A., and A. Kelly. "Single and multiple fracture." The properties of fibre composites Proceedings Conf. National Physical Laboratories, IPC Science & Technology Press Ltd., London, UK. 1971.

77. Budiansky, Bernard, John W. Hutchinson, and Anthony G. Evans. "Matrix fracture in fiber-reinforced ceramics." Journal of the Mechanics and Physics of Solids 34.2 (1986): 167-189.

78. Marshall, D. B., Bo N. Cox, and Ao G. Evans. "The mechanics of matrix cracking in brittle-matrix fiber composites." Acta metallurgica 33.11 (1985): 2013-2021.

79. Sidoroff, F. "Damage mechanics and its application to composite materials." Mechanical characterisation of load bearing fibre composite laminates (1985): 21-35.

80. Talreja, Ramesh. "Stiffness properties of composite laminates with matrix cracking and interior delamination." Engineering Fracture Mechanics 25.5-6 (1986): 751-762.

81. Wnuk, M. P., and R. D. Kriz. "CDM model of damage accumulation in laminated composites." International journal of fracture 28 (1985): 121-138.

82. Alabdullah, Mohammad, and Nasr M. Ghoniem. "A thermodynamics-based damage model for the non-linear mechanical behavior of SiC/SiC ceramic matrix composites in irradiation and thermal environments." International Journal of Damage Mechanics 29.10 (2020): 1569-1599.

83. Ladevèze, Pierre, Gilles Lubineau, and David Marsal. "Towards a bridge between the micro- and mesomechanics of delamination for laminated composites." Composites Science and Technology 66.6 (2006): 698-712.

84. Wetherhold, Robert C., and R. Byron Pipes. "Statistics of fracture of composite materials under multiaxial loading." Materials Science and Engineering 68.1 (1984): 113-118.

85. Cassenti, B. N. "Probabilistic static failure of composite material." AIAA journal 22.1 (1984): 103-110.

86. Zweben, Carl, and B. Walter Rosen. "A statistical theory of material strength with application to composite materials." Journal of the Mechanics and Physics of Solids 18.3 (1970): 189-206.

87. Harlow, D. Gary, and S. Leigh Phoenix. "The chain-of-bundles probability model for the strength of fibrous materials I: analysis and conjectures." Journal of composite materials 12.2 (1978): 195-214.

88. Farahmand, Bahram. "Progressive Failure Analysis (PFA) of Laminated Composites." Fundamentals of Composites and Their Methods of Fabrications: PMCs, MMCs, and CMCs. Cham: Springer Nature Switzerland, 2025. 175-196.

89. Ochoa, Ozden O., et al. Finite element analysis of composite laminates. Springer Netherlands, 1992.

90. Sleight, David W. Progressive failure analysis methodology for laminated composite structures. No. NAS 1.60: 209107. 1999.

91. Hashin, Zvi. "Failure criteria for unidirectional fiber composites." (1980): 329-334.

92. Christensen, Richard M. "A Comprehensive Theory of Yielding and Failure for Isotropic Materials." Journal of Engineering Materials and Technology 129 (2007): 173.

93. Murray, Y., and L. Schwer. "Implementation and verification of fiber-composite damage models, Failure Criteria and Analysis in Dynamic Response." (1990): 21-30.

94. Highsmith, Alton L. Stiffness reduction resulting from transverse cracking in fiber-reinforced composite laminates. Diss. Virginia Polytechnic Institute and State University, 1981.

95. Nahas, Mahmoud N. "Survey of failure and post-failure theories of laminated fiber-reinforced composites." Composites Technology and Research 8.4 (1986): 138-153.

96. Reddy, Yeruva S., and Junuthula N. Reddy. "Three-dimensional finite element progressive failure analysis of composite laminates under axial extension." Composites Technology and Research 15.2 (1993): 73-87.

97. Artz, Timothy, et al. "Computational model for oxidation-assisted rupture of ceramic matrix composites." International Journal of Solids and Structures (2020): 195-207.

98. Morscher, Gregory N., Janet Hurst, and David Brewer. "Intermediate-temperature stress rupture of a woven Hi-Nicalon, BN-interphase, SiC-matrix composite in air." Journal of the American Ceramic Society 83.6 (2000): 1441-1449.

99. Ogbuji, Linus UJT. "Recent developments in the environmental durability of SiC/SiC composites." CIMTEC 2002 International Conferences on Modern Materials and Technologies. No. NAS 1.26: 211687. 2002.

100. Xu, Wenbo, Frank W. Zok, and Robert M. McMeeking. "Model of oxidation-induced fiber fracture in SiC/SiC composites." Journal of the American Ceramic Society 97.11 (2014): 3676-3683.

101. Iyengar, N., and W. A. Curtin. "Time-dependent failure in fiber-reinforced composites by fiber degradation." Acta Materialia 45.4 (1997): 1489-1502.

102. Artz, Timothy. Modeling Lifetime Performance of Ceramic Matrix Composites with Reduced Order Homogenization Multiscale Methods. Columbia University, 2022.

103. Cluzel, Christophe, et al. "Mechanical behaviour and lifetime modelling of self-healing ceramic-matrix composites subjected to thermomechanical loading in air." Composites Part A: Applied Science and Manufacturing 40.8 (2009): 976-984.

104. Genet, Martin, et al. "Computational prediction of the lifetime of self-healing CMC structures." Composites Part A: Applied Science and Manufacturing 43.2 (2012): 294-303.

105. Evans, A. G., and C. Weber. "Creep damage in SiC/SiC composites." Materials Science and Engineering: A 208.1 (1996): 1-6.

106. Begley, M. R., A. G. Evans, and R. M. McMeeking. "Creep rupture in ceramic matrix composites with creeping fibers." Journal of the Mechanics and Physics of Solids 43.5 (1995): 727-740.

107. Ruggles-Wrenn, Marina, Nicholas Boucher, and Craig Przybyla. "Fatigue of three advanced SiC/SiC ceramic matrix composites at 1200° C in air and in steam." International Journal of Applied Ceramic Technology 15.1 (2018): 3-15.

108. Luo, Zheng, et al. "Tension-tension fatigue behavior of a PIP SiC/SiC composite at elevated temperature in air." Ceramics International 42.2 (2016): 3250-3260.

109. Mizuno, Mineo, et al. "Cyclic-fatigue behavior of SiC/SiC composites at room and high temperatures." Journal of the American Ceramic Society 79.12 (1996): 3065-3077.

110. Ladevèze, Pierre, et al. "Damage and lifetime modeling for structure computations." Ceramic Matrix Composites: Materials, Modeling and Technology (2014): 465-519.

111. Jin, Enze, et al. "Effect of interface coating on high temperature mechanical properties of SiC–SiC composite using domestic Hi–Nicalon type SiC fibers." Coatings 10.5 (2020): 477.

112. Jing, Xin, et al. "Deformation and rupture behaviors of SiC/SiC under creep, fatigue and dwell-fatigue load at 1300 C." Ceramics International 45.17 (2019): 21440-21447.

113. Rugg, Kevin L., et al. "Creep of SiC–SiC microcomposites." Journal of the European Ceramic Society 19.13-14 (1999): 2285-2296.

114. Almansour, Amjad S., and Gregory N. Morscher. "Tensile creep behavior of SiCf/SiC ceramic matrix minicomposites." Journal of the European Ceramic Society 40.15 (2020): 5132-5146.

115. Khafagy, Khaled H., et al. "Modeling creep behavior in ceramic matrix composites." Ceramics International 47.9 (2021): 12651-12660.

116. Grujicic, Mica, et al. "Material constitutive models for creep and rupture of SiC/SiC ceramic-matrix composites (CMCs) under multiaxial loading." Journal of Materials Engineering and Performance 25 (2016): 1697-1708.

117. Arnold, Steven M., et al. "Combining material and model pedigree is foundational to making ICME a reality." Integrating Materials and Manufacturing Innovation 4 (2015): 37-62.

118. Bednarcyk, Brett A., et al. "Multiscale modeling of ceramic matrix composites." 56th AIAA/ASCE/AHS/ASC Structures, Structural Dynamics, and Materials Conference. 2015.

119. Aboudi, Jacob, Steven M. Arnold, and Brett A. Bednarcyk. Micromechanics of composite materials: a generalized multiscale analysis approach. Butterworth-Heinemann, 2012.

120. Lamon, Jacques, and Adrien Laforêt. "Static Fatigue of SiC/SiC Minicomposites at High Temperatures Up to 1200° C in Air: Multiscale Approach." Journal of Composites Science 5.3 (2021): 67.

121. Longbiao, Li. "A hysteresis energy dissipation based model for multiple loading damage in continuous fiber-reinforced ceramic-matrix composites." Composites Part B: Engineering 162 (2019): 259-273.

122. ARNOLD, STEVEN, et al. "Multiscale Modeling of Random Microstructures in SiC/SiC Ceramic Matrix Composites within MAC/GMC Framework." Proceedings of the American Society for Composites: Thirty-First Technical Conference. 2016.

123. Zhang, Long, et al. "Experimental investigation and multiscale simulation on the bending fatigue of 2D SiCf/SiC composites." International Journal of Fatigue 144 (2021): 106051.

124. Zheng, Jincheng, et al. "A multi-scale submodel method for fatigue analysis of braided composite structures." Materials 14.15 (2021): 4190.

125. Liu, Changqi, et al. "A novel creep-fatigue life evaluation method for ceramic-composites components." International Journal of Mechanical Sciences 249 (2023): 108259.

126. Snead, Lance L., et al. "Handbook of SiC properties for fuel performance modeling." Journal of Nuclear Materials 371.1-3 (2007): 329-377.

127. Stone, J. G., et al. "Stress analysis and probabilistic assessment of multi-layer SiC-based accident tolerant nuclear fuel cladding." Journal of Nuclear Materials 466 (2015): 682-697.

128. Ben-Belgacem, M., et al. "Thermo-mechanical analysis of LWR SiC/SiC composite cladding." Journal of Nuclear Materials 447.1-3 (2014): 125-142.

129. Singh, Gyanender, Kurt Terrani, and Yutai Katoh. "Thermo-mechanical assessment of full SiC/SiC composite cladding for LWR applications with sensitivity analysis." Journal of Nuclear Materials 499 (2018): 126-143.

130. Deng, Yangbin, et al. "Probabilistic view of SiC/SiC composite cladding failure based on full core thermo-mechanical response." Journal of Nuclear Materials 507 (2018): 24-37.

131. Alabdullah, Mohammad, and Nasr M. Ghoniem. "A thermodynamics-based damage model for the non-linear mechanical behavior of SiC/SiC ceramic matrix composites in irradiation and thermal environments." International Journal of Damage Mechanics 29.10 (2020): 1569-1599.

132. Burchell, T.D., Radiation damage in carbon–carbon composites: structure and property effects. Physica scripta, 1996. 1996(T64): p. 17.

133. Snead, L., T. Burchell, and A. Qualls. “Strength of neutron-irradiated high-quality 3D carbon fiber composite.” Journal of Nuclear Materials, 2003. 321(2-3): p. 165-169.

134. Burchell, T. and T. Oku, Material properties data for fusion reactor plasma facing carbon-carbon composites. Atomic and Plasma-Material Interaction Data for Fusion, 1994. 5: p. 77-128.

135. Krenkel, W., Ceramic matrix composites: fiber reinforced ceramics and their applications. 2008: John Wiley & Sons.

136. Bonal, J.P., et al. “Neutron induced dimensional changes in carbon materials at high temperatures and high damage doses.” Journal of Nuclear Materials, 1994. 212: p. 1218-1222.

137. Bonal, J. and C. Wu. “Neutron irradiation effects on carbon based materials at 350° C and 800° C.” Journal of Nuclear Materials, 2000. 277(2-3): p. 351-359.

138. Bonal, J. and C. Wu, Neutron irradiation effects on the thermal conductivity and the dimensional stability of carbon fiber composites. Physica Scripta, 1996. 1996(T64): p. 26.

139. Shibata, T., et al., Irradiation-Induced Property Change of C/C Composite for Application of Control rod Elements of Very High Temperature Reactor (VHTR). Structural Materials for Innovative Nuclear Systems (SMINS-2), 2012: p. 69-78.

140. Eto, M., et al. Research and developments on application of carbon-carbon composite to HTGR/VHTR in Japan. in IOP Conference Series: Materials Science and Engineering. 2011. IOP Publishing.

141. Bonal, J. and C. Wu. "Neutron irradiation effects on the thermal conductivity and dimensional stability of carbon fiber composites at divertor conditions." Journal of Nuclear Materials, 1996. 228(2): p. 155-161.

142. Hofer, W.O. and J. Roth, Physical processes of the interaction of fusion plasmas with solids. Academic Press, San Diego, 1996.

143. Shibata, T., et al. "Research and developments on C/C composite for Very High Temperature Reactor (VHTR) application." Ceramic Engineering and Science Proceedings. 2009.

144. Burchell, T.D., Irradiation-induced structure and property changes in tokamak plasma-facing, carbon-carbon composites. 1994, Oak Ridge National Lab., TN (United States).

145. Snead, L., T. Burchell, and Y. Katoh. "Swelling of nuclear graphite and high quality carbon fiber composite under very high irradiation temperature." Journal of Nuclear Materials, 2008. 381(1-2): p. 55-61.

146. Snead, L., Ceramic structural composites. The most advanced structural material. International School on Fusion Reactor Technology, Erice, Italy, 2004.

147. Koyanagi, T., et al. "Effects of neutron irradiation on mechanical properties of silicon carbide composites fabricated by nano-infiltration and transient eutectic-phase process." Journal of Nuclear Materials, 2014. 448(1-3): p. 478-486.

148. Snead, L.L., et al. "Handbook of SiC properties for fuel performance modeling. Journal of Nuclear Materials." 2007. 371(1-3): p. 329-377.

149. Hua, Y., et al., Microstructure and mechanical properties of SiC P/SiC and SiC W/SiC composites by CVI. Journal of Materials Science, 2010. 45: p. 392-398.

150. Koyanagi, T., Y. Katoh, and T. Nozawa, Design and strategy for next-generation silicon carbide composites for nuclear energy. Journal of Nuclear Materials, 2020. 540: p. 152375.

151. Katoh, Y., et al., Mechanical properties of advanced SiC fiber composites irradiated at very high temperatures. Journal of Nuclear Materials, 2011. 417(1-3): p. 416-420.

152. Hollenberg, G., et al., The effect of irradiation on the stability and properties of monolithic silicon carbide and SiCf/SiC composites up to 25 dpa. Journal of Nuclear Materials, 1995. 219: p. 70-86.

153. Jones, R.H., et al., Promise and challenges of SiCf/SiC composites for fusion energy applications. Journal of Nuclear Materials, 2002. 307: p. 1057-1072.

154. Koyanagi, T., S. Kondo, and T. Hinoki, The influence of sintering additives on the irradiation resistance of NITE SiC. Journal of Nuclear Materials, 2011. 417(1-3): p. 435-439.

155. Ozawa, K., et al., Fusion Materials Semiannual Progress. 2009, Report DOE/ER-0313/46.

156. Terrani, K.A., et al., Irradiation stability and thermo-mechanical properties of NITE-SiC irradiated to 10 dpa. Journal of Nuclear Materials, 2018. 499: p. 242-247.

157. Katoh, Y., et al., Stability of SiC and its composites at high neutron fluence. Journal of Nuclear Materials, 2011. 417(1-3): p. 400-405.

158. Shibata, T., et al., Non-destructive evaluation methods for degradation of IG-110 and IG-430 graphite. Journal of Nuclear Materials, 2008. 381(1-2): p. 165-170.

159. Sumita, J., et al. Study on fracture behavior of 2D-C/C composite for application to control rod of Very High Temperature Reactor. in IOP Conference Series: Materials Science and Engineering. 2011. IOP Publishing.

160. Sumita, J., et al., Investigation of microstructural change by X-ray tomography and anisotropic effect on thermal property of thermally oxidized 2D-C/C composite for very high temperature reactor. Journal of nuclear science and technology, 2010. 47(4): p. 411-420.

161. Buckthorpe, D. Results from EU 5th Framework HTR Projects HTR-M & HTR-M1. in Proceedings of the Conference on High Temperature Reactors HTR-2004. 2004.

162. Roy, J., et al., Oxidation behaviour of silicon carbide-a review. Reviews on Advanced Materials Science, 2014. 38(1).

163. Koyanagi, T., et al., SiC/SiC cladding materials properties handbook. Nuclear Technology Research and Development, 2017.

164. Frety, N., R. Molins, and M. Boussuge, Oxidizing ageing effects on SiC-SiC composites. Journal of Materials Science, 1992. 27: p. 5084-5090.

165. Fitzgerald, K. and D. Shepherd, Review of SiCf/SiCm corrosion, erosion and erosion-corrosion in high temperature helium relevant to GFR conditions. Journal of Nuclear Materials, 2018. 498: p. 476-494.

166. Wang, L.-Y., et al., Oxidation resistance of SiCf/SiC composites with a PyC/SiC multilayer interface at 500° C to 1100° C. Corrosion Science, 2020. 167: p. 108522.

167. Gauthier, W., et al., Oxidation of silicon carbide fibers during static fatigue in air at intermediate temperatures. Journal of the American Ceramic Society, 2009. 92(9): p. 2067-2073.

168. Gauthier, W. and J. Lamon, Delayed failure of Hi-Nicalon and Hi-Nicalon S multifilament tows and single filaments at intermediate temperatures (500–800 C). Journal of the American Ceramic Society, 2009. 92(3): p. 702-709.

169. Katoh, Y., et al., SiC/SiC composites through transient eutectic-phase route for fusion applications. Journal of Nuclear Materials, 2004. 329: p. 587-591.

170. Simnad, M.T., Nuclear reactor materials and fuels. 2002.

171. Romatoski, R.R. and L.-W. Hu, Fluoride salt coolant properties for nuclear reactor applications: A review. Annals of Nuclear Energy, 2017. 109: p. 635-647.

172. Katoh, Y., et al., Current status and recent research achievements in SiC/SiC composites. Journal of Nuclear Materials, 2014. 455(1-3): p. 387-397.

173. Qin, F., et al., Oxidation kinetics and mechanisms of carbon/carbon composites and their components in water vapour at high temperatures. Corrosion Science, 2015. 90: p. 340-346.

174. Zhang, J., et al., Degradation mechanism of SiCf/SiC composites after long-time water vapor and oxygen corrosion at 1300° C. Corrosion Science, 2022. 197: p. 110099.

175. Wolf, R.A., Carbon-Carbon Composites as Recuperator Material for Direct Gas Brayton Systems. 2006, Bettis Atomic Power Laboratory (BAPL), West Mifflin, PA.

176. Koyanagi, T., et al., Hermeticity of SiC/SiC composite and monolithic SiC tubes irradiated under radial high-heat flux. Journal of Nuclear Materials, 2024. 588: p. 154784.

177. Feng, S., et al., High temperature in-situ synchrotron-based XRD study on the crystal structure evolution of C/C composite impregnated by FLiNaK molten salt. Scientific Reports, 2017. 7(1): p. 10673.

178. Feng, S., et al., Improved mechanical properties and fracture mechanism of C/C composites with salt treatment monitored by synchrotron-based in-situ tensile XRD. Composites Part B: Engineering, 2020. 199: p. 108274.

179. Williams, D.F., Assessment of candidate molten salt coolants for the advanced high temperature reactor (AHTR). 2006.

180. Seregin, M., et al., Solubility of UF4, ThF4, and CeF3 in a LiF-NaF-KF melt. Radiochemistry, 2011. 53(5): p. 491-493.

181. Wilson, D.F., Chemical compatibility issues associated with use of SiC/SiC in advanced reactor concepts. 2015, Oak Ridge National Lab.(ORNL), Oak Ridge, TN (United States).

182. Katoh, Y., D.F. Wilson, and C.W. Forsberg, Assessment of silicon carbide composites for advanced salt-cooled reactors. 2007, Oak Ridge National Lab.(ORNL), Oak Ridge, TN (United States).

183. Xi, Jianqi, et al. "Corrosion of Si, C, and SiC in molten salt." Corrosion Science 146 (2019): 1-9.

184. Yang, X., et al., Corrosion of SiC induced by Hastelloy N alloy and its corrosion products in LiF–NaF–KF molten salt. Corrosion Science, 2016. 109: p. 62-67.

185. Xue, W., et al., Effects of Cr3+ on the corrosion of SiC in LiF–NaF–KF molten salt. Corrosion Science, 2017. 114: p. 96-101.

186. Wang, H., et al., The corrosion behavior of CVI SiC matrix in SiCf/SiC composites under molten fluoride salt environment. Journal of Nuclear Materials, 2017. 487: p. 43-49.

187. Yang, X., et al., Effect of oxygen on the corrosion of SiC in LiF–NaF–KF molten salt. Corrosion Science, 2016. 103: p. 165-172.

188. Wang, H., et al., Microstructure evolution and high-temperature mechanical properties of SiCf/SiC composites in liquid fluoride salt environment. Corrosion Science, 2017. 124: p. 131-137.

189. Lamm, B.W., et al., Corrosion characteristics of silicon carbide fiber-reinforced composites in beryllium-bearing molten fluoride salt. Corrosion Science, 2025. 244: p. 112635.

190. Nishimura, H., et al., Compatibility of structural candidate materials with LiF–BeF2 molten salt mixture. Journal of Nuclear Materials, 2000. 283: p. 1326-1331.

191. Xi, J., et al., Corrosion of Si, C, and SiC in molten salt. Corrosion Science, 2019. 146: p. 1-9.

192. Koyanagi, T., et al., Corrosion characteristics of monolithic SiC materials in beryllium-bearing molten fluoride salt. Corrosion Science, 2023. 220: p. 111301.

193. Lee, J.J., et al., Chemical compatibility of silicon carbide in molten fluoride salts for the fluoride salt-cooled high temperature reactor. Journal of Nuclear Materials, 2019. 524: p. 119-134.

194. Forsberg, C.W., et al., Tritium control and capture in salt-cooled fission and fusion reactors. Fusion Science and Technology, 2017. 71(4): p. 584-589.

195. Stempien, J.D., R.G. Ballinger, and C.W. Forsberg, An integrated model of tritium transport and corrosion in Fluoride Salt-Cooled High-Temperature Reactors (FHRs)–Part I: Theory and benchmarking. Nuclear Engineering and Design, 2016. 310: p. 258-272.

196. Calderoni, P., et al., Control of molten salt corrosion of fusion structural materials by metallic beryllium. Journal of Nuclear Materials, 2009. 386: p. 1102-1106.

197. Petti, D.A., et al., JUPITER-II molten salt Flibe research: An update on tritium, mobilization and redox chemistry experiments. Fusion Engineering and Design, 2006. 81(8-14): p. 1439-1449.

198. Causey, R.A. and W.R. Wampler, The use of silicon carbide as a tritium permeation barrier. Journal of Nuclear materials, 1995. 220: p. 823-826.

199. Causey, R., et al., Tritium migration in vapor-deposited β-silicon carbide. Journal of Nuclear Materials, 1993. 203(3): p. 196-205.

200. Nobuta, Y., et al., Tritium retention properties of tungsten, graphite and co-deposited carbon film. Fusion Engineering and Design, 2014. 89(7-8): p. 1516-1519.

201. Doyle, B., W. Wampler, and D. Brice, Temperature dependence of H saturation and isotope exchange. Journal of Nuclear Materials, 1981. 103: p. 513-517.

202. Sun, J. G., et al. "NDT technologies for ceramic matrix composites: Oxide and nonoxide." Materials Evaluation 64.1 (2006): 52-60.

203. Sun, J. G., et al. Thermal imaging measurement and correlation of thermal diffusivity in continuous fiber ceramic composites. No. ANL/ET/CP-93341; CONF-9710119-. Argonne National Lab.(ANL), Argonne, IL (United States), 1997.

204. Stuckey, J., J. G. Sun, and W. A. Ellingson. "Rapid infrared characterization of thermal diffusivity in continuous fiber ceramic composite components." Nondestructive Characterization of Materials VIII. Boston, MA: Springer US, 1998. 805-810.

205. Wang, Yu-Lin, et al. "Evaluation of Thermal Shock Damage in 2-D Woven Nicalon™-$Al_2O_3$ Composite by NDE Techniques." 22nd Annual Conference on Composites, Advanced Ceramics, Materials, and Structures: A: Ceramic Engineering and Science Proceedings. Vol. 19. Hoboken, NJ, USA: John Wiley & Sons, Inc., 1988.

206. Sun, Jiangang. Method for determining defect depth using thermal imaging. No. 6,542,849. Univ. of Chicago, IL (United States), 2003.

207. Kim, Jeongguk, and Peter K. Liaw. "The nondestructive evaluation of advanced ceramics and ceramic-matrix composites." JOM 50.11 (1998): 1-15.

208. Kim, Jeongguk, Peter K. Liaw, and Hsin Wang. "The nde analysis of tension behavior in nicalon/sic ceramic matrix composites." JOM 55.1 (2003): 1-13.

209. Ellingson, W. A., et al. "Characterization of Melt Infiltrated SiC/SiC Composite Combustor Liners Using Meso-and Micro-NDE Techniques." Turbo Expo: Power for Land, Sea, and Air. Vol. 78576. American Society of Mechanical Engineers, 2000.

210. Sun, J. G., et al. "Nondestructive evaluation of defects and operating damage in CFCC combustor liners." 26th Annual Conference on Composites, Advanced Ceramics, Materials, and Structures: A: Ceramic Engineering and Science Proceedings. Hoboken, NJ, USA: John Wiley & Sons, Inc., 2002.

211. Shiwa, Mitsuharu, et al. "Fracture mechanisms in unnotched and notched SiC/SiC composites studied by acoustic emission analysis." Materials Transactions, JIM 36.4 (1995): 511-517.

212. Luo, Jyi-Jiin, Shi-Chang Wooh, and Isaac M. Daniel. "Acoustic emission study of failure mechanisms in ceramic matrix composite under longitudinal tensile loading." Journal of Composite Materials 29.15 (1995): 1946-1961.

213. Jadaan, Osama M., K. C. Liu, and H. Pih. "Fatigue Evaluation in Ceramic Materials by Acoustic Emission." International Design Engineering Technical Conferences and Computers and Information in Engineering Conference. Vol. 11726. American Society of Mechanical Engineers, 1993.

*Page intentionally left blank*

**Applied Materials Division**
Argonne National Laboratory
9700 South Cass Avenue, Bldg. 212
Argonne, IL 60439

www.anl.gov

Argonne National Laboratory is a U.S. Department of Energy laboratory managed by UChicago Argonne, LLC